Rongfu Tang

Mathematical Methods
for Camera Self-Calibration
in Photogrammetry and Computer Vision

München 2013

Mathematical Methods
for Camera Self-Calibration
in Photogrammetry and Computer Vision

Von der Fakultät Luft- und Raumfahrttechnik und Geodäsie

der Universität Stuttgart

zur Erlangung der Würde eines

Doktors der Ingenieurwissenschaften (Dr.-Ing.)

genehmigte Abhandlung

Vorgelegt von

M.Sc. Rongfu Tang

München 2013

Adresse der Deutschen Geodätischen Kommission:

Deutsche Geodätische Kommission

Alfons-Goppel-Straße 11 ● D – 80 539 München

Telefon +49 – 89 – 23 031 1113 ● Telefax +49 – 89 – 23 031 - 1283 / - 1100
e-mail hornik@dgfi.badw.de ● http://www.dgk.badw.de

Hauptberichter: Prof. Dr.-Ing. habil. Dieter Fritsch
Mitberichter: Prof. Dr.-Ing. habil. Christian Heipke

Tag der mündlichen Prüfung: 28.05.2013

Diese Dissertation ist auch auf dem Dokumentenserver der Universität Stuttgart veröffentlicht
<http://elib.uni-stuttgart.de/opus/doku/e-diss.php>

Contents

Zusammenfassung

Die Kalibration von Kameras ist ein zentrales Thema in der Photogrammetrie und der Computer Vision. Das als Selbstkalibration bezeichnete Verfahren ist sehr flexibel und leistungsfähig und spielt eine signifikante Rolle bei der Bestimmung der inneren und äußeren Orientierung einer Kamera und in der bildbasierten Objektrekonstruktion. Diese Arbeit hat sich daher zum Ziel gesetzt, eine mathematische, detaillierte und synthetische Studie zum Einsatz der Selbstkalibration in der Luftbildphotogrammetrie, dem photogrammetrischen Nahbereich wie auch dem Computer Vision zu liefern.

In der Luftbildphotogrammetrie hat der Einsatz von zusätzlichen Parametern für Zwecke der Selbstkalibration eine lange Tradition, auch wenn diese oft pragmatisch und ohne große mathematische oder physikalische Begründungen genutzt werden. Zudem sind sie hochkorreliert mit anderen Korrekturparametern. Im photogrammetrischen Nahbereich sind hohe Korrelationen schon seit langem bekannt, nicht zuletzt durch das als Quasi-Standard eingesetzte Brown'sche Selbstkalibrationsmodell. Die negativen Effekte dieser hohen Korrelationen sind bisher nur unzulänglichuntersucht. Die Verzeichnungskorrektur ist eine wesentliche Komponente der photogrammetrischen Selbstkalibration; dies ist im Computer Vision-Bereich nicht unbedingt der Fall: Hier ist mit der Autokalibration die Festlegung von einigen wenigen Parametern beschrieben, unabhängig von Verzeichnung und Näherungswerten. Auch wenn in den letzten Jahrzehnten eine Auto-Kalibration für N≥3 Bilder sehr extensiv untersucht worden ist, stellt diese nach wie vor ein schwieriges Thema dar.

In dieser Arbeit wird zunächst das mathematische Problem der Selbstkalibration allgemein untersucht. Es kann gezeigt werden, dass die photogrammetrische Selbstkalibration (oder der Aufbau von Selbstkalibrationsmodellen) im Wesentlichen einer "Funktional-Approximation" der Mathematik entspricht. Die Abweichungen von der strengen Perspektivbildgeometrie werden mittels einer linearen Kombination von speziellen mathematischen Basisfunktionen approximiert. Mit Hilfe von algebraischen Polynomen kann eine Reihe von Legendre-Selbstkalibrationsmodellen definiert werden, die alle auf der Basis von orthogonalen, univariaten Legendre-Polynomen beruhen. Der Satz von Weierstrass garantiert, dass die geometrischen Abweichungen eines flächenhaft aufzeichnenden Kamerasystems effektiv durch die Verwendung von Legendre-Polynomen entsprechenden Grades kalibriert werden können. Dieses Legendre-Modell kann auch als eine wesentliche Verallgemeinerung der historischen Selbstkalibrationsmodelle, vorgeschlagen durch Ebner und Grün, angesehen werden, speziell wenn man Legendre-Polynome zweiten und vierten Grades einsetzt.

Aus mathematischer Sicht haben diese algebraischen Polynome jedoch einen unerwünschten Nebeneffekt - hohe Korrelationen zwischen den Polynomtermen. Dies ist auch der Grund für die hohen Korrelationen im Brown'schen Ansatz der Nahbereichsphotogrammetrie. Dieser Nachteil ist inhärent und unabhängig von Blockgeometrie und externer Orientierung der Bilder. Als Ergebnis von Korrelationsanalysen wurde daher für den photogrammetrischen Nahbereich ein verbessertes Modell zur Korrektur der Verzeichnung in der Bildebene vorgeschlagen.

Nachdem in dieser Arbeit eine Reihe von mathematischen Basisfunktionen geprüft wurden, werden speziell Fourierreihen als theoretisch optimale und geeignete Basisfunktionen zum Aufbau von Selbstkalibrationsmodellen empfohlen. Aus diesem Grund wurde eine Familie von Fourier-Selbstkalibrationsmodellen entwickelt, die auf der Laplace-Gleichung wie auch dem Satz von Fourier beruhen. Bei Abwägung aller Vor- und Nachteile von physikalischen und mathematischen Modellen zur Selbstkalibration wird vorgeschlagen, entweder Legendre- oder Fourierpolynome angereichert

durch Parameter für die Korrektur der radialen Verzeichnung für Kalibrationsanwendungen einzusetzen.

In dieser Arbeit wurden eine Reihe von Simulationen und empirischen Tests zur Untersuchung der neuen Selbstkalibrationsmodelle durchgeführt. Die Tests zu den digitalen Luftbildkamerasystemen zeigen, dass beide Gruppen – sowohl die Legendre- als auch die Fourier-Polynome –rigoros, flexibel, generisch, effektiv und erfolgreich zur Korrektur von geometrischen Abweichungen der Perspektivbildgeometrie von flächenhaft aufzeichnenden Kamerasystemen mit großen, mittleren oder kleinen Sensorformaten, eingesetzt in Einkopf- oder Mehrkopf-Systemen (eingeschlossen DMC, DMC II, UltraCamX, UltraCam Xp, DigiCAM usw.) eingesetzt werden können. Der Vorteil von Fourierpolynomen liegt darin, dass zum einen weniger zusätzliche Parameter notwendig sind und zum anderen eine bessere Verzeichnungskorrektur erreicht werden kann. Die Tests im photogrammetrischen Nahbereich zeigen, dass die Lage des Bildhauptpunkts zuverlässig rekonstruiert werden kann, obwohl hohe Korrelationen mit den dezentralen Verzeichnungsparametern auftreten. Das Modell der „Im-Bild"-Kalibration erlaubt eine verbesserte Bestimmung der Brennweite. Die gute Verwendungsmöglichkeit von kombinierten „Radial+Legendre"- sowie „Radial+Fourier"–Modellen zur Selbstkalibration wird gezeigt. Für den Einsatz im Computer Vision wird eine neue Methode zur Auto-Kalibration vorgeschlagen, welche lediglich Bildkorrespondenzen unabhängig von Bildverzerrung benötigt. Diese Methode basiert im Wesentlichen auf der Fundamentalmatrix und den drei (abhängigen) Bedingungen, abgeleitet von der Rang 2 Projektionsmatrix. Die drei wichtigsten Vorzüge des Verfahrens sind folgende: Erstens kann eine rekursive Strategie zur Bestimmung von Brennweite und der Lage des Bildhauptpunktes eingesetzt werden. Zweitens werden optimale geometrische Bedingungen ausgewählt mit Hinblick auf minimale Varianz. Drittens wird eine nichtlineare Optimierung für die vier internen Parameter mittels des Levenberg-Marquardt Algorithmus durchgeführt. Diese neue Methode der Autokalibration ist schnell, effizient und ergibt eine eindeutige Kalibration.

Neben diesem neuen Verfahren zur Autokalibration wird vorgeschlagen, die Brennweite aus nur zwei Bildern zu berechnen, unabhängig von der Lage des Bildhauptpunkts. Im Vergleich zur bisherigen Vorgehensweise, welche die exakte Lage des Bildhauptpunkts benötigt, ist die neue Methode viel flexibler und einfacher. Auch wenn die Autokalibration nicht in all ihren Details untersucht worden ist, konnten sehr gute Ergebnisse durch Simulationen und praktische Experimente nachgewiesen werden. Ferner werden Diskussionen für zukünftige Verbesserungen ausgeführt.

Es ist die Hoffnung des Autors, dass der Inhalt dieser Dissertation nicht nur alle relevanten mathematischen Prinzipien in die Praxis der Selbstkalibration eingeführt hat, sondern auch zum besseren Verständnis zwischen der Photogrammetrie und dem Computer Vision-Bereich beiträgt, die viele gemeinsame Aufgaben zu lösen haben, wenn auch mit unterschiedlichen mathematischen Hilfsmitteln.

Kennwörter: Photogrammetrie, geometrisches Computer Vision, Kamera-Selbstkalibration, zusätzliche Parameter, Brown'sches Modell der Selbstkalibration, Legendre-Modell der Selbstkalibration, Fourier-Modell der Selbstkalibration, Funktional-Approximation, Korrelation, Mehrfach-Bildgeometrie, Zweibild-Kalibration, Fundamentalmatrix.

Abstract

Camera calibration is a central subject in photogrammetry and geometric computer vision. Self-calibration is a most flexible and highly useful technique, and it plays a significant role in camera automatic interior/exterior orientation and image-based reconstruction. This thesis study is to provide a mathematical, intensive and synthetic study on the camera self-calibration techniques in aerial photogrammetry, close range photogrammetry and computer vision.

In aerial photogrammetry, many self-calibration additional parameters (APs) are used increasingly without evident mathematical or physical foundations, and moreover they may be highly correlated with other correction parameters. In close range photogrammetry, high correlations exist between different terms in the 'standard' Brown self-calibration model. The negative effects of those high correlations on self-calibration are not fully clear. While distortion compensation is essential in the photogrammetric self-calibration, geometric computer vision concerns auto-calibration (known as self-calibration as well) in calibrating the internal parameters, regardless of distortion and initial values of internal parameters. Although camera auto-calibration from $N \geq 3$ views has been studied extensively in the last decades, it remains quite a difficult problem so far.

The mathematical principle of self-calibration models in photogrammetry is studied synthetically. It is pointed out that photogrammetric self-calibration (or building photogrammetric self-calibration models) can – to a large extent – be considered as a *function approximation* problem in mathematics. The unknown function of distortion can be approximated by a linear combination of specific mathematical basis functions. With algebraic polynomials being adopted, a whole family of *Legendre self-calibration model* is developed on the base of the orthogonal univariate Legendre polynomials. It is guaranteed by the Weierstrass theorem, that the distortion of any frame-format camera can be effectively calibrated by the Legendre model of proper degree. The Legendre model can be considered as a superior generalization of the historical polynomial models proposed by Ebner and Grün, to which the Legendre models of second and fourth orders should be preferred, respectively.

However, from a mathemtical viewpoint, the algebraic polynomials are undesirable for self-calibration purpose due to high correlations between polynomial terms. These high correlations are exactly those occurring in the Brown model in close range photogrammetry. They are factually inherent in all self-calibration models using polynomial representation, independent of block geometry. According to the correlation analyses, a refined model of the in-plane distortion is proposed for close range camera calibration.

After examining a number of mathematical basis functions, the Fourier series are suggested to be the theoretically optimal basis functions to build the self-calibration model in photogrammetry. Another family of *Fourier self-calibration model* is developed, whose mathematical foundations are the Laplace's equation and the Fourier theorem. By considering the advantages and disvantages of the physical and the mathematical self-calibration models, it is recommended that the Legendre or the Fourier model should be combined with the radial distortion parameters in many calibration applications.

A number of simulated and empirical tests are performed to evaluate the new self-calibration models. The airborne camera tests demonstrate that, both the Legendre and the Fourier self-calibration models are rigorous, flexible, generic and effective to calibrate the distortion of digital frame airborne cameras of large-, medium- and small-formats, mounted in single- and multi-head systems (including the DMC, DMC II, UltraCamX, UltraCamXp, DigiCAM cameras and so on). The advantages of the Fourier model result from the fact that it usually needs fewer APs and obtains more reliable distortion calibration. The tests in close range photogrammetry show that, although it is highly correlated with

the decentering distortion parameters, the principal point can be reliably and precisely located in a self-calibration process under appropriate image configurations. The refined in-plane distortion model is advantageous in reducing correlations with the focal length and improving the calibration of it. The good performance of the combined "Radial + Legendre" and "Radial + Fourier" models is illustrated.

In geometric computer vision, a new auto-calibration solution which needs image correspondences and zero (or known) skew parameter only is presented. This method is essentially based on the fundamental matrix and the three (dependent) constraints derived from the rank-2 essential matrix. The main virtues of this method are threefold. First, a recursive strategy is employed subsequently to a coordinate transformation. With an appropriate approximation, the recursion estimates the focal length and aspect ratio in advance and then calculates the principal point location. Second, the optimal geometric constraints are selected using error propagation analyses. Third, the final nonlinear optimization is performed on the four internal parameters via the Levenberg–Marquardt algorithm. This auto-calibration method is fast and efficient to obtain a unique calibration.

Besides auto-calibration, a new idea is proposed to calibrate the focal length from two views without the knowledge of the principal point coordinates. Compared to the conventional two-view calibration techniques which have to know principal point shift a priori, this new analytical method is more flexible and more useful. Although the auto-calibration and the two-view calibration methods have not been fully mature yet, their good performance is demonstrated in both simulated and practical experiments. Discussions are made on future refinements.

It is hoped that this thesis not only introduces the relevant mathematical principles into the practice of camera self-calibration, but is also helpful for the inter-communications between photogrammetry and geometric computer vision, which have many tasks and goals in common but simply using different mathematical tools.

Keywords: photogrammetry, geometric computer vision, camera self-calibration, additional parameters (APs), Brown self-calibration model, Legendre self-calibration model, Fourier self-calibration model, function approximation, correlation, multi-view geometry, two-view calibration, fundamental matrix.

1 Introduction

"Being too hasty might obtain the right answer to the wrong problem."

—— Anonym.

Camera calibration is a central subject in photogrammetry and computer vision. It plays a crucial role in camera interior/exterior orientation and image-based reconstruction. Rigorously speaking, this thesis studies the *geometric calibration* rather than the radiometric calibration in photogrammetry, and the calibration in *geometric* computer vision. Without ambiguity, the terms "photogrammetry", "computer vision" and "calibration" in this thesis are referred to geometric photogrammetry, geometric computer vision and geometric calibration, respectively.

To understand camera calibration, the basic concepts of photogrammetry and computer vision need to be introduced in advance. The collinearity equations and projection equation, which are the mathematical fundamentals in photogrammetry and computer vision respectively, can be exactly derived from the mathematical central projection.

1.1 Basic concepts

1.1.1 Camera coordinate system

The definition of a camera coordinate system differs slightly in photogrammetry and computer vision. In Fig. 1.1, XYZ and xyz are the world coordinates and the camera coordinates, respectively. The perspective center and the principal point are denoted by O and PP, respectively. Both camera coordinates are right hand coordinate systems, and their difference is raised by the different z directions.

1.1.2 Central projection

A mathematical form of the central projection in the three dimensions is given by

$$\begin{pmatrix} X \\ Y \\ Z \end{pmatrix} = \begin{pmatrix} X_0 \\ Y_0 \\ Z_0 \end{pmatrix} + m_X \mathrm{R}(\omega, \varphi, \kappa) \begin{pmatrix} x - x_0 \\ y - y_0 \\ \pm f \end{pmatrix} \tag{1.1}$$

where

- X, Y and Z are the coordinates of an object point in the world coordinates;
- X_0, Y_0 and Z_0 are the coordinates of the camera perspective center in the world coordinates;
- $\mathrm{R}(\omega, \varphi, \kappa) \triangleq \left(r_{ij} \right)_{i,j=1,2,3}$ is the rotation matrix from the camera coordinates to the world coordinates, and ω, φ and κ are the three rotation angles;
- $X_0, Y_0, Z_0, \omega, \varphi$ and κ are the six parameters of the exterior orientation (or external/extrinsic orientation, EO);
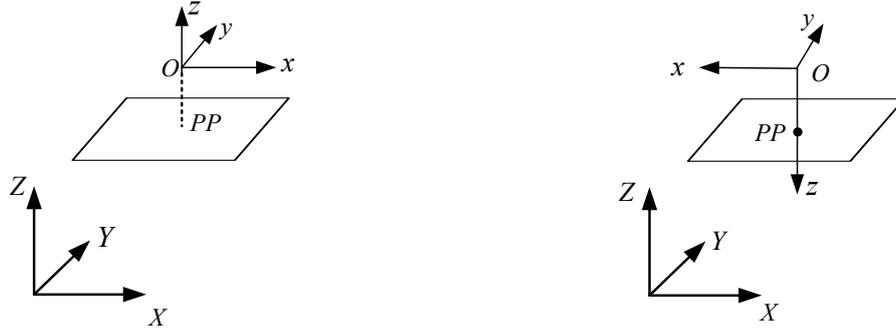
Fig. 1.1 Camera coordinate systems defined in photogrammetry (left) and in computer vision (right).

- x and y are the coordinates of an image point in the camera coordinates;
- x_0 and y_0 are the coordinates of the principal point, and f is focal length (principle distance)[1]. They are often called the three interior orientation (IO) parameters in photogrammetry;
- The sign of f depends on the definition of the camera coordinates (see Fig. 1.1). It is $-f$ in photogrammetry and f in computer vision;
- m_X is the scale factor given in (1.2) below; and
- The camera model in (1.1) has 9 degrees of freedom (DOF), i.e., the three IO parameters and the six EO parameters.

$$m_X = \frac{1}{\pm f}\left(r_{13}(X - X_0) + r_{23}(Y - Y_0) + r_{33}(Z - Z_0)\right) \tag{1.2}$$

1.1.3 Collinearity equations

In Cartesian coordinates of Euclidean geometry, the photogrammetric collinearity equations can be derived as (1.3) by eliminating the scale factor m_X in (1.1):

$$\begin{aligned}
x &= x_0 - f\frac{r_{11}(X - X_0) + r_{21}(Y - Y_0) + r_{31}(Z - Z_0)}{r_{13}(X - X_0) + r_{23}(Y - Y_0) + r_{33}(Z - Z_0)}\\
y &= y_0 - f\frac{r_{12}(X - X_0) + r_{22}(Y - Y_0) + r_{32}(Z - Z_0)}{r_{13}(X - X_0) + r_{23}(Y - Y_0) + r_{33}(Z - Z_0)}
\end{aligned} \tag{1.3}$$

where the photogrammetric camera model has thus 9 DOF, same as that in the central projection (1.1).

In most practices, there exists distortion which causes departures from the ideal equations (1.3). The collinearity equations with distortion and random errors are described as

$$\begin{aligned}
x &= x_0 - f\frac{r_{11}(X - X_0) + r_{21}(Y - Y_0) + r_{31}(Z - Z_0)}{r_{13}(X - X_0) + r_{23}(Y - Y_0) + r_{33}(Z - Z_0)} + \Delta x + \varepsilon\\
y &= y_0 - f\frac{r_{12}(X - X_0) + r_{22}(Y - Y_0) + r_{32}(Z - Z_0)}{r_{13}(X - X_0) + r_{23}(Y - Y_0) + r_{33}(Z - Z_0)} + \Delta y + \varepsilon
\end{aligned} \tag{1.4}$$

---

[1] Rigorously speaking, the principal distance is defined slightly differently from the focal length. The principal distance is the length of the normal from the perspective centre of the lens to the image plane (Newby, 2012). Focal length is referred as "equivalent focal length" which is an approximate value of principal distance which is also called "calibrated focal length" (McGlone et al., 2004). In this thesis, this slight difference is ignored and "focal length" stands mostly for the principal distance.

where Δx and Δy are the distortion terms, and ε indicates the random error. Δx and Δy are often represented by parametric models which are known as *self-calibration models*.

Because of the fundamental role of the *nonlinear* collinearity equations in photogrammetry, lots of the photogrammetric analytical techniques are nonlinear, iterative and requiring good initial values.

1.1.4 Projection equation

Denote

$$\begin{pmatrix} X' \\ Y' \\ Z' \end{pmatrix} \triangleq \mathrm{R}^T \begin{pmatrix} X - X_0 \\ Y - Y_0 \\ Z - Z_0 \end{pmatrix} = \mathrm{R}^T \begin{pmatrix} 1 & 0 & 0 & -X_0 \\ 0 & 1 & 0 & -Y_0 \\ 0 & 0 & 1 & -Z_0 \end{pmatrix} \begin{pmatrix} X \\ Y \\ Z \\ 1 \end{pmatrix}. \tag{1.5}$$

Then $m_X = Z'/f$ and (1.1) can be rewritten as

$$\begin{pmatrix} x - x_0 \\ y - y_0 \\ f \end{pmatrix} = f/Z' \begin{pmatrix} X' \\ Y' \\ Z' \end{pmatrix} \tag{1.6}$$

and

$$\begin{pmatrix} x \\ y \\ f \end{pmatrix} = \begin{pmatrix} x_0 \\ y_0 \\ 0 \end{pmatrix} + \frac{1}{Z'} \begin{pmatrix} f & 0 & 0 \\ 0 & f & 0 \\ 0 & 0 & f \end{pmatrix} \begin{pmatrix} X' \\ Y' \\ Z' \end{pmatrix} = \frac{1}{Z'} \begin{pmatrix} f & 0 & x_0 \\ 0 & f & y_0 \\ 0 & 0 & f \end{pmatrix} \begin{pmatrix} X' \\ Y' \\ Z' \end{pmatrix}. \tag{1.7}$$

By noticing $f \equiv fZ'/Z'$, (1.7) is equivalent to

$$Z' \begin{pmatrix} x \\ y \\ 1 \end{pmatrix} = \begin{pmatrix} f & 0 & x_0 \\ 0 & f & y_0 \\ 0 & 0 & 1 \end{pmatrix} \begin{pmatrix} X' \\ Y' \\ Z' \end{pmatrix}. \tag{1.8}$$

Using the *homogeneous* representation in the two dimensional image coordinates $((x, y, 1)^T$ and $(ax, ay, a)^T$ represent the same point in two dimensions for any $a \neq 0$), Z' can removed from (1.8):

$$\begin{pmatrix} x \\ y \\ 1 \end{pmatrix} = \begin{pmatrix} f & 0 & x_0 \\ 0 & f & y_0 \\ 0 & 0 & 1 \end{pmatrix} \begin{pmatrix} X' \\ Y' \\ Z' \end{pmatrix}. \tag{1.9}$$

A geometric interpretation of the equivalence between (1.8) and (1.9) is that the coordinates of imaging points are independent of the scene depth Z'. Inserting (1.5) into (1.9) obtains

$$\begin{pmatrix} x \\ y \\ 1 \end{pmatrix} = \begin{pmatrix} f & 0 & x_0 \\ 0 & f & y_0 \\ 0 & 0 & 1 \end{pmatrix} \mathrm{R}^T \begin{pmatrix} 1 & 0 & 0 & -X_0 \\ 0 & 1 & 0 & -Y_0 \\ 0 & 0 & 1 & -Z_0 \end{pmatrix} \begin{pmatrix} X \\ Y \\ Z \\ 1 \end{pmatrix} \tag{1.10}$$

$$\begin{pmatrix} x \\ y \\ 1 \end{pmatrix} = \mathrm{P} \begin{pmatrix} X \\ Y \\ Z \\ 1 \end{pmatrix} \tag{1.11}$$

where

$$K = \begin{pmatrix} f & 0 & x_0 \\ 0 & f & y_0 \\ 0 & 0 & 1 \end{pmatrix}, C = \begin{pmatrix} X_0 \\ Y_0 \\ Z_0 \end{pmatrix}, P = KR^T[I| - C]. \tag{1.12}$$

P is defined as the *camera matrix* and K is the *calibration matrix*. (1.11) is the *projection equation* and also named as the *basic pinhole camera model*. It should be noted that the pinhole model (1.11) should contain 9 DOF while a general 3×4 matrix P has 11 DOF.

In CCD cameras, two parameters are additionally introduced into the calibration matrix:

$$K = \begin{pmatrix} f & s & x_0 \\ 0 & \alpha f & y_0 \\ 0 & 0 & 1 \end{pmatrix} \tag{1.13}$$

where α is the aspect ratio and s is the skew parameter. $\alpha = u_x/u_y$ where u_x and u_y are the pixel size in x and y directions, respectively; and $\alpha = 1$ for the square pixel. s accounts for the angle between the pixel axes and $s = 0$ holds in most practices. It will be shown that s is exactly the parameter B_2 of the in-plane distortion in photogrammetry (up to a constant scale factor). These two parameters enable filling the gap of DOF between a general 3×4 camera matrix and the pinhole camera model[2].

The projection equation (1.11) is the fundamental formula in computer vision, as well as the collinearity equations in photogrammetry. Due to its linear form, many analytical methods in computer vision are linear.

It is evident from the above mathematical derivations that the collinearity equations in photogrammetry are the *Cartesian* representation of the central projection in *Euclidean geometry*, while the projection equation in computer vision is the *homogeneous* representation of the central projection in *projective geometry*. The mathematical fundamentals of photogrammetry and computer vision are essentially the same.

1.1.5 Terminology

Due to the different traditions, philosophies and mathematics being used, there are differences of the terminology in photogrammetry and computer vision.

Interior orientation V.S. **internal orientation (IO)**: interior orientation is uniquely adopted in photogrammetry while internal/intrinsic orientation is routinely used in computer vision. The interior orientation parameters include x_0, y_0, f, and the parameters of Δx and Δy in (1.4), while the five internal orientation parameters (known as the calibration parameters as well) are x_0, y_0, f, α and s in the calibration matrix (1.13).

Exterior orientation V.S. **external/extrinsic orientation (EO)**: exterior orientation is used in photogrammetry and external/extrinsic orientation is usually employed in computer vision. Both refer to the same six parameters: $X_0, Y_0, Z_0, \omega, \varphi$ and κ.

Camera calibration: Notwithstanding the different definitions, the purposes of camera calibration in photogrammetry and computer vision are, quite similarly, to determine the parameters of interior

---

[2] It sometimes confuses the photogrammetrists that why the skew parameter s (equivalently B_2) is introduced into the calibration matrix in computer vision, but not others such as the parameters of the radial and the decentering distortion which are definitely much more significant in practice? In the textbooks by Hartley & Zisserman (2003), there is an example, though not much photogrammetric, illustrating the case $s \neq 0$. The introduction of s may, to a large extent, be used to fill the gap of DOF between the camera model and a general 3×4 matrix.

orientation and internal orientation, respectively (those parameters are differently defined). Compensating Δx and Δy (if necessary) in computer vision is often known as **distortion correction**.

Distortion: The terms, such as "systematic image errors", "lens distortion" and "image distortion", are often used to indicate Δx and Δy in photogrammetry. The lens distortion may be only part of the distortion sources in the multi-head camera systems (see Section 1.3.2 below), and "systematic image errors" is rarely known in computer vision. The term "image distortion" is thus adopted in this thesis, disregarding the potential trivial differences among these terms. It is also noteworthy that the "projective distortion", "affine distortion" and "similarity distortion" are used frequently in computer vision. They stand for the deformation of the Euclidean reality caused by the projective, affine and similar transformations, respectively; they are not mattered with Δx and Δy.

For more on the basic concepts in photogrammetry and computer vision, the readers are referred to the textbooks, such as Kraus (2007), Luhmann et al. (2006) and Mikhail et al. (2001) in photogrammetry, and Faugeras (1993) and Hartley & Zisserman (2003) in computer vision.

1.2 Camera calibration

1.2.1 Camera calibration in photogrammetry

Camera calibration has been investigated in the photogrammetric society for several decades. A general definition of *calibration* by the International Vocabulary of Basic and General Terms in Metrology (VIM, 2007) is

> "*set of operations that establish, under specified conditions, the relationship between values of quantities indicated by a measuring instrument or measuring system, or values represented by a material measure or a reference material, and the corresponding values realized by standards*".

Another definition, closer to camera calibration, was given in Slama (1980): calibration is

> "*the act and process of determining certain specific measurements in a camera or other instrument or device by comparison with a standard, for use in correcting or compensating errors for purposes of record*".

The definitions of camera calibration have changed significantly over recent years. While there is no well-accepted definition, the purpose of camera calibration in photogrammetry is to determine the geometric camera model described by the parameters of interior orientation, including focal length, principal point shift, the distortion terms and others (McGlone et al., 2004; Luhmann et al., 2006).

There are different definitions of principal point during the development of photogrammetric calibration. They are the indicated principal point (fiducial center), the principle point of best symmetry and the principal point of autocollimation, denoted by IPP, PPS and PPA, respectively. Some important notes on these principal points are (Kraus, 2007):

- they lie within a circle of radius < 0.02 mm in most metric cameras;
- IPP is valid only in analogue cameras but not in digital cameras anymore;
- both PPS and PPA are recorded in the digital camera calibration report; and
- PPA is the mathematical definition of principal point in (1.1).

Different calibration techniques have been employed in photogrammetry as follows (Kraus, 1997; Clarke & Fryer, 1998; McGlone et al., 2004; Luhmann et al., 2006).

Laboratory calibration. Laboratory calibration is generally used only for metric cameras. The IO parameters are determined by goniometers, collimators or other optical alignment instruments.

Test field calibration. Test field calibration uses a suitable targeted field of object points with known coordinates or distances. This test field is imaged from multi-view camera stations, ensuring good ray intersection and filling the image format. This calibration is processed by bundle adjustment to calculate the IO parameters.

Plumb-line calibration. Plumb-line method employs a test field with several straight lines. Its main principle is that a straight line must be imaged as a straight line and all deviations should be caused by distortion.

In-situ calibration. In-situ calibration (known as on-the-job calibration as well) indicates a test field calibration with combination of actual object measurements of known coordinates. It is processed by the self-calibrating bundle adjustment technique.

Self-calibration. Self-calibration can be considered as an extension to test field and in-situ calibration. It does not require any known reference points.

Each calibration technique has advantages as well as disadvantages.

- As it is hardly performed by camera users, laboratory calibration is often employed for airborne cameras but not practical in close range photogrammetry. It is recognized that the distortion can be impacted by the environment and this may be not fully accounted in the lab calibration.
- As the analytical calibration methods, including test field, plumb-line, in-situ and self-calibration techniques, are processed by the bundle adjustment, good initial values of the IO and EO parameters are required for good convergence and precise calibration.
- The test field, in-situ and self-calibration techniques can precisely determine the IO parameters in an appropriate configuration of multiple views. They are quite popular in close range photogrammetry, and self-calibration is the most flexible technique. The high correlations between different terms should be cautioned in practice.
- A major advantage of the plumb-line calibration is that it avoids high correlations. However, it cannot locate the principal point and usually needs a pre-defined principal point. The plumb-line method is rarely used in aerial photogrammetry.
- The parametric self-calibration models of Δx and Δy play a crucial role in analytical calibration methods. The unknown coefficients of the self-calibration model are called *self-calibration additional parameters (APs)*. Self-calibration by using APs has been widely accepted and substantially used as an efficient technique in photogrammetry.
- In-situ airborne camera calibration has recently received many attentions and becomes a routine process (in fact, some airborne camera vendors rely only on the in-situ calibration). Although self-calibration itself is unworkable in aerial photogrammetry (this is due to the distinctive block geometry of nadir looking; the ground control and aerial control are necessary), the self-calibration models are vital for the in-situ calibration.

1.2.2 Camera calibration in computer vision

Camera calibration in computer vision is to determine the calibration matrix. There are two major distinctions between the camera calibration in photogrammetry and that in computer vision. First, while the precise prior information on the interior orientation (focal length at least) is needed in most photogrammetric cases, the calibration in computer vision, benefiting from the linear projection equation (1.11), does not require any prior knowledge on the internal parameters (unless specified otherwise). Second, the distortion compensation is a critical issue in the photogrammetric calibration, but it is much less or even not considered in computer vision (perhaps due to the vision philosophy: why the distortion needs to be taken into account for making a computer see?).

Besides image correspondences, many calibration techniques in computer vision require one or more additional constraints, such as camera motion, scene information, three-dimensional (3D) or two-dimensional (2D) object coordinates, and partial knowledge on the internal parameters. There is a very

important calibration technique named as self-calibration (or auto-calibration) which is defined to determine a constant calibration matrix by using only image correspondences from multiple views. Any prior information on camera motion, scene constraints or calibration parameters is not required in self-calibration. This "self-calibration" in computer vision is definitely different from that in photogrammetry, except that both do not use any control points. To avoid ambiguity, the term "auto-calibration" is adopted to indicate the self-calibration in computer vision.

1.3 Related work on camera self-calibration

1.3.1 Self-calibration in close range photogrammetry

The concept of self-calibration appeared initially in close range photogrammetry, mainly due to the pioneer work of Duane C. Brown. He developed the camera distortion model (Brown, 1956, 1964, 1966) and firstly introduced an analytical calibration method (Brown, 1971). His self-calibration model includes the three IO parameters, the radial distortion (three parameters) and the decentering distortion (two parameters).

Brown's work was followed by many investigations (Kenefick et al., 1972; Faig, 1975; Wong, 1975; Ziemann & El-Hakim, 1982; Fryer & Brown, 1986; Fryer & Fraser, 1986; Fryer et al., 1994; Fraser et al., 1995). Although it was originated for analogue camera calibration, the Brown model has found great significance in the digital era as well. The Brown model of eight parameters was suggested by Fraser (1997) to be combined with two parameters of the in-plane distortion for digital camera self-calibration. The Brown model and the 10-parameter extension are very favorable in close range photogrammetry. Notwithstanding any changes of terminology, the formulae proposed by Brown appear to have remained virtually unchallenged for over forty years, as mentioned by Clarke & Fryer (1998) who gave an excellent review on the early calibration work.

Many works have been investigated on the practical applications of the Brown self-calibration model. They may be categorized as follows (to cite a few).

- Methodology studies: an important characteristic of the Brown model is the zoom effects, which were observed in many self-calibration studies (Wiley & Wong, 1995; Fraser & Al-Ajlouni, 2006). Wester-Ebbinghaus (1983) studied the impact of image configurations on self-calibration. The plumb-line calibration method was studied in Habib et al. (2002) and the effects of various straight line patterns were explored in José & Cabrelles (2007).
- Camera-based studies: the photogrammetric model and calibration of underwater camera were studied in Fryer & Fraser (1986) and Telem & Filin (2010). The stability of the off-shelf lenses was analyzed in Läb & Förstner (2004) and Habib & Morgan (2005). Stamatopoulos & Fraser (2011) studied calibrating the cameras of long focal length, where the correlations are rather high between the EO and the three IO parameters.
- Implementations: different calibration implementations and algorithms were compared in Remondino & Fraser (2006). Targetless camera calibration was recently studied in Barazzetti et al. (2011). And
- Applications: the applications in industry and heritage documentation are illustrated in such as Granshaw (1980), Yilmaza (2008) and Luhmann (2010).

A main inconvenience of the Brown self-calibration model is high correlations between different parameters. Those high correlations have been well recognized for almost as long as the self-calibration itself (Brown, 1971, 1972, 1989; Ziemann, 1986; Fraser, 1997; Clarke & Fryer, 1998; Clarke et al., 1998; Luhmann et al., 2006).
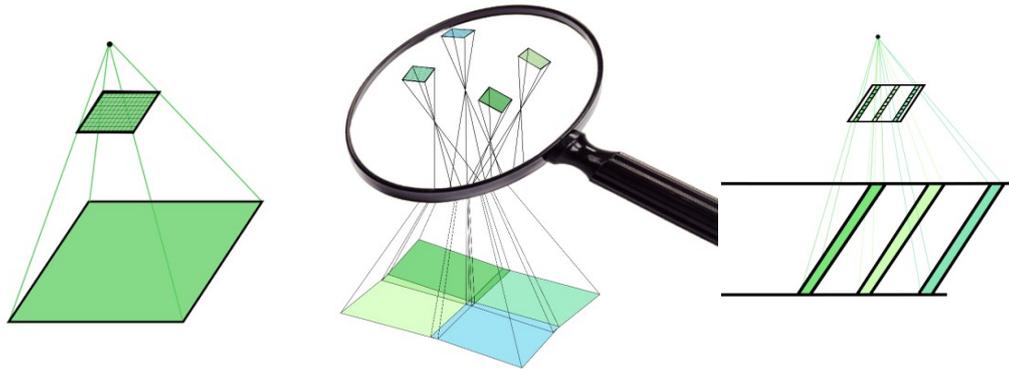
Fig. 1.2 Different formats of digital airborne cameras (from left to right): single-head, multi-head and three-line-scanner (push-broom) (Cramer et al., 2012) © 2012 Springer.

1.3.2 Self-calibration in aerial photogrammetry

Besides in close range photogrammetry, the self-calibration models play a significant role in compensating the distortion of airborne cameras in aerial photogrammetry as well.

Brown (1976) extended his classical close range self-calibration model to calibrate the single-head analogue airborne cameras. This model contains additional terms which were supposed to compensate the film deformation and unflatness. The polynomial models were introduced in Ebner (1976) and Grün (1978) by using the orthogonal polynomials of second and fourth orders, respectively. El-Hakim & Faig (1977) proposed a mathematical self-calibration model by using spherical harmonics. Jacobsen (1982) implemented a set of APs in his bundle adjustment software. A number of early effects were carried out to investigate the self-calibrating bundle adjustment with APs (Schut, 1979; Ackermann, 1981; Kilpelä, 1981; Kilpelä et al., 1981). These contributions showed that self-calibration APs could reduce remarkably image residuals and improve accuracy. The concerns were raised as well on overparameterization, high correlations and the theoretical foundations of self-calibration APs (Ackermann, 1981; Clarke & Fryer, 1998). Ackermann (1981) presented many theoretical and practical discussions which are still valuable for digital airborne camera calibration. A few traditional self-calibration models are illustrated in Appendix A.

There were two main developments in digital aerial photogrammetry. The first one is the introduction of digital airborne cameras, whose manufacturing technologies are quite different from those of analogue cameras (Sandau, 2010). In contrast to the analogue airborne camera of typical 23cm×23cm size (such as the Zeiss RMK camera and Leica RC camera), digital cameras have various formats:

- the push-broom cameras, such as the Airborne Digital Sensor (ADS40 and ADS80) in Leica Geosystems/Hexagon, the Jena Airborne Scanner (JAS) in Jena-Optronik GmbH, the HRV cameras in SPOT satellites and the cameras in WorldView-1 satellites;
- the large-format cameras, such as the Digital Mapping Camera (DMC) and DMC II in Intergraph Z/I Imaging/Hexagon, the cameras of UltraCam family in Vexcel/Microsoft, and the Quattro DigiCAM cameras in Ingenieur-Gesellschaft für Interfaces (IGI) mbH;
- the medium-format cameras, such as the cameras of DigiCAM series in IGI mbH and the cameras of RCD series in Leica Geosystems/Hexagon; and
- the small-format cameras, such as Digital Camera System (DCS) in Kodak.

It should be noted that with the development of hardware and technologies, the dividing lines among small, medium, and large format sensors has shifted and will continue to shift.

There are single-head cameras (such as DMC II, RCD 30 and DCS cameras) and multi-head cameras (such as DMC, UltraCam family and Quattro DigiCAM). The multi-head cameras usually employ virtual image composition techniques to create very large format aerial images. The distortion sources

of multi-head cameras are thus much more complex than those of single-head types. Different format sensors are illustrated in Fig. 1.2.

The second striking development is the successful incorporation of navigation sensors into airborne camera systems (Schwarz, 1993; Ackermann, 1994; Skaloud et al., 1996; Skaloud & Legat, 2008; Blázquez & Colomina, 2012). The navigation sensors are typically GPS (Global Positioning System, or Global Navigation Satellite System (GNSS)) or GPS/IMU integration (Inertial Measurement Unit or Inertial Navigation System (INS)). This leads to so-called direct georeferencing and integrated sensor orientation (Heipke et al., 2002), which reduce the number of ground control points (GCPs), increase reliability and flexibility, and accelerate photogrammetric mapping. The introduction of GPS/IMU (or GPS/INS) system as aerial control makes the in-situ airborne camera calibration feasible. Besides distortion calibration, the systematic errors in the direct observations of EO parameters need to be compensated.

Since of these revolutions, many effects were devoted to the calibration of digital airborne camera systems (Fritsch, 1997; Kersten & Haering, 1997; Schuster & Braunecker, 2000; Zeitler et al., 2002; Kröpfl et al., 2004; Chen et al., 2007; Jacobsen, 2011). Cramer (2009, 2010) reported the comprehensive empirical tests carried out by EuroSDR (European Spatial Data Research) and DGPF (German Society for Photogrammetry, Remote Sensing and Geoinformation). It is now well accepted that the in-situ calibration has become a new option and an indispensable calibration procedure (Heipke et al., 2002; Honkavaara et al., 2006; Kresse, 2006; Cramer et al., 2010). For overall system calibration, the misalignments between camera and navigation instruments and the drift/shift effect must be compensated (Honkavaara, 2004; Yastikli & Jacobsen, 2005).

Unlike the dominant role of the Brown model or the 10-parameter extension in close range photogrammetry, there is no such 'standard' self-calibration model for digital airborne camera calibration. A number of different self-calibration models were employed to compensate the distortion of airborne cameras (Cramer, 2009; Jacobsen et al., 2010).

1.3.3 Auto-calibration in computer vision

Camera auto-calibration was originally introduced by Faugeras et al. (1992) in computer vision. The methods based on the Kruppa equation were later developed by Maybank & Faugeras (1992), Heyden & Astrom (1996) and Luong & Faugeras (1997). Stratification approach was proposed by Pollefeys & van Gool (1997) and refined recently by Chandraker et al. (2010). Triggs (1997) introduced the absolute (dual) conic as a numerical device for formulating auto-calibration problem. These early works are however quite sensitive to noise and unreliable (Bougnoux, 1998; Hartley & Zisserman, 2003). An excellent comprehensive overview on the early auto-calibration work is given in the whole Chapter 19 of the textbooks by Hartley & Zisserman (2003). The numerical solution using interval analysis was presented in Fusiello et al. (2004), but this method is quite time consuming.

Other techniques, of which some were although proclaimed as auto-calibration, use different constraints, such as camera motion (Hartley, 1994; Stein, 1995; Horaud & Csurka, 1998; Agapito et al., 1999), scene constraints by using the vanishing points (Caprile & Torre, 1990; Liebowitz & Zisserman, 1998; Hartley et al., 1999), plane constraints (Triggs, 1998; Sturm & Maybank, 1999; Malis & Cipolla, 2002; Knight et al., 2003), concentric circles (Kim et al., 2005), plumb-lines (Geyer & Daniilidis, 2002) and others (Pollefeys et al., 1998; Liebowitz & Zisserman, 1999); and partial calibration information (Sturm et al., 2005). Nevertheless, not all of them are practically useful.

Instead of calibrating all the internal parameters from $N \geqslant 3$ views, it was recently studied to estimate focal length from two-views, given the other internal parameters, i.e., aspect ratio and principal point (Sturm et al., 2005; Stewénius et al., 2005; Li, 2008). However, the prerequisite of known principal point can hardly be satisfied in practice.

Although image distortion is less important, it is critical for the camera-based vision applications. The distortion, particularly the radial distortion, is occasionally accounted in vision (Tsai, 1987; Weng et al., 1992; Zhang, 2000). These techniques contain essentially two-steps: a close-form solution to

obtain the initial values of calibration parameters, and a subsequent nonlinear optimization. The known object coordinates (3D or 2D information, while the 2D planar board can be viewed as a special type of 3D test field with $Z = 0$) are necessary for the close-form solution. These methods can thus be categorized as the test-field calibration techniques from a photogrammetric viewpoint. Mallon & Whelan (2004) described how to approximate the inverse of the Brown radial distortion model, in order to get an 'undistorted' image which is not of much sense in photogrammetry[3]. Fitzgibbon (2001) proposed the so-called division model of radial distortion, whose applications were found in such as calculating the fundamental matrix for cameras with radial distortion (Barreto & Daniilidis, 2005). The non-parametric radial distortion correction was recently studied in Hartley & Kang (2007).

1.4 Problem settings

Due to the vital importance of camera calibration in photogrammetry and computer vision, numerous effects have been contributed into this subject (even the citations in this thesis are a small set of the whole contribution yet). Self-calibration is the most flexible and highly useful calibration technique. The self-calibration model is crucial for high-accuracy photogrammetric applications. It is recognized that, although many outstanding successes have been achieved, a number of important problems on self-calibration remain unsolved. The following three relevant subjects on self-calibration are undertaken and addressed in this thesis.

1.   Self-calibration models in aerial photogrammetry.

There are inconveniences on the existing self-calibration models for airborne camera calibration.

- Due to the development of digital airborne cameras, the traditional self-calibration APs, which were originated for the single-head analogue camera calibration, may not fit the distinctive features of digital airborne cameras, such as multi-head, virtual images composition and various image formats.
- Although self-calibration APs are increasingly employed for calibration purposes, many of them appear to have no evident mathematical or physical foundations. The foundations are essential to address the following questions: whether the self-calibration model is appropriate to calibrate the distortion of the camera being used? Whether the distortion has been (almost) fully calibrated by the used self-calibration model? Is there any overparameterization or underparameterization effect?
- From the viewpoint of overall system calibration, camera self-calibration must be decoupled from the correction of other systematic errors. Decoupling is vital in the senses that each systematic error must be independently (in statistical sense) calibrated and the calibration results should be block-independent. Decoupling indicates mathematically low correlations between different correction parameters. However, some self-calibration APs suffer high correlations with other parameters.
- Last but not least, some self-calibration APs are tailored for specific cameras concerning the manufacturing technologies. They can hardly be used to calibrate different cameras in a general sense.

Therefore, new self-calibration models are desired for digital airborne camera calibration. These new models should have solid mathematical or physical foundations and low correlations with other correction parameters. Further, the new models might be generally effective to calibrate the distortion of all frame-format airborne cameras.

---

[3] The distortion is originated in principal point. Correcting distortion is thus impractical unless principal point is known.

2. Self-calibration models in close range photogrammetry.

It is well known that high correlations, usually over 0.90, exist between the principal point shift and the parameters of the decentering distortion. High correlation also occurs between focal length and an in-plane distortion parameter. High correlations imply that the errors of one parameter can be corrected by the parameters of another. Harmful effects can be induced by high correlations, and high correlations may lead to a weakening calibration solution or unrealistic calibration results. Many effects were devoted to circumvent the high correlations in the close range camera self-calibration, but most of them seemed unnecessary (Clarke & Fryer, 1998).

The following critical questions remain not fully resolved: to what extent the principal point shift can be compensated by the parameters of the decentering distortion due to high correlations? Or inversely, to what extent the decentering distortion can be compensated by the principal point shift? Further, can self-calibration always obtain reliable and realistic calibration results?

In order to answer these questions, more theoretical works are desired to explore the reasons behind the correlations. Quantitative analyses should be investigated to learn the negative effects of these high correlations in practice. The 10-parameter model could even be refined.

3. Camera auto-calibration in computer vision.

Auto-calibration is essential if the camera information is unavailable or inadequate for camera orientation and scene reconstruction. Auto-calibration is not only of vital importance in computer vision, but also significant in photogrammetry. Camera information can be missed in some mobile mapping cases, such as reconstruction using historical images. Auto-calibration is a prerequisite to obtain precise initial values of the IO parameters for photogrammetric reconstruction in these cases.

Although it is possible to auto-calibrate a camera from $N \geqslant 3$ views and various methods have been proposed in the last two decades, it remains quite a difficult problem in computer vision (Hartley & Zisserman, 2003). The work on auto-calibration should be continued for its ultimate efficient solution.

The study of these three subjects is not only significant in each corresponding area, but also can offer a synthetic overview of the self-calibration models in aerial and close range photogrammetry, and help to bridge the gaps of calibration techniques in photogrammetry and computer vision.

1.5 Outline of the thesis

The general aim of this thesis is to *provide a mathematical, intensive and synthetic study on the camera self-calibration techniques in aerial photogrammetry, close range photogrammetry and computer vision*. The thesis is outlined as follows.

In Chapter 2, the mathematical principle of self-calibration models in photogrammetry is studied. It is pointed out that photogrammetric self-calibration (or building photogrammetric self-calibration models) can – to a large extent – be considered as a *function approximation* or, more precisely, curve fitting problem in mathematics. Image distortion can be approximated by a linear combination of specific mathematical basis functions. Different sets of basis functions are regarded. With the algebraic polynomials being adopted, a whole family of so-called *Legendre self-calibration model* is developed from the orthogonal univariate Legendre Polynomials. It is guranteed by the renowned Weierstrass theorem, that the Legendre APs of proper degree are capable to effectively calibrate the distortion of any frame-format camera. The Legendre self-calibration model can be considered as a superior generalization of the polynomial models proposed by Ebner (1976) and Grün (1978), to which the Legendre APs of second and fourth orders should be preferred, respectively. However, from a mathemtical viewpoint, the algebraic polynomials are undesirable for self-calibration purpose due to

the high correlations between different polynomial terms. After examining many mathematical basis functions, the Fourier series are suggested to be the theoretically optimal ones to build a self-calibration model. Another family of *Fourier self-calibration model* is developed, whose mathematical foundations are the Laplace's equation and the Fourier theorem. The combination of the Fourier (or Legendre) model and the parameters of radial distortion is recommended in many calibration applications. It is further shown that the high correlations in the Brown model are exactly those occurred in the (Legendre) polynomial APs. According to the correlation analyses, a refined model of in-plane distortion is proposed.

In Chapter 3, a number of simulated and empirical tests are performed on the self-calibration models in photogrammetry. Evaluation strategies of the in-situ airborne camera calibration are suggested. The empirical tests of airborne camera calibration demonstrate the high performance of the Lgendre and the Fourier self-calibration models, whose advantages are demonstrated over the conventional counterparts. Both the Legendre and the Fourier models are flexible, generic and effective to calibrate the distortion of most digital frame airborne cameras (including the DMC, DMC II, UltraCamX, UltraCamXp, DigiCAM cameras and so on). The advantages of the Fourier APs lie in that they usually need fewer APs and obtain more reliable calibration of image distortion. The tests in close range photogrammetry confirm the theoretical analyses of correlations in Chapter 2. It is shown that the principal point can be reliably and precisely located in a self-calibration under appropriate image configurations, disregarding the high correlations with the decentering distortion. The refined in-plane distortion model is advantageous in reducing the correlation with focal length and improving the calibration of it. The good performance of the combined "Radial + Legendre" and "Radial + Fourier" models are demonstrated. Discussions are made on the advantages and disadvantages of the physical and the mathematical self-calibration models.

Camera auto-calibration in computer vision is studied in Chapter 4. A new method is presented for camera auto-calibration from N≥3 views, by given image correspondences and zero skew parameter only. This method is essentially based on the fundamental matrix and the three (dependent) constraints derived from the rank-2 essential matrix. The main virtues of this method are threefold. First, a recursive strategy is performed subsequently to a coordinate transformation. The recursion first estimates focal length and aspect ratio, and then calculates principal point by fixing the estimate of focal length and aspect ratio. The principal point estimate returns to contribute to computing focal length and aspect ratio. Second, the optimal geometric constraints are selected using error propagation analyses. Third, the Levenberg–Marquardt algorithm is adopted for the fast final refinement of the four internal parameters. This method is fast and efficient to derive a unique calibration. Besides, we propose a new idea of the focal length calibration from two views without the knowledge of principal point. The coordinate transformation appears to play a critical role in this two-view focal length calibration. While the auto-calibration and the two-view calibration methods are not fully mature, their promising potential is demonstrated in both simulation and practical experiments. Discussions are made on future improvement.

Finally, this work is summarized. Discussions are made on the self-calibration models in photogrammetry, the advantages and disadvantages of the analytical methods in photogrammetry and computer vision, and future outlooks.

2 Self-Calibration Models in Photogrammetry: Theory

"Mathematics, rightly viewed, possesses not only truth, but supreme beauty."

—— Bertrand Russell (1872 – 1970).

2.1 Self-calibration models

2.1.1 Distortion modeling

The mathematical fundamentals of photogrammetry are the collinearity equations (1.4). The distortion terms, Δx and Δy, are two-variable functions whose forms are unknown. They need to be represented by specific models, i.e., self-calibration models.

Generally speaking, there are *physical* and *mathematical* approaches to develop self-calibration models. If precise knowledge on distortion is available and the pattern of distortion is evident, the physical modeling is often favored and distortion can be precisely represented by an exact function. Otherwise, we need to approximate the unknown distortion function via abstract mathematical modeling techniques. Both physical and mathematical approaches have advantages and disadvantages. On the one hand, the physical approach, whose efficiency depends heavily on the knowledge on distortion, is able to model the major significant distortion. The physical models are usually precise and compact. Yet, there might be minor distortion missed in a physical model. The physical modeling may not work if the distortion pattern is not apparent. On the other hand, the mathematical approach is independent on the physical sources of distortion and can thus be generally effective. Nevertheless, the mathematical models may need more unknown parameters than the physical counterparts, and they may be involved in overparameterization. The combination of both modeling approaches can be effective and flexible in practice. Correlations should be taken into account in developing any distortion model.

These two modeling approaches have factually been used, implicitly or explicitly, in developing all the existing distortion models. An excellent example of the physical models is the Brown self-calibration model (Brown, 1971), and two mathematical models are those by Ebner (1976) and Grün (1978).

2.1.2 Self-calibration: a mathematical view

The unknown distortion can be approximated via the mathematical modeling approach. As known, there are several groups of basis functions available in mathematics and their combinations can well approximate any function. The distortion can thus be modeled by a linear combination of specific basis functions. The unknown coefficients of the linear combination are computed in the adjustment process; or in a loose sense, the coefficients can be fixed by the noisy image measurements during the adjustment. This quite resembles the problem of least-squares fitting to the irregular spaced data in mathematics (see Rao & Toutenburg (1999) for the mathematical materials on least-squares fitting). Therefore, photogrammetric self-calibration (or building self-calibration models) can – to a very large

extent – be considered as a *function approximation* or, more precisely, a *curve fitting* problem in mathematics.

Function approximation is the main mathematical principle used in developing new self-calibration models. Its significance arises throughout the whole chapter and even in constructing the physical self-calibration models. Many interesting and valuable observations can be found from the viewpoint of the approximation theory.

Before proceeding to establishing new self-calibration models, the function approximation theory and the mathematical basis functions are briefly introduced in the following two subsections (more materials are given in such as Itō (1993) and Oliver et al. (2010)).

2.1.3 Function approximation theory

The principle of function approximation is very useful in applied mathematics, computer science and many engineering disciplines. In general, function approximation is concerned with how functions can be best approximated with other simpler functions, and with quantitatively characterizing the errors introduced thereby. The meanings of best and simpler depend on the application. Briefly speaking, the simple functions (algebraic polynomials for example) often have desirable properties, such as inexpensive computation, continuity, integrability and limit values. The best approximation depends on the norm of the function space (or loosely speaking, the definition of the distance between functions). Typical choices of norm in the function space include the minimax norm (uniform norm), least-squares norm (Euclidean norm) and mean norm (Manhattan norm).

The function approximation problems can be categorized into two major classes, depending on whether the target function is known or not. First, for the known target function, the approximation investigates how certain known functions can be approximated by a specific class of functions. Second, the explicit form of the target function is unknown and a set of sample points is provided. The problems of this type include interpolation, extrapolation, curve fitting and so on.

Therefore, photogrammetric self-calibration is a function approximation problem of the second type, since the target distortion function is unknown; the least-squares norm (Euclidean norm) should be adopted, since calibration is to minimize the image residuals in the least-squares sense.

2.1.4 Mathematical basis functions

In mathematics, a basis function is an element of a particular basis for a function space. Every function in the function space can be represented as a linear combination of basis functions. A few sets of mathematical basis functions are briefly introduced as follows.

Algebraic polynomials

A polynomial is a mathematical expression involving a sum of finite powers in one or more variables multiplied by coefficients. A univariate polynomial is given by

$$a_n x^n + a_{n-1} x^{n-1} + \cdots + a_1 x + a_0 \tag{2.1}$$

where a_i $(i = 0, 1, \ldots, n)$ are the coefficients.

Rational functions

A rational function is any function which can be written as the ratio of two polynomial functions. A univariate rational function $f(x)$ is

$$f(x) = \frac{P(x)}{Q(x)} \tag{2.2}$$

where $P(x)$ and $Q(x)$ are two polynomials.

Wavelet functions

A wavelet is a wave-like oscillation, which is to analyze according to amplitude. The amplitude starts at zero, increases and then decreases back to zero. Wavelet functions may be considered as the forms of time-frequency representation. They are quite useful in signal processing.

Three sets of basis functions from the Laplace's equation

The Laplace's equation is a second-order partial differential equation named after the French mathematician Pierre-Simon Laplace. It is written as

$$\Delta f = 0 \tag{2.3}$$

where Δ is the Laplace operator and f is a scalar function. The form of Laplace' equation varies in different coordinate systems. In the *Cartesian coordinates* (x, y, z), it is

$$\Delta f = \frac{\partial^2 f}{\partial x^2} + \frac{\partial^2 f}{\partial y^2} + \frac{\partial^2 f}{\partial z^2} = 0. \tag{2.4}$$

In the *cylindrical coordinates* (r, z, φ), it is

$$\Delta f = \frac{1}{r}\frac{\partial}{\partial r}\left(r\frac{\partial f}{\partial r}\right) + \frac{1}{r^2}\frac{\partial^2 f}{\partial \varphi^2} + \frac{\partial^2 f}{\partial z^2} = 0. \tag{2.5}$$

And in the *spherical coordinates* (ρ, θ, φ), it is

$$\Delta f = \frac{1}{\rho^2}\frac{\partial}{\partial \rho}\left(\rho^2\frac{\partial f}{\partial \rho}\right) + \frac{1}{\rho^2 \sin\theta}\frac{\partial}{\partial \theta}\left(\sin\theta\frac{\partial f}{\partial \theta}\right) + \frac{1}{\rho^2 \sin\theta}\frac{\partial^2 f}{\partial \varphi^2} = 0. \tag{2.6}$$

Different solutions of the Laplace's equation can be derived in different coordinates. Particularly,

- the Fourier series are obtained from (2.4) in the Cartesian coordinates;
- the Bessel functions (also known as cylindrical harmonics) are obtained from (2.5) in the cylindrical coordinates; and
- the spherical harmonics are obtained from (2.6) in the spherical coordinates.

Each set of the solutions forms a group of *orthogonal* basis functions in their specific coordinates. In particular, the Fourier series in two-dimensional Cartesian coordinates are

$$cos(mx + ny), sin(mx + ny); \quad m, n = 0, \pm 1, \pm 2, \dots. \tag{2.7}$$

The spherical harmonics in two-dimensional spherical coordinates (known as circular harmonics) are

$$r^n \cos m\theta, r^n \sin m\theta; \quad m, n = 0, 1, 2, \dots. \tag{2.8}$$

Notice the difference between the Fourier series and the circular harmonics, though both are trigonometric functions.

2.2 Legendre self-calibration model

Algebraic polynomials are adopted as basis functions to approximate distortion in this section. This is inspired somehow by the historical prevalence of the polynomial self-calibration models proposed by Ebner (1976) and Grün (1978).

2.2.1 Orthogonal polynomial approximation

The algebraic polynomial approximation is based on the renowned Weierstrass theorem (Mason & Handscomb, 2002), which is given as follows.

Theorem 1 (Weierstrass Theorem)

Suppose g is a continuous function complex-valued on $[a, b]$. There exists a sequence of polynomials $\{p_n(x)\}_n$ such that

$$\lim_{n \to \infty} p_n(x) = g(x) \tag{2.9}$$

uniformly on $[a, b]$. If g is real-valued, then $\{p_n(x)\}_n$ can be taken real.

A constructive proof of the Weierstrass theorem is given in Appendix D.1. This theorem indicates that any univariate function can be approximated with arbitrary accuracy by a polynomial of sufficiently high degree. Among all the forms of polynomials, the orthogonal polynomials (OPs) are often favored in both theoretical and practical applications due to their orthogonality and numerical stability. An orthogonal polynomial sequence is defined in mathematics as a family of polynomials, such that any two different polynomials in the sequence are orthogonal under certain inner product (see Appendix B). The OPs can be categorized into two types: discrete and continuous. The discrete OPs are orthogonal with respect to finite discrete measurements, while the continuous OPs are orthogonal over a whole region.

For the function approximation problem of the second type, the analytical form of function is unknown while sample measurements are available. The unknown function can be approximated by a combination of OPs. If the number of measurements is close to the degree of the used polynomials, the discrete OPs are usually employed and can be obtained by an orthogonalization process. The discrete OPs are orthogonal on the measured locations only, but not necessarily on others. Else, if the number of the measurements is much larger than the polynomials' degree, the continuous OPs are preferred. More theoretical materials can be seen in Berztiss (1964) and Mason & Handscomb (2002).

Legendre polynomials, denoted by $\{L_m(x)\}_{m=0,1,2,\ldots}$ where m indicates the order, are continuous OPs over $[-1, 1]$:

$$|L_m(x)| \leq 1, -1 \leq x \leq 1$$
$$\int_{-1}^{1} L_m(x) L_n(x) dx = \begin{cases} 0, & m \neq n \\ 1, & m = n \end{cases}. \tag{2.10}$$

Among all polynomials, the Legendre polynomials possess the *optimal* approximation in the least-squares sense, i.e., the minimal (weighted) mean square error (MSE) is obtained by using the Legendre polynomials for function approximation (Mason & Handscomb, 2002). The first few normalized Legendre polynomials are listed in Appendix B.1.

The bivariate OPs can be generalized from the univariate polynomials. They can be much more complicated, depending on the two-dimensional definition domain. Particularly, the two-dimensional

generalization on the rectangular domain turns out to be rather easily straightforward. Namely, if $\{p_m(x)\}_{m=0,1,2,\dots}$ are a series of univariate OPs over $[-1,1]$, then

$$\{p_{m,n}(x,y) = p_m(x)p_n(y)\}_{m,n=0,1,2,\dots} \tag{2.11}$$

are the complete bivariate OPs over the rectangular domain $[-1,1] \times [-1,1]$, satisfying

$$\int_{-1}^{1}\int_{-1}^{1} p_{m,n}(x,y)p_{i,j}(x,y)dxdy = \begin{cases} 1, & if\ m=i\ and\ n=j \\ 0, & else \end{cases}. \tag{2.12}$$

 "Complete" means that any two-variable function can be approximated well by the OPs $\{p_{m,n}(x,y)\}_{m,n=0,1,2,\dots}$, as long as a sufficiently high degree of the OPs has been chosen (Koornwinder, 1975).

2.2.2 Legendre model

Let $2b_x$ and $2b_y$ denote the width and length of the image format, respectively (the unit of $2b_x$ and $2b_y$ is usually metric (meter) or pixel). By scaling we obtain

$$l_m(\bar{x}, b_x) = L_m(\bar{x}/b_x), l_n(\bar{y}, b_y) = L_n(\bar{y}/b_y) \tag{2.13}$$

where $\bar{x}$ and $\bar{y}$ are the corrected coordinates of image measurements[4], and L_m and L_n are the univariate Legendre polynomials. The first few $l_m(\bar{x}, b_x)$ are,

$l_0(\bar{x}, b_x) = 1$

$l_1(\bar{x}, b_x) = \bar{x}/b_x$

$l_2(\bar{x}, b_x) = [3(\bar{x}/b_x)^2 - 1]/2$

$l_3(\bar{x}, b_x) = [5(\bar{x}/b_x)^3 - 3(\bar{x}/b_x)]/2$

$l_4(\bar{x}, b_x) = [35(\bar{x}/b_x)^4 - 30(\bar{x}/b_x)^2 + 3]/8$

$l_5(\bar{x}, b_x) = [63(\bar{x}/b_x)^5 - 70(\bar{x}/b_x)^3 + 15(\bar{x}/b_x)]/8$

$l_6(\bar{x}, b_x) = [231(\bar{x}/b_x)^6 - 315(\bar{x}/b_x)^4 + 105(\bar{x}/b_x)^2 - 5]/16.$

The similar formulae of $\{l_n(\bar{y}, b_y)\}_n$ can be derived as above. Denote

$$f_{m,n} \triangleq f_{m,n}(\bar{x}, \bar{y}; b_x, b_y) = l_m(\bar{x}, b_x)l_n(\bar{y}, b_y). \tag{2.14}$$

Then $\{f_{m,n}\}_{m,n}$ are a series of bivariate OPs over the rectangular frame $[-b_x, b_x] \times [-b_y, b_y]$ and $|f_{m,n}| \leq 1$. By considering the image distortion is typically in the order of μm, $p_{m,n}$ is obtained by multiplying $f_{m,n}$ with 10^{-6} for numerical stability:

---

[4] The term "the corrected coordinates of image measurements" is widely used in the literature of camera calibration in photogrammetry. It indicates the ideal coordinates of image measurements in the ideal collinearity equations (1.3); i.e., the "corrected coordinates" are distortion-free and noise-free. The corrected coordinates are certainly unknown in practice, and they are (approximately) calculated in the iterative adjustment process.

$$p_{m,n} = 10^{-6} f_{m,n}, \qquad |p_{m,n}| \leq 10^{-6}. \tag{2.15}$$

$\{p_{m,n}\}_{m,n}$ can be ordered lexicographically as (2.16), following Koornwinder (1975):

$$
\begin{array}{llll}
p_{0,0} & & & \\
p_{1,0} & p_{0,1} & & \\
p_{2,0} & p_{1,1} & p_{0,2} & \quad . \\
p_{3,0} & p_{2,1} & p_{1,2} & p_{0,3} \\
\dots\,\dots & & &
\end{array}
\tag{2.16}
$$

Obviously,

$$\int_{-b_y}^{b_y} \int_{-b_x}^{b_x} p_{m,n}(x,y) p_{i,j}(x,y) dx dy = 0, \qquad if\ m \neq i\ or\ n \neq j. \tag{2.17}$$

It implies that if the image measurements are densely distributed, then

$$\sum_k p_{m,n}(x_k, y_k) p_{i,j}(x_k, y_k) \approx 0, \ if\ m \neq i\ or\ n \neq j \tag{2.18}$$

which indicates that $\{p_{m,n}\}_{m,n}$ is (almost) orthogonal over all the image measurements.

Therefore, the distortion Δx and Δy in (1.4) could be approximated by the continuous bivariate OPs $\{p_{m,n}\}_{m=0,n=0}^{m=M_x,n=N_x}$ and $\{p_{m,n}\}_{m=0,n=0}^{m=M_y,n=N_y}$ respectively, where M_x, N_x, M_y and N_y are the chosen maximum degrees (these four degrees are not necessarily equal, and $M_x = M_y = M$ and $N_x = N_y = N$ are usually adopted in practice; generally speaking, more complicated the distortion is, larger degrees are required). Further, six of them should be eliminated, as also done in Ebner (1976) and Grün (1978). Specially, the constant terms $p_{0,0}$ in Δx and Δy are nothing but the principal point shift; $p_{1,0}$, $p_{0,1}$, $p_{2,0}$ and $p_{1,1}$ in Δx are highly correlated with $p_{0,1}$, $p_{1,0}$, $p_{1,1}$ and $p_{0,2}$ in Δy, respectively. Thus, the number of the unknown parameters is $(M_x + 1)(N_x + 1) + (M_y + 1)(N_y + 1) - 6$ or $2(M + 1)(N + 1) - 6$.

For example, the APs of $M = N = 5$ are,

$$
\begin{aligned}
\Delta x =\ & a_1 p_{1,0} + a_2 p_{0,1} + a_3 p_{2,0} + a_4 p_{1,1} + a_5 p_{0,2} + a_6 p_{3,0} + a_7 p_{2,1} \\
& + a_8 p_{1,2} + a_9 p_{0,3} + a_{10} p_{4,0} + a_{11} p_{3,1} + a_{12} p_{2,2} + a_{13} p_{1,3} + a_{14} p_{0,4} \\
& + a_{15} p_{5,0} + a_{16} p_{4,1} + a_{17} p_{3,2} + a_{18} p_{2,3} + a_{19} p_{1,4} + a_{20} p_{0,5} + a_{21} p_{5,1} \\
& + a_{22} p_{4,2} + a_{23} p_{3,3} + a_{24} p_{2,4} + a_{25} p_{1,5} + a_{26} p_{5,2} + a_{27} p_{5,3} + a_{28} p_{3,4} \\
& + a_{29} p_{2,5} + a_{30} p_{5,3} + a_{31} p_{4,4} + a_{32} p_{3,5} + a_{33} p_{5,4} + a_{34} p_{4,5} + a_{35} p_{5,5} \\[8pt]
\Delta y =\ & a_2 p_{1,0} - a_1 p_{0,1} + a_{36} p_{2,0} - a_3 p_{1,1} - a_4 p_{0,2} + a_{37} p_{3,0} + a_{38} p_{2,1} \\
& + a_{39} p_{1,2} + a_{40} p_{0,3} + a_{41} p_{4,0} + a_{42} p_{3,1} + a_{43} p_{2,2} + a_{44} p_{1,3} + a_{45} p_{0,4} \\
& + a_{46} p_{5,0} + a_{47} p_{4,1} + a_{48} p_{3,2} + a_{49} p_{2,3} + a_{50} p_{1,4} + a_{51} p_{0,5} + a_{52} p_{5,1} \\
& + a_{53} p_{4,2} + a_{54} p_{3,3} + a_{55} p_{2,4} + a_{56} p_{1,5} + a_{57} p_{5,2} + a_{58} p_{5,3} + a_{59} p_{3,4} \\
& + a_{60} p_{2,5} + a_{61} p_{5,3} + a_{62} p_{4,4} + a_{63} p_{3,5} + a_{64} p_{5,4} + a_{65} p_{4,5} + a_{66} p_{5,5}
\end{aligned}
\tag{2.19}
$$

with 66 unknown parameters ($a_i, i = 1, 2, \dots, 66$).

The model of $M = 4$ and $N = 3$ with 34 APs ($a_i, i = 1, 2, \dots, 34$) are given by

$$\Delta x = a_1 p_{1,0} + a_2 p_{0,1} + a_3 p_{2,0} + a_4 p_{1,1} + a_5 p_{0,2} + a_6 p_{3,0} + a_7 p_{2,1}$$
$$+ a_8 p_{1,2} + a_9 p_{0,3} + a_{10} p_{4,0} + a_{11} p_{3,1} + a_{12} p_{2,2} + a_{13} p_{1,3} + a_{14} p_{4,1}$$
$$+ a_{15} p_{3,2} + a_{16} p_{2,3} + a_{17} p_{4,2} + a_{18} p_{3,3} + a_{19} p_{4,3}$$

$$\Delta y = a_2 p_{1,0} - a_1 p_{0,1} + a_{20} p_{2,0} - a_3 p_{1,1} - a_4 p_{0,2} + a_{21} p_{3,0} + a_{22} p_{2,1}$$
$$+ a_{23} p_{1,2} + a_{24} p_{0,3} + a_{25} p_{4,0} + a_{26} p_{3,1} + a_{27} p_{2,2} + a_{28} p_{1,3} + a_{29} p_{4,1}$$
$$+ a_{30} p_{3,2} + a_{31} p_{2,3} + a_{32} p_{4,2} + a_{33} p_{3,3} + a_{34} p_{4,3}$$

$$(2.20)$$

So far a whole family of self-calibration model has been completely constructed. The input of the model includes the image length and width ($2b_x$ and $2b_y$), and the chosen degrees. This class of self-calibration model is based on the Legendre polynomials and thus named as *Legendre self-calibration model* (or equivalently *Legendre self-calibration APs*). The Legendre self-calibration model of n-th order is defined as that with $M = N = n$.

2.2.3 Discussions on polynomial self-calibration models

As the self-calibration models proposed by Ebner (1976) and Grün (1978) are also based on algebraic polynomials, theoretical discussions can be made on them and the Legendre model.

Based on the "standard" 60% forward overlapping level and a few number of photographic measurements in the analogue time, Ebner and Grün proposed the polynomial self-calibration models of second and fourth orders, respectively. Their models were built on the assumed 3×3 and 5×5 regular "grid points" configurations, respectively. They can be obtained by orthogonalization and elimination of six parameters, and finally get the models of 12 and 44 unknowns, respectively. Obviously, they belong to the *discrete OPs* in the mathematical jargon and they are orthogonal on the grid points only.

However, the continuous OPs should be certainly preferred to the discrete OPs for the self-calibration purpose. It is mainly because that the distortion of a single camera is always assumed to be constant in one block. This homogenous assumption implies that all the measurements of all images are put together into a single image dimension for calibration, as illustrated in Fig. 2.1. For example, for a block containing 50 images, each image contains a small amount of measurements, say around 40. It turns out to be about 2000 measurements usable for self-calibration, much more than the unknown APs which are usually less than 100. The number of total image measurements is far larger than the number of APs in all photogrammetric practices (otherwise, the block will be extremely unstable due to the severe overparameterization). According to the theory of polynomial approximation in Section 2.2.1, the Legendre self-calibration model which is derived from the continuous Legendre OPs is theoretically favored.

Furthermore, the polynomial models by Ebner and Grün can be exactly derived from the principle of polynomial approximation which was although not explicitly mentioned in their work. Particularly, the Ebner APs can be developed via the following steps:

1. use univariate polynomials no higher than the second order: $1, x, x^2$;
2. perform normalization and orthogonalization (neglecting one scale factor);
3. do two-dimensional generalization as (2.14);
4. eliminate two constants and four highly correlated terms; and
5. the Ebner APs are exactly obtained.

The mathematical relation among these three sets of polynomial APs can be further shown. Assume there are $(2m + 1) \times (2m + 1)$ points distributed equidistantly on a *square* image dimension. Let's consider the 2nd-degree monic polynomial $p_2(x)$ (the leading coefficient is one), which corresponds to the term k in the Ebner and Grün APs (see Appendix A) and $p_{2,0}$ in the Legendre APs. Neglecting a scale constant, $p_2(x)$ could be obtained by using the Gram-Schmidt orthogonalization process:
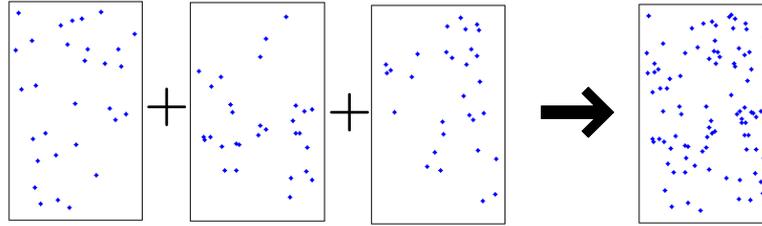
Fig. 2.1 The effect of the homogeneous assumption of image distortion on self-calibration: all the image measurements are put together into a single image dimension.

$$p_2(x) = x^2 - \frac{\sum_{i=-m}^{m} \sum_{j=-m}^{m} (j/m)^2}{\sum_{i=-m}^{m} \sum_{j=-m}^{m} 1} = x^2 - \frac{m+1}{3m}. \tag{2.21}$$

Then,

$$p_2(x) = x^2 - 2/3 = k, \qquad if\ m = 1\ (3 \times 3\ \text{grid points}, Ebner\ APs)$$

$$p_2(x) = x^2 - 1/2 = k, \qquad if\ m = 2\ (5 \times 5\ \text{grid points}, Grün\ APs)$$

$$p_2(x) = x^2 - 1/3 = p_{2,0}, \qquad if\ m \to \infty\ (\text{dense points}, Legendre\ APs).$$

Therefore, the theoretical foundations behind all polynomial APs (Ebner, Grün and Legendre) are the same: polynomial approximation and the Weierstrass theorem. That the polynomial self-calibration models are able to compensate distortion is because that the polynomials can approximate the unknown distortion function. The principle of polynomial approximation is also able to explain why the regular 3×3 and 5×5 point patterns are not a prerequisite for applying the Ebner and Grün APs. The irregular point distribution does not degrade the calibration effect but induces impacts on correlations. Theoretically, the correlations of the Ebner and the Grün APs are larger than those of Legendre APs. This will be confirmed in the practical tests in Chapter 3.

In contrast to the Ebner or the Grün APs which are single-order APs, the whole family of Legendre APs offers much flexibility to calibrate more complex image distortion, particularly when high degree is desired. The Legendre APs suit the rectangular image format and are orthogonal over the whole image format. Compared to the two historical counterparts, the Legendre self-calibration model is more flexible and more effective. Particularly, the Legendre model can also be considered as a superior generalization of the models by Ebner and Grün.

Another interesting issue is on using alternative orthogonal polynomials rather than the Legendre polynomials as bases to build self-calibration models. Amongst them the Chebyshev polynomials of the first kind (see Appendix B.2) can be most attractive. While the Chebyshev polynomials possess the optimal approximation in the minimax sense, the Legendre polynomials are optimal in the least-squares sense. Therefore, the Legendre polynomials are theoretically advantageous since camera calibration is to minimize the image residuals in the least-squares sense. Our empirical experiences also show that, although there is no significant difference between applying these two sets of polynomials, the application of the Chebyshev polynomials involves higher correlations and is less stable than the Legendre polynomials.

In a word, three main theoretical conclusions can be drawn. First, the mathematical foundations for all polynomial APs are the same: polynomial approximation and the Weierstrass theorem. Second, the continuous OPs rather than the discrete OPs should be favored to build self-calibration models, due to that the number of all image measurements is far larger than the number of APs. Third, the Legendre self-calibration model is preferred to other polynomial models, due to that the Legendre polynomials obtain optimal approximation in the least-squares sense.

2.3 Fourier self-calibration model

2.3.1 Optimal basis functions

Principally speaking, every set of basis functions introduced in Section 2.1.4 can build a self-calibration model. Then, a natural question is whether there is a set of optimal basis functions which should be preferred for self-calibration? The 'optimal basis functions' stand for at least

(1) that their self-calibration model is able to (almost) fully compensate distortion under certain conditions;

(2) that their self-calibration model follows strictly the approximation theory; and

(3) that their self-calibration model does not cause severe overparameterization in practice.

The first condition requires that distortion can be approximated by a combination of these basis functions. The second one requires that all the APs in $\Delta x(\bar{x}, \bar{y})$ should be independent of those in $\Delta y(\bar{x}, \bar{y})$. In fact, one function, say $f_1(\bar{x}, \bar{y})$, is used to approximate $\Delta x(\bar{x}, \bar{y})$ and another $f_2(\bar{x}, \bar{y})$ is to approximate $\Delta y(\bar{x}, \bar{y})$. From the viewpoint of approximation, all the coefficients of these two functions, $f_1(\bar{x}, \bar{y})$ and $f_2(\bar{x}, \bar{y})$, should thus be fully free (independent of any others). The third condition requires that the basis functions should use as few terms as possible to approximate distortion. Too many terms indicate mathematically very slow approximation and may practically cause serious overparameterization.

All sets of basis functions satisfy, at least theoretically, the first rule by using the terms of sufficiently high order. However, not all of them meet the second and the third rules. For example, the algebraic polynomials do not fully follow the second rule since they have to eliminate four highly correlated terms. This is detailed as follows.

The first five terms of the two-dimensional Legendre polynomials are

$$
\begin{aligned}
\Delta x_P &: a_0 + a_1 p_{1,0} + a_2 p_{0,1} + a_3 p_{2,0} + a_4 p_{1,1} + a_5 p_{0,2} \\
\Delta y_P &: b_0 + b_1 p_{1,0} + b_2 p_{0,1} + b_3 p_{2,0} + b_4 p_{1,1} + b_5 p_{0,2}
\end{aligned}. \tag{2.22}
$$

It can be shown in theoretical study and simulation experiments that six terms of (2.2) must be eliminated to build polynomial self-calibration models, due to

- that the constants a_0 and b_0 are merely the principal point shift Δx_0 and Δy_0;
- that a_1 and b_2 are highly correlated in the presence of Δf;
- that a_2 and b_1 are highly correlated due to the exterior rotation angle κ;
- that a_3 and b_4 are highly correlated due to Δx_0 and the exterior rotation angle φ; and
- that a_4 and b_5 are highly correlated due to Δy_0 and the exterior rotation angle ω.

Therefore, two constants are removed since they are nothing more than the principal point shift (removal of constant terms never impacts the approximation), and four parameters must be eliminated due to the high correlations. Consequently, the first five terms of the Legendre self-calibration APs are

$$
\begin{aligned}
\Delta x_P &: a_1 p_{1,0} + a_2 p_{0,1} + a_3 p_{2,0} + a_4 p_{1,1} + a_5 p_{0,2} \\
\Delta y_P &: a_2 p_{1,0} + (-a_1) p_{0,1} + b_3 p_{2,0} + (-a_3) p_{1,1} + (-a_4) p_{0,2}
\end{aligned}. \tag{2.23}
$$

Note that all the four high correlations are linked to the terms x, y and xy. These correlation analyses hold for all the polynomial self-calibration models including those by Ebner (1976) and Grün (1978)[5].

---

[5] It should be noted that these correlation analyses can only be performed in a simulation block of integrated sensor orientation. Without the direct observations of the EO parameters, it may lead to incorrect interpretations of the elimination, such as that in Grün (1978) "…the rejection of those parameters which correspond to the 6 elements of exterior orientation …".

The elimination of the four highly correlated terms is an indispensable step to construct the polynomial APs. It imposes four constraints on the polynomial APs. This is however a theoretical deficiency. According to the polynomial approximation principle and the Weierstrass theorem, all the parameters in Δx_P should be *independent* of those in Δy_P for the strict approximation purpose. In other words, the theoretical number of the unknown APs in the Ebner, the Grün and the fifth order Legendre models should be 16, 48 and 70, rather than 12, 44 and 66, respectively (by removing two constants). The elimination of the highly correlated terms degrades the rigorousness of the polynomial APs, and it may cause negative effects on calibration. Algebraic polynomials are therefore not the optimal basis functions for self-calibration purpose. This view was shared in Ziemann (1986) that algebraic polynomials "are undesirable from a mathematical point of view because of the high correlation between the different terms".

Moreover, the wavelet and rational functions are not favored by the reason that their forms are rather inconvenient and their derivatives are complicated. These functions increase computation and can burden bundle adjustment. For the three sets of basis functions from the Laplace's equation, the Fourier series should be certainly favored since of the Cartesian image coordinate system. This mathematical insight also explains why the APs using spherical harmonics (El-Hakim & Faig, 1977) are less significant in practice. Actually, the APs using spherical harmonics encounter the similar difficulties of high correlations as those in the algebraic polynomial APs. They include the terms

$$\begin{aligned}
\Delta x_H : &\ a_1 r \cos\theta + a_2 r \sin\theta + a_3 r^2 \cos 2\theta + a_4 r^2 \sin 2\theta \\
&= a_1 x + a_2 y + a_3 (2x^2 - r^2) + a_4 xy \\
\Delta y_H : &\ b_1 r \cos\theta + b_2 r \sin\theta + b_3 r^2 \cos 2\theta + b_4 r^2 \sin 2\theta \\
&= b_1 x + b_2 y + b_3 (r^2 - 2y^2) + b_4 xy
\end{aligned} \tag{2.24}$$

where the parameters b_1 and b_2 must be replaced by a_2 and $-a_1$, respectively (similar to (2.23)). The correlations between a_3 and b_4, and between a_4 and b_3, can be fairly high.

Therefore, the Fourier series should be chosen as the theoretically optimal basis functions to develop self-calibration models.

2.3.2 Fourier model

Parallel to the Weierstrass theorem for the algebraic polynomial approximation, the Fourier theorem is the fundamental principle for the approximation via the Fourier series.

Theorem 2 (Fourier Theorem)

Suppose g is a continuous real function whose period is 2π. For every $\varepsilon > 0$, there exists an integral number N, $\{a_n\}$ and $\{b_n\}$ ($n = 0, 1, 2, \dots, N$) such that

$$\left| \sum_{n=1}^{N} (a_n \cos nx + b_n \sin nx) - g(x) \right| < \varepsilon \tag{2.25}$$

Particularly, if g is valued on $\left[-\pi + a, \pi + a\right]$ where a is an arbitrary real number, (2.25) holds uniformly for any $x \in \left[-\pi + a, \pi + a\right]$.

A proof of the Fourier theorem is given in Appendix D.2.

Bivariate Fourier series are given as

$$\cos(mx + ny), \sin(mx + ny); \quad m, n = 0, \pm 1, \pm 2, \dots \tag{2.26}$$

where $x, y \in [-\pi, \pi]$. The Fourier theorem in two-variables indicates that any two-variable functions defined in $[-\pi, \pi] \times [-\pi, \pi]$ can be approximated with arbitrary accuracy by the linear combination of the bivariate Fourier series of sufficiently high degree.

Denote

$$u = \bar{x}\pi/b_x, v = \bar{y}\pi/b_y, \quad u, v \in [-\pi, \pi]$$
$$c_{m,n} \triangleq 10^{-6}\cos(mu + nv), s_{m,n} \triangleq 10^{-6}\sin(mu + nv) \tag{2.27}$$

where the factor 10^{-6} accounts for the order of distortion magnitude, as done in the Legendre self-calibration model. The $c_{m,n}$ and $s_{m,n}$ satisfy the orthogonal conditions (2.28) which indicate $c_{m,n}$ and $s_{m,n}$ are orthogonal over the whole image dimension:

$$\int_{-b_y}^{b_y} \int_{-b_x}^{b_x} c_{m,n}c_{m',n'}dxdy = 0, \ if \ m \neq m' or \ n \neq n'$$
$$\int_{-b_y}^{b_y} \int_{-b_x}^{b_x} s_{m,n}s_{m',n'}dxdy = 0, \ if \ m \neq m' or \ n \neq n'. \tag{2.28}$$
$$\int_{-b_y}^{b_y} \int_{-b_x}^{b_x} c_{m,n}s_{m',n'}dxdy = 0$$

The linear combination of the bivariate Fourier series can be used to approximate the unknown distortion functions Δx and Δy. The general form of self-calibration models is given as

$$\Delta x = \sum_{m=1}^{M}\sum_{n=-N}^{N}(a_{m,n}c_{m,n} + b_{m,n}s_{m,n}) + \sum_{n=1}^{N}(a_{0,n}c_{0,n} + b_{0,n}s_{0,n})$$
$$\Delta y = \sum_{m=1}^{M}\sum_{n=-N}^{N}(a'_{m,n}c_{m,n} + b'_{m,n}s_{m,n}) + \sum_{n=1}^{N}(a'_{0,n}c_{0,n} + b'_{0,n}s_{0,n}) \tag{2.29}$$

where $a_{m,n}$, $b_{m,n}$, $a'_{m,n}$ and $b'_{m,n}$ are the unknown coefficients (parameters) to be computed in adjustment. M and N are the maximum degrees chosen by the users. The number of unknown APs is $2(2M(2N + 1) + 2N) = 4(2MN + M + N)$ (although different degrees M_x, N_x, M_y and N_y can be introduced as those in the Legendre model, $M_x = M_y = M$ and $N_x = N_y = N$ are used in practice).

As this family of self-calibration APs (with respect to M and N) is established on the base of the Fourier series, it is named as *Fourier self-calibration model* (or *Fourier self-calibration APs*). The n-th order Fourier model is defined as that with $M = N = n$.

Particularly, the Fourier model of $M = N = 1$ (16 APs) is given with the lexicographic order:

$$\Delta x = a_1 c_{1,0} + a_2 c_{0,1} + a_3 c_{1,-1} + a_4 c_{1,1}$$
$$+ a_5 s_{1,0} + a_6 s_{0,1} + a_7 s_{1,-1} + a_8 s_{1,1}$$
$$\Delta y = a_9 c_{1,0} + a_{10} c_{0,1} + a_{11} c_{1,-1} + a_{12} c_{1,1} \tag{2.30}$$
$$+ a_{13} s_{1,0} + a_{14} s_{0,1} + a_{15} s_{1,-1} + a_{16} s_{1,1}$$

The Fourier model of $M = N = 2$ with 48 unknown APs are given by

$$\Delta x = a_1 c_{1,0} + a_2 c_{0,1} + a_3 c_{2,0} + a_4 c_{1,-1} + a_5 c_{1,1} + a_6 c_{0,2}$$
$$+ a_7 c_{1,2} + a_8 c_{1,-2} + a_9 c_{2,-1} + a_{10} c_{2,1} + a_{11} c_{2,-2} + a_{12} c_{2,2}$$
$$+ a_{13} s_{1,0} + a_{14} s_{0,1} + a_{15} s_{2,0} + a_{16} s_{1,-1} + a_{17} s_{1,1} + a_{18} s_{0,2}$$
$$+ a_{19} s_{1,2} + a_{20} s_{1,-2} + a_{21} s_{2,-1} + a_{22} s_{2,1} + a_{23} s_{2,-2} + a_{24} s_{2,2}$$
$$\Delta y = a_{25} c_{1,0} + a_{26} c_{0,1} + a_{27} c_{2,0} + a_{28} c_{1,-1} + a_{29} c_{1,1} + a_{30} c_{0,2} \tag{2.31}$$
$$+ a_{31} c_{1,2} + a_{32} c_{1,-2} + a_{33} c_{2,-1} + a_{34} c_{2,1} + a_{35} c_{2,-2} + a_{36} c_{2,2}$$
$$+ a_{37} s_{1,0} + a_{38} s_{0,1} + a_{39} s_{2,0} + a_{40} s_{1,-1} + a_{41} s_{1,1} + a_{42} s_{0,2}$$
$$+ a_{43} s_{1,2} + a_{44} s_{1,-2} + a_{45} s_{2,-1} + a_{46} s_{2,1} + a_{47} s_{2,-2} + a_{48} s_{2,2}$$

An intermediate model between the first and the second orders is given in (2.32) below where it contains 32 APs.

$$\Delta x = a_1 c_{1,0} + a_2 c_{0,1} + a_3 c_{2,0} + a_4 c_{1,-1} + a_5 c_{1,1} + a_6 c_{0,2}$$
$$+a_7 c_{1,2} + a_8 c_{1,-2} + a_9 c_{2,-1} + a_{10} c_{2,1} + a_{11} c_{2,-2} + a_{12} c_{2,2}$$
$$+a_{13} s_{1,0} + a_{14} s_{0,1} + a_{15} s_{1,-1} + a_{16} s_{1,1}$$

$$\Delta y = a_{17} c_{1,0} + a_{18} c_{0,1} + a_{19} c_{2,0} + a_{20} c_{1,-1} + a_{21} c_{1,1} + a_{22} c_{0,2}$$
$$+a_{23} c_{1,2} + a_{24} c_{1,-2} + a_{25} c_{2,-1} + a_{26} c_{2,1} + a_{27} c_{2,-2} + a_{28} c_{2,2}$$
$$+a_{29} s_{1,0} + a_{30} s_{0,1} + a_{31} s_{1,-1} + a_{32} s_{1,1}$$

(2.32)

For the Fourier self-calibration model, all the APs in Δx are independent of those in Δy and there is no need to eliminate any APs. Therefore, the Fourier APs completely and strictly obey their mathematical principles while the polynomial APs do not. From a mathematical point of view, the Fourier APs are more rigorous and more desirable for camera self-calibration.

2.3.3 Discussions on mathematical self-calibration models

We have insofar developed two groups of mathematical self-calibration models, i.e., the Legendre and the Fourier models. Discussions are made on their commons and distinctions in this subsection.

Mathematical fundamentals of self-calibration models

There exist solid mathematical fundamentals behind the polynomial (including the Ebner, Grün and Legendre models) and the Fourier self-calibration models. The basic principle is utilizing the basis functions to approximate the unknown distortion function. The approximation theory guarantees that the Legendre and the Fourier models of appropriate degree are capable to approximate any distortion. Although the mathematical APs are sometimes dubbed "empirical" (McGlone et al., 2004), the Legendre and the Fourier self-calibration models are in fact more objective in many senses than the physical self-calibration models. For example, the performance of these mathematical models is quite independent of any empirical knowledge on distortion.

Theoretical rigorousness

As seen previously, algebraic polynomials have to eliminate four highly correlated terms to construct the self-calibration models while the Fourier series do not. This fact can also be interpreted from the function profiles of the univariate algebraic polynomials and the Fourier series. In Fig. 2.2 it is plotted the first six Legendre polynomials (left), the first six Chebyshev polynomials of the first kind (middle), and the first five terms of Fourier series (right) (all the zero-order constants are ignored). The Legendre polynomials and the Chebyshev polynomials are denoted by '$L_n(x)$' and '$T_n(x)$' (n indicates the polynomial order), respectively.

The most distinction found in Fig. 2.2 is that, in contrast to the two polynomials, the Fourier series contain no *linear* term. The linear terms, x and y, and their two-dimensional multiplication xy, cause high correlations with the three IO parameters (Δx_0, Δy_0 and Δf), as shown in (2.23). In fact, any self-calibration model including the terms x, y and xy gives rise to high correlations with the three IO parameters, if not following (2.23) to minimize correlations. It is a distinct characteristic of the camera orientation and independent of block geometry. The disappearance of the linear terms (and their multiplication) in the Fourier series makes that the Fourier model does not need to eliminate any term. Therefore, the Fourier self-calibration model is theoretically more rigorous than the Legendre counterpart.

It is also noteworthy that the curves of those two polynomials and the Fourier series appear somehow similarly with particular respect to the number of the peaks. Following the order of the algebraic polynomials, the Fourier series on $[-\pi, \pi]$ can be 'naturally' ordered as

$$\cos x, \sin x, \cos 2x, \sin 2x, \cos 3x, \sin 3x, \dots. \tag{2.33}$$

In other words, $\sin nx$ can be considered to be one-order higher than $\cos nx$, but one-order lower than $\cos(n+1)x$ $(n = 1, 2, \dots)$. This is the exact rule how to derive the intermediate formulae (2.32) between the first and the second orders. The formulae (2.32) is factually that $c_{2,k}$ and $c_{k,2}$ $(k = -2, -1, \dots, 2)$ are added to the first order (2.30), or that $s_{2,k}$ and $s_{k,2}$ $(k = -2, -1, \dots, 2)$ are removed from the second order (2.31).
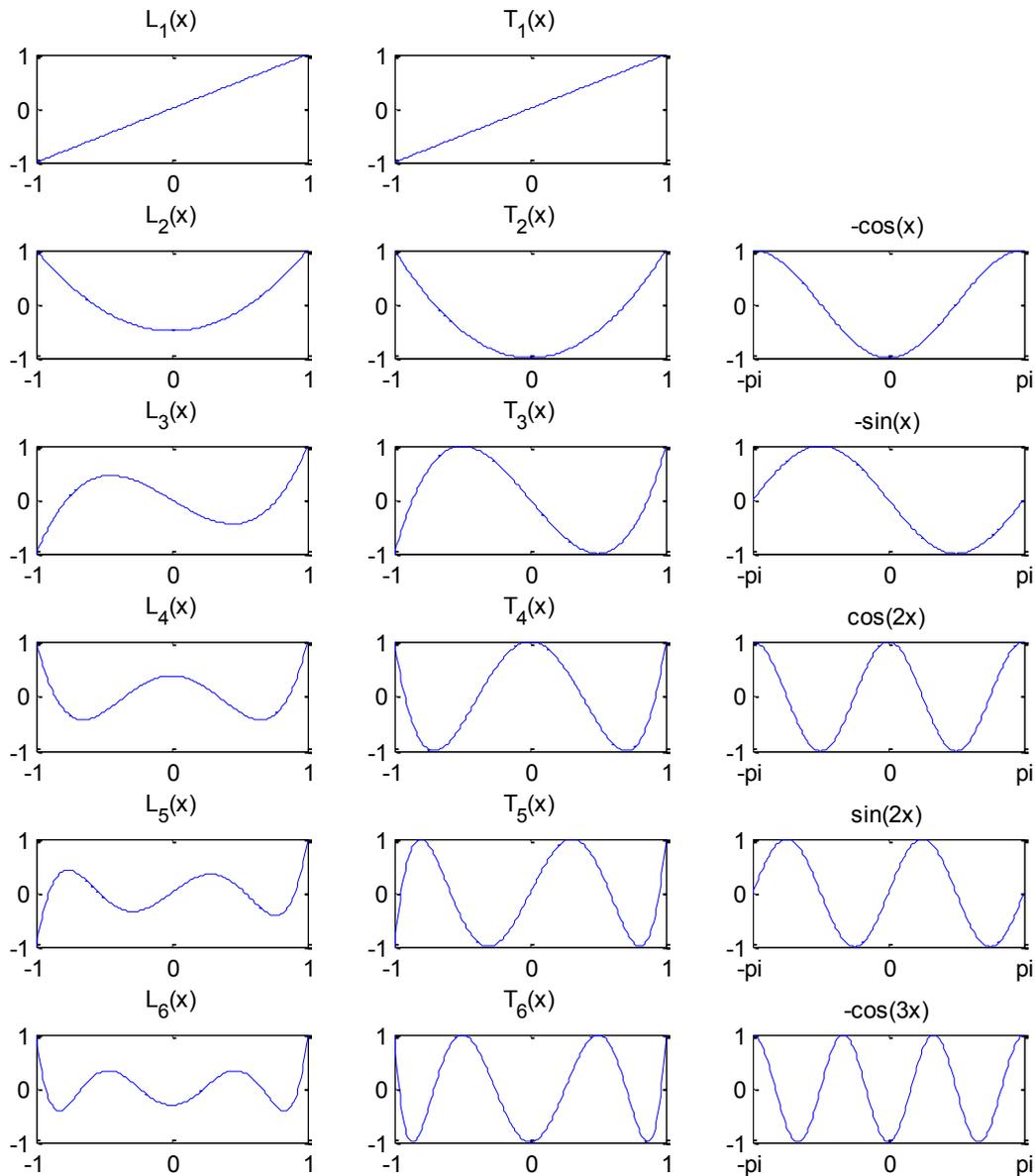

Fig. 2.2 The function profiles of the first few Legendre polynomials (left), the Chebyshev polynomials of the first kind (middle) and the Fourier series (right).

Independence of distortion sources

The Legendre and the Fourier self-calibration models (as well as the models by Ebner, Grün and El-Hakim & Faig) are built on the base of the abstract principle of function approximation. They are thus independent of the distortion sources and generically effective. This is the exact reason why the APs by Ebner and Grün can work well in the digital era, although they are originated for analogue camera calibration. This is also a significant advantage which can be of vital importance when precise knowledge on distortion is unavailable.

APs' interpretation

Ebner (1976) illustrated the geometric effects of his second-order polynomial APs. However, these illustrations should *not* be viewed as the interpretations like those of the physical APs. Generally speaking, the APs of both the polynomial and the Fourier models merely follow the mathematical principle of function approximation, and they don't have any physical meaning (it is noted that having physical meanings implies depending on distortion sources, and vice versa). There is no need to interpret those mathematical APs, while the illustrations might be slightly helpful for empirical understanding.

Overparameterization and underparameterization

Overparameterization is always a major concern whenever the self-calibration APs are applied. In personal opinion, there are two relevant but different types of overparameterization. One is in the common mathematical sense that the random error is over-fitted as the systematic error; another is in the photogrammetric sense that the block geometry is deformed by the excessive use of APs. The first type is generally trivial since the image measurements are far more than the unknown APs (see section 2.2.3). The second type is mainly dependent on the configurations of block geometry, such as the distribution of GCPs and the overlapping levels. Generally, increasing the number of GCPs and the overlapping levels helps the block against overparameterization.

As the opposite of overparameterization, underparameterization should deserve similar importance. Underparameterization implies that self-calibration model is inadequate for distortion compensation. It can also result in degraded accuracy and incorrect system calibration.

For the Legendre and the Fourier models, overparameterization and underparamterization can be simply interpreted as overly high and too low degrees, respectively. The degree should be decreased if overparameterization is observed, and should be increased if underparamterization occurs. The appropriate degree of the Legendre and the Fourier models needs to be chosen in order to avoid overparameterization and underparamterization.

Then, an open question is that how many degrees of the Legendre and the Fourier models should be chosen in practice? Generally, there is no certain answer which depends on particular circumstances. From our empirical experiences (maybe a rule of thumb), the Legendre model of fourth and fifth orders, and the Fourier model of first and second orders and the intermediate (2.32), are sufficient for many applications in aerial photogrammetry. The risk of overparameterization should be cautioned if one utilizes the Legendre and the Fourier models of even higher orders.

Radial distortion

The radial distortion ((2.37) below) is known as a major distortion in many frame-format cameras. Although the Legendre and the Fourier self-calibration models are generically effective to calibrate any type's distortion, it is unwise to *directly* use them to calibrate the symmetric radial distortion. The main reason is that the Legendre APs of over sixth-order (over 92 parameters), or the Fourier APs of over third-order (over 96 parameters) may be needed to approximate the radial distortion to a good accuracy. This can cause severe damages of overparameterization.

Instead, we strongly recommend that the Legendre and the Fourier APs should be utilized together with the radial distortion parameters to calibrate the image distortion which maintains significant radial distortion. These combined models (or called "mixed models") "Radial + Legendre" and "Radial + Fourier" can be very efficient and highly flexible. On the one hand, these two combined models are capable to calibrate the radial distortion (if present) and others (by the Legendre or the Fourier APs), with little price of overparameterization. On the other hand, the radial distortion parameters are low correlated with the EO and other IO parameters; they do not increase the risk of high correlations. As will be seen in the next chapter, these combined models work very well even in calibrating the typical lenses in close range photogrammetry.

2.4 Self-calibration models in close range photogrammetry

Notwithstanding slight variations, the self-calibration model developed by Duane. C. Brown is the 'standard' model widely accepted in close range photogrammetry. It is efficient and powerful to calibrate a huge range of lenses. Yet, a main disadvantage of the Brown model is the well-known high correlations between different parameters. The high correlations and their effects on self-calibration are analyzed in this section.

2.4.1 Brown self-calibration model

The Brown self-calibration model includes the three IO parameters (Δx_0, Δy_0 and Δf), the symmetric radial distortion and the decentering distortion. The principle of function approximation is significant as well in the following construction of the Brown model.

Radial distortion

The radial distortion is a major geometric error of many cameras. It is caused by variations in refraction at each individual component lens. It is a radial function, denoted by $P_r(r)$. The corrections in the two image coordinates are Δx_r and Δy_r:

$$\Delta x_r = \cos \phi \, P_r(r) = \frac{\bar{x}}{r} P_r(r), \; \Delta y_r = \sin \phi \, P_r = \frac{\bar{y}}{r} P_r(r) \tag{2.34}$$

where $\bar{x}$ and $\bar{y}$ are the corrected coordinates, $r^2 = \bar{x}^2 + \bar{y}^2$, and ϕ is the angle between the x axis and the radial vector to the image point $(\bar{x}, \bar{y})$.

The profile function $P_r(r)$ can certainly be approximated by an algebraic polynomial (see the Weierstrass theorem in Section 2.2.1):

$$P_r(r) = \sum_{n=0}^{\infty} a_n r^n \tag{2.35}$$

where $a_n (n = 0, 1, 2, ...)$ are the coefficients. As the three odd-order terms are sufficient in most practices, (2.35) and (2.34) are simplified as (2.36) and (4.7), respectively:

$$P_r(r) \approx \Delta r = K_1 r^3 + K_2 r^5 + K_3 r^7 \tag{2.36}$$

$$\begin{aligned} \Delta x_r &= \bar{x}(K_1 r^2 + K_2 r^4 + K_3 r^6) \\ \Delta y_r &= \bar{y}(K_1 r^2 + K_2 r^4 + K_3 r^6) \end{aligned} \tag{2.37}$$

Decentering distortion

A lack of centering of lens elements along the optical axis gives rise to the decentering distortion. According to the Conrady's model (Conrady, 1919), the decentering distortion contains the radial and tangential components, denoted by Δd_r and Δd_t:

$$\Delta d_r = 3 P_d(r) \sin(\phi - \phi_0), \ \Delta d_t = P_d(r) \cos(\phi - \phi_0) \tag{2.38}$$

where $P_d(r)$ is the profile function of the decentering distortion, and ϕ_0 is the angle between the x axis and the axis of the maximum tangential distortion.

Then, the effects of the decentering distortion in two image coordinates, denoted by Δx_d and Δy_d, are given as

$$\begin{aligned} \Delta x_d &= \Delta d_r \cos \phi - \Delta d_t \sin \phi \\ \Delta y_d &= \Delta d_r \sin \phi + \Delta d_t \cos \phi \end{aligned} \tag{2.39}$$

Analogue to (2.35), $P_d(r)$ is approximated by a polynomial as well. Specifically, it can be well approximated by a series of the even-order polynomials:

$$P_d(r) \approx J_1 r^2 + J_2 r^4 + J_3 r^6 + \cdots. \tag{2.40}$$

From (2.38) – (2.40), we can obtain

$$\begin{aligned} \Delta x_d &= [P_1(r^2 + 2\bar{x}^2) + 2P_2\, \bar{x}\, \bar{y}][1 + P_3 r^2 + \cdots] \\ \Delta y_d &= [P_2(r^2 + 2\bar{y}^2) + 2P_1\, \bar{x}\, \bar{y}][1 + P_3 r^2 + \cdots] \end{aligned} \tag{2.41}$$

where

$$P_1 = -J_1 \sin \phi_0, \ P_2 = J_1 \cos \phi_0. \tag{2.42}$$

The terms higher than second order in (2.41) are practically negligible, leading to common forms as

$$\begin{aligned} \Delta x_d &= P_1(r^2 + 2\bar{x}^2) + 2P_2\, \bar{x}\, \bar{y} = P_1(3\bar{x}^2 + \bar{y}^2) + 2P_2\, \bar{x}\, \bar{y} \\ \Delta y_d &= P_2(r^2 + 2\bar{y}^2) + 2P_1\, \bar{x}\, \bar{y} = P_2(\bar{x}^2 + 3\bar{y}^2) + 2P_1\, \bar{x}\, \bar{y} \end{aligned} \tag{2.43}$$

2.4.2 Out-of-plane and in-plane distortion

Out-of-plane distortion

The unflatness of focal plane causes the out-of-plane distortion, denoted by Δr_u. Its components Δx_u and Δy_u in two coordinates are

$$\begin{Bmatrix} \Delta x_u \\ \Delta y_u \end{Bmatrix} = \begin{Bmatrix} \bar{x}/r \\ \bar{y}/r \end{Bmatrix} \sum_{n=0}^{N} \sum_{j=0}^{n} a_{ij} \bar{x}^{\,(n-j)} \bar{y}^{\,j}. \tag{2.44}$$

While Δr_u may be significant in metric film cameras, it is often negligible in digital cameras.

In-plane distortion

In-plane distortion, denoted by Δr_f, arises due to the shrinkage and stretching in film cameras. The shrinkage effect in CCD camera is a differential scaling between the x and y coordinates. In order to avoid overparameterization, Δr_f is often modeled in two coordinates as

$$\Delta x_f = B_1 \bar{x} + B_2 \bar{y}$$
$$\Delta y_f = 0 \tag{2.45}$$

where B_1 and B_2 are named as the affinity and the shear terms, respectively. They account for the differential scaling and the non-orthogonality between two image axes, respectively (It is proved in Appendix C that the shear term B_2 and the skew parameter s in the calibration matrix (1.13) are exactly the same, up to a scale constant). The in-plane distortion is rarely of metric significance in digital cameras.

In summary, the Brown self-calibration model is

$$\Delta x = -\Delta x_0 - \frac{\bar{x}}{f}\Delta f + \bar{x}(K_1 r^2 + K_2 r^4 + K_3 r^6) + P_1(r^2 + 2\bar{x}^2) + 2P_2\,\bar{x}\,\bar{y}$$
$$\Delta y = -\Delta y_0 - \frac{\bar{y}}{f}\Delta f + \bar{y}(K_1 r^2 + K_2 r^4 + K_3 r^6) + P_2(r^2 + 2\bar{y}^2) + 2P_1\,\bar{x}\,\bar{y} \tag{2.46}$$

Adding (2.45) to (2.46) leads to the so-called extended 10-parameter model:

$$\Delta x = -\Delta x_0 - \frac{\bar{x}}{f}\Delta f + \Delta x_r + \Delta x_d + \Delta x_f$$
$$\Delta y = -\Delta y_0 - \frac{\bar{y}}{f}\Delta f + \Delta y_r + \Delta y_d + \Delta y_f \tag{2.47}$$

The Brown and the 10-parameter models are most favorable in close range digital camera calibration. More materials on close range self-calibration models can be found in Brown (1971; 1972), Fraser (1997) and McGlone et al. (2004).

2.4.3 Correlation analysis

Three types of high correlations are of major concerns in close range camera self-calibration:

1. high correlations between the IO and the EO parameters;
2. high correlations between principal point shift and the decentering distortion parameters P_1 and P_2; and
3. high correlation between Δf and the in-plane distortion parameter B_1.

Correlations of the first type can be quite serious in calibrating the cameras of long focal length (Stamatopoulos & Fraser, 2011), while they are rarely significant in most other cases as long as the image configurations are appropriate (Luhmann et al., 2006). The high correlations of the second and the third types are often encountered in practice and will be studied in this subsection. As plumb-line calibration is generally unable to locate the principal point (Clarke & Fryer, 1998; José & Cabrelles, 2007) and the decentering parameters are not used in the calibration of long focal length camera (Stamatopoulos & Fraser, 2011), these two cases are beyond the scope of this study and are not further considered.

It is well known that, the high correlations of the second type indicate that the decentering distortion can be partially compensated by the principal point shift, and vice versa. It was illustrated in Clarke et al. (1998) that the EO parameters were linked to these high correlations. However, there were only four images used in their simulation study (which may be geometrically inadequate) and their conclusion is unlikely to be true. In fact, these high correlations still remain even if the EO parameters are precisely given. The EO parameters should thus not be considered to be the main factor causing the high correlations. There must be other reasons.

It will be shown that the high correlations of the second and third types are inherently caused by the *polynomial nature* of the Brown model and the correlations are exactly those occurring in all the

polynomial models in Section 2.2. For this purpose, the first five terms of the bivariate polynomials, by neglecting the constant terms which are entirely irrelevant to correlation analysis, are rewritten as

$$\Delta x_P : a_1\bar{x} + a_2\bar{y} + a_3\bar{x}^2 + a_4\bar{x}\,\bar{y} + a_5\bar{y}^2$$
$$\Delta y_P : b_1\bar{x} + b_2\bar{y} + b_3\bar{x}^2 + b_4\bar{x}\,\bar{y} + b_5\bar{y}^2 \tag{2.48}$$

which correspond to (2.22). In order to minimize the correlations, b_1, b_2, b_3 and b_5 should be replaced by a_2, $-a_1$, $-a_3$ and $-a_4$, respectively (see Section 2.2 and Section 2.3.1). (2.48) are thus reduced as

$$\Delta x_P : a_1\bar{x} + a_2\bar{y} + a_3\bar{x}^2 + a_4\bar{x}\,\bar{y} + a_5\bar{y}^2$$
$$\Delta y_P : a_2\bar{x} + (-a_1)\bar{y} + b_3\bar{x}^2 + (-a_3)\bar{x}\bar{y} + (-a_4)\bar{y}^2 \,. \tag{2.49}$$

In contrast, the terms are $3P_1\bar{x}^2$ and $2P_1\,\bar{x}\,\bar{y}$, and $3P_2\bar{y}^2$ and $2P_2\,\bar{x}\,\bar{y}$, in the decentering distortion (2.43). They are different from those terms $a_3\bar{x}^2$ and $-a_3\bar{x}\bar{y}$, and $-a_4\bar{y}^2$ and $a_4\bar{x}\bar{y}$, in (2.49) of minimum correlations. These differences, particularly the opposite signs between $-a_3\bar{x}\bar{y}$ and $2P_1\,\bar{x}\,\bar{y}$, and between $-a_4\bar{y}^2$ and $3P_2\bar{y}^2$, give rise to high correlations between the decentering parameters and principal point shift.

To further illustrate the impact of the sign differences, two altered formulae are composed:

$$\Delta x_d = P_1(3\bar{x}^2 + \bar{y}^2)$$
$$\Delta y_d = P_2(\bar{x}^2 + 3\bar{y}^2) \tag{2.50}$$

$$\Delta x_d = P_1(3\bar{x}^2 + \bar{y}^2) - 2P_2\,\bar{x}\,\bar{y}$$
$$\Delta y_d = P_2(\bar{x}^2 + 3\bar{y}^2) - 2P_1\,\bar{x}\,\bar{y} \tag{2.51}$$

where the first formulae (2.50) remove the $\bar{x}\,\bar{y}$ terms from (2.43) and the second ones (2.51) change the signs of the $\bar{x}\,\bar{y}$ terms (Note that these formulae are constructed for correlation analyses only, but not for calibration purpose). It is theoretically expected that (2.50) obtain lower correlations than (2.43), and (2.51) which most resemble (2.49) get lowest correlations. This will be confirmed by the tests in Chapter 3. Thus, high correlations between the decentering distortion parameters and principal point shift are inherent in the Brown models, mainly due to that the polynomial representation of the decentering distortion (2.43) does not follow (2.49) or (2.23) to minimize correlations.

Analogously following the spirit of (2.49), the in-plane distortion should be altered as

$$\Delta x_f = B_1\bar{x} + B_2\bar{y}$$
$$\Delta y_f = -B_1\bar{y} \quad . \tag{2.52}$$

While handling the scaling effect quite similarly with (2.45), (2.52) possess an advantage that they reduce the correlation between B_1 and Δf without any price of overparameterization. This advantage can be interpreted by the geometric effects of Δf, (2.45) and (2.50), as illustrated in Fig. 2.3. It is clearly found in Fig. 2.3 that, compared to (2.45), the geometric effect of (2.52) is more distinct from that of Δf. This leads to smaller correlation between Δf and the B_1 in (2.52).

It is noteworthy that, although certain terms are common and their numerical behaviors are similar in the Brown or 10-parameter model and the polynomial self-calibration model in Section 2.2, those terms should not be confounded and they are factually different in many ways. The terms in the Brown model are based on the distortion sources and they are physically interpretable; while the terms in the polynomial model are derived from the abstract principle of function approximation, and they are independent of distortion sources and not interpretable.
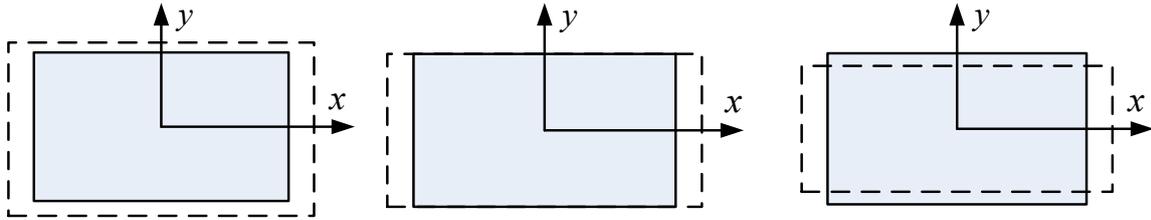
Fig. 2.3 Geometric effects of $\Delta f < 0$ (left), the affinity parameter $B_1 > 0$ in (2.45) (middle) and in (2.52) (right).

2.5 Concluding remarks

It is pointed out that the primary mathematical principle of photogrammetric self-calibration (building self-calibration models) is function approximation. The significance of this principle identified not only in building two groups of mathematical self-calibration models, i.e., the Legendre and the Fourier models, but also in refining the physical self-calibration models in close range photogrammetry.

The work in this chapter will be tested in practice, with particular interests in

- how is the practical performance of the Legendre and the Fourier self-calibration models?
- what are the advantages and disadvantages of these two new models, compared to the conventional counterparts?
- experimenting the correlation analyses of the Brown and the 10-parameter model in close range camera calibration; and
- others of practical interests.

3 Self-Calibration Models in Photogrammetry: Tests

"I have no satisfaction in formulas unless I feel their numerical magnitude."

—— Lord Kelvin (William Thomson) (1824 – 1907).

3.1 Test datasets

3.1.1 Datasets in aerial photogrammetry

The empirical test datasets are taken from a recent project of DGPF (German Society for Photogrammetry, Remote Sensing and Geoinformation). This project was carried out in the well-established Vaihingen/Enz test field nearby Stuttgart, Germany. This successful project aimed at an independent and comprehensive evaluation on the performance of digital airborne cameras, as well as providing a standard empirical dataset for the next years (Cramer, 2010; DGPF project, 2010).

Four flight datasets of two cameras are adopted in our tests: DMC (GSD 20cm, ground sample distance), DMC (GSD 8cm), UltraCamX (GSD 20cm) and UltraCamX (GSD 8cm). Each camera was flown at two heights, i.e., a same DMC camera flown in the blocks of DMC (GSD 20cm) and DMC (GSD 8cm), and a same UltraCamX camera flown in the UltraCamX (GSD 20cm) and UltraCamX (GSD 8cm) blocks. The test field of a top view is illustrated in Fig. 3.1.The area of solid rectangular in Fig. 3.1 is used for the flights of GSD 20cm, and the smaller area of dash rectangular is for the flights of GSD 8cm.

Fig. 3.1 The Vaihingen/Enz test field nearby Stuttgart, Germany.

Table 3.1 The block configurations of the test flights of airborne cameras.

| Scenarios	In-situ calibration	Operational project
Sensor orientation	Integrated sensor orientation	Integrated sensor orientation
Forward overlap (p)	60% ~70%	60% ~70%
Cross strip	NO	NO
Side overlap (q)	60% ~70%	20% ~30%
Image number		
DMC (GSD 20cm)	3 lines × 14/line = 42	2 lines × 14/line = 28
UltraCamX (GSD 20cm)	3 lines × 12/line = 36	2 lines × 12/line = 24
DMC (GSD 8cm)	5 lines × 22/line = 110	3 lines × 22/line = 66
UltraCamX (GSD 8cm)	5 lines × 35/line = 175	3 lines × 35/line = 105
GCP/ChP distribution		
DMC (GSD 20cm)	47 GCPs / 138 ChPs	4 GCPs / 181 ChPs
UltraCamX (GSD 20cm)	47 GCPs / 138 ChPs	4 GCPs / 181 ChPs
DMC (GSD 8cm)	49 GCPs / 69 ChPs	4 GCPs / 114 ChPs
UltraCamX (GSD 8cm)	48 GCPs / 68 ChPs	4 GCPs / 112 ChPs
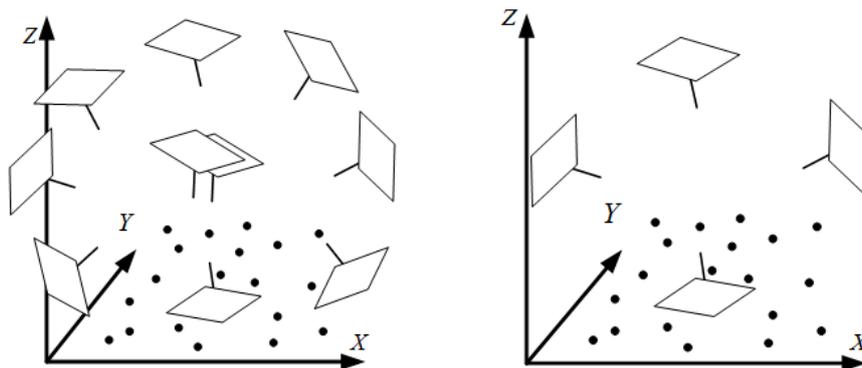
Fig. 3.2 The 10-image (left) and 4-image (right) configurations in close range photogrammetry.
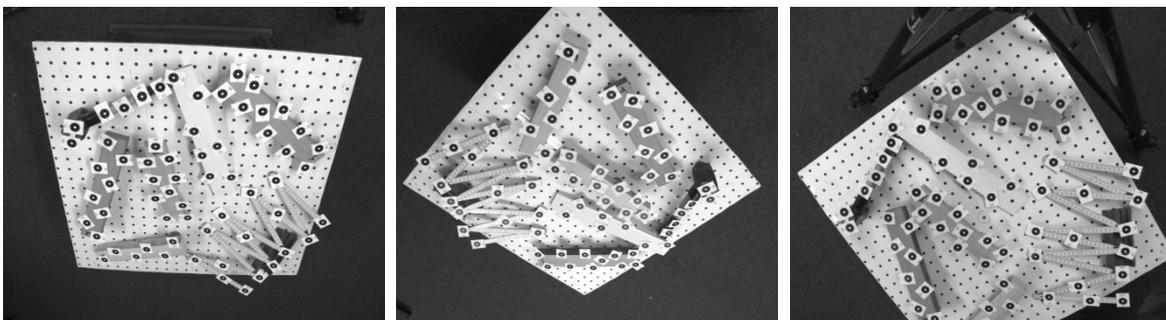

Fig. 3.3 Three examples of the practical images taken by a typical close range digital camera.

For each flight, we are interested in two most often used scenarios: in-situ calibration and operational project. The former scenario is with high side overlapping ($\approx 60\%$) and a number of well-distributed GCPs, and the latter with low side overlapping ($\approx 20\%$) and 4 GCPs only at the block corners. The block configurations are depicted in Table 3.1, where 'ChP' stand for check point. The external accuracy, also called "empirical check point accuracy", indicates the root mean square errors (RMSE) of check points.

Other datasets, which are acquired from different test fields by using different cameras, are also adopted to test the new self-calibration models. The cameras being tested include DMC II, UltraCamXp, DigiCAM and so on. Similar results are obtained as those in the DGPF project. The details on these tests are not demonstrated in this thesis due to contract limitations.

The bundle adjustment with self-calibration is implemented in the open-source software DGAP from the Institute for Photogrammetry (ifp), University of Stuttgart, Germany (http://www.ifp.uni-stuttgart.de/publications/software/openbundle/index.html, last accessed in May 2012). DGAP, composed by Dipl. -Ing Dirk Stallmann, is a compact, efficient and reliable software. It delivers adjustment results similar to those by commercial software, such as ApplicationsMaster from Inpho/Trimble (http://www.inpho.de) and PAT-B from the K^2 – Photogrammetry company (http://www.k2-photogrammetry.de).

It should be pointed out that all the tests are not intended for, and should not be interpreted as, the direct comparisons between different commercial camera systems. All the investigations are carried out for the scientific purpose only.

3.1.2 Datasets in close range photogrammetry

Simulation datasets

The focal length of the virtual lens is 8mm and the image format is $7{\times}7\text{mm}^2$. The pixel size is $4{\times}4\mu m^2$ and the standard deviation (std. dev.) of the Gaussian noise in the image measurements is 0.1 pixels.

Two groups of simulation datasets are used. They contain ten and four images, respectively, as demonstrated in Fig. 3.2. In the 10-image configuration, there are two images looking-down and eight around a 3D test field with a convergent angle of approximately 45^0. This highly redundant and reliable configuration follows the suggestions by Wester-Ebbinghaus (1983). The 4-image configuration is similar to that used in Clark et al. (1998), with a convergent angle of about 90^0.

Empirical datasets

Two lens systems, with focal length of 8mm and 12mm, are fixed in a uEye camera from Imaging Development System (IDS) GmbH (http://www.ids-imaging.com). The resolution of the CCD sensor is 2448×2048 and the pixel size is $3.5{\times}3.5 \ \mu m^2$. The image distribution is similar to the 10-image configuration in Fig. 3.2 (left). Ten images of each lens system are taken from a 3D test field, and a few examples are illustrated in Fig. 3.3.

3.2 In-situ airborne camera calibration

Before proceeding to the empirical tests, we need to study two topics of in-situ airborne camera calibration: overall system calibration and the evaluation strategy. The first topic is an essential requirement for calibrating heterogeneous systematic errors of a camera system. The second one, on which there has been a lack of investigations, is vital to evaluate whether a camera system has been fully in-situ calibrated and to assess the performance of self-calibration models.

3.2.1 Overall system calibration

The systematic errors involved in the direct EO observations must be compensated. The errors of important interests include the misalignments between camera and navigation instruments and the shift/drift (if present). For the overall system calibration, a major challenge is to minimize the coupling effects of different correction parameters. Decoupling is critical in the sense that each systematic error must be independently and properly corrected and the calibration results are block-independent.

For this purpose, we suggest the joint application of the Legendre APs or the Fourier APs (for calibrating image distortion) with other correction parameters, i.e., the three IO parameters used for correcting principal point shift and focal length error, the GPS/IMU shift/drift and the misalignment correction parameters. Low correlations must be warranted between the self-calibration APs and those other correction parameters, and between APs and the EO parameters.

3.2.2 Evaluation strategies

In the traditional aerial triangulation without aerial control, the common evaluation approach was to check whether the empirical check-point accuracy is close to the optimal theoretical accuracy. This evaluation approach, which is still important yet, may be inadequate in integrated sensor orientation due to two reasons. First, according to the statistical effect of sampling size, a sufficient number of well-distributed check points are needed to properly evaluate the empirical accuracy. This is however not always satisfied in practice due to the economic or other limitations. Second, high correlations may occur between correction parameters and they can result in miscalibration.

In this subsection, the evaluation strategies of in-situ camera calibration are investigated via a simulation study. The simulated camera, embodied with assumed GPS/IMU system, is similar to the DMC camera. The error of $20\mu m$ is introduced into the three IO parameters. The image distortion is represented by the Legendre model of third order (factually any model can be used as well to represent certain distortion, as long as the model's APs don't have high correlations with other parameters). The IMU misalignments in three directions are 0.005 degrees. Two block configurations, 'calibration scenario' and 'operational scenario', are similar to those of DMC (GSD 20cm) in Table 3.1.

In practice, the true precision of GPS/IMU measurements is unknown[6] and its standard deviation (std. dev.) is often assigned empirically. It may lead to variance misspecifications, whose effect on calibration is also investigated here. Without loss of generality, four presumptions of the std. dev. of the GPS/INS position, 20, 10, 5 and 2 (unit: cm) in the three dimensions, are employed, while the true value is 10cm. The std. dev. of the precision of the other observations is assigned perfectly.

Two adjustment solutions are performed on the simulated blocks. In the first solution, the three IO and the IMU misalignment parameters are employed, while the Legendre APs of third order are applied additionally in the second solution. The impact of the remaining distortion can be demonstrated by comparing the two adjustment results. Note that the first adjustment solution implies equivalently that uncompensated distortion is remained if an inappropriate self-calibration model has been adopted.

The adjustment results of the three IO parameters and the IMU misalignments in the 'calibration scenario' are illustrated in Fig. 3.4 and Fig. 3.5, respectively. On the one hand, it is found from the left figures of Fig. 3.4 and Fig. 3.5, that the three IO parameters and the IMU misalignments cannot be correctly calibrated if significant distortion is remained. Moreover, the calibration results vary substantially with the std. dev presumptions of GPS/INS position. On the other hand, if the proper self-calibration APs are employed in adjustment, the systematic errors can be precisely calibrated (the right figures). More interestingly, the calibration is quite stable, disregarding the variations of the std. dev. presumptions of GPS/INS position. Thus, a main observable distinction between using

---

[6] The precision of GPS/IMU measurements depends on signals received and algorithmic processing.

inappropriate and appropriate self-calibration models lies in whether the calibration of systematic errors varies with the std. dev. presumptions of GPS/INS position.

In the 'operational scenario', it is nearly impossible to obtain accurate calibration results even if the adjustment model is perfect (i.e., adjustment with exact correction parameters, self-calibration model, and perfect variance assignments). The estimates of the three IO parameters with perfect adjustment model are 21.7, 30.9 and 12.1 (μm), which quite deviate from the true values $20\mu m$. This is mainly due to the weak block geometry. A sufficient number of GCPs are necessary for in-situ airborne camera calibration.

According to the above simulation studies, the following three strategies are suggested for evaluating full in-situ airborne camera calibration:

1. the empirical check point accuracy should be equal to the theoretical accuracy. The statistical effect of sampling size (the number and the distribution of check points) should be kept in mind in practice;
2. the calibration results of systematic errors should be very stable, with respect to varying the std. dev. presumptions of GPS/INS positions; and
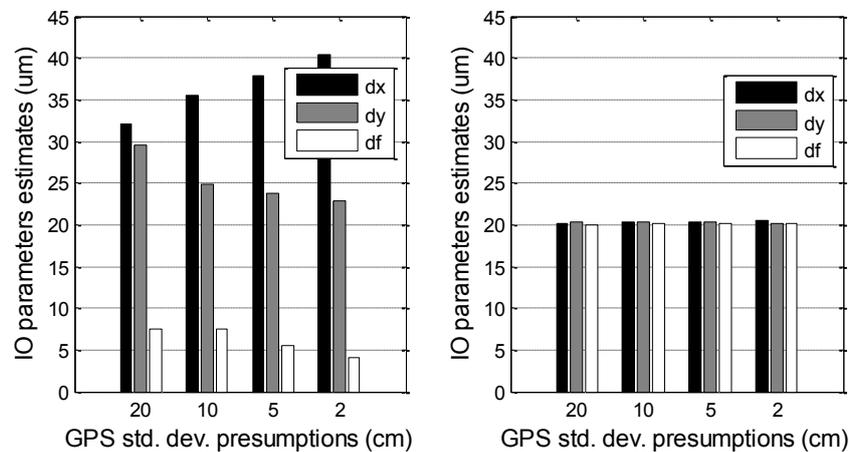

Fig. 3.4 The calibration results of the three IO parameters vary with different std. dev. presumptions of GPS/INS position, without (left) and with (right) appropriate distortion calibration.
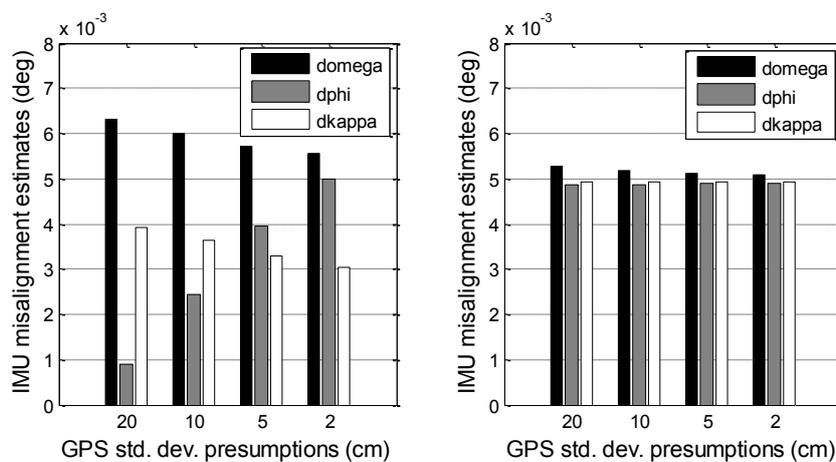

Fig. 3.5 The calibration results of the IMU misalignments vary with different std. dev. presumptions of GPS/INS position, without (left) and with (right) appropriate distortion calibration.

3. the correction of each systematic error should be decoupled from others' correction. Any correction parameter should be low correlated with others.

Nevertheless, it cannot take all practical effects into account in the simulation study. For example, the instability of camera lens, imperfect forward move compensation (FMC) or time delayed integration (TDI), and operator errors, may occur in practice. Thus, these three strategies may be not entirely satisfied in every practice.

These three strategies will be used to evaluate the performance of the Legendre and the Fourier self-calibration models. Another similar simulation study with more details was given in Tang et al. (2012).

3.3 Tests in aerial photogrammetry

3.3.1 Tests on Legendre self-calibration model

In-situ calibration scenario

The system calibration strategy in Section 3.2.1 is adopted in all the blocks of in-situ calibration scenarios. Particularly, the three IO, IMU misalignments and horizontal GPS shift (insignificant in all the tests) parameters, and the Legendre self-calibration model of $M = N = 5$, are employed. The order of the Legendre model is empirically selected by the compromise between achieving optimal accuracy and reducing overparameterization effects. The derived external accuracy, indicated by "self calibrating", is compared to the theoretical accuracy and the "without APs" one which indicates using the three IO parameters but not the Legendre self-calibration APs. We assume four std. dev. of the GPS/INS positions: 20, 10, 5 and 2 (unit: cm) in the three dimensions. The std. dev. assumptions of the other observations are kept invariant.

The adjustment accuracy is demonstrated in Fig. 3.6 (the APs of statistical insignificance are not eliminated in the adjustment unless specified). By comparing "self calibrating" with "Without APs", the refinement of the Legendre APs is significant in all the blocks, up to 10cm in the DMC (GSD 20cm) block. Moreover, all the "self calibrating" accuracy reaches very close to the theoretical one, i.e., the optimal accuracy has been achieved. All the "self calibrating" accuracy reaches to about 0.2 GSD in the horizontal directions and 0.4 GSD in the vertical direction. It is interesting to note that, although the DMC and UltraCamX cameras are differently manufactured, very similar external accuracy can be obtained by using the Legendre APs in the blocks of similar configuration, i.e., similar GSD, similar GCPs distribution, and similar forward and side overlapping levels. This important fact coincides well with the photogrammetric accuracy expectation. That is, if all the systematic errors have been fully calibrated, the external accuracy should depend only on the block configuration and the precision of measurements, but is independent of the cameras being used.

For the system calibration, we demonstrate in Fig. 3.7 and Fig. 3.8 the calibration results of the three IO parameters and the IMU misalignments in the four blocks, with respect to different std. dev. assumptions of GPS/INS positions. It is observed that the calibrations of the three IO parameters and the IMU misalignments are quite stable. These results meet well the conclusions of the simulation study in Section 3.2.2. It is noticed as well that the dx calibration is less stable than dy and dc, particularly in the DMC (GSD 8cm) block. It may be caused by the imperfect TDI (or FMC) in practice, since the x coordinate is parallel to the flight direction in all the blocks. This practical effect was not accounted in the simulation study in Section 3.2.2. Further, by comparing the calibration results of the DMC and UltraCamX cameras at different flight heights, it can be found that the three IO parameters of the both cameras are very stable at different heights.

Another issue of interest is the precision of image measurements. The posteriori std. dev. estimates are 1.6, 1.4, 0.89 and 0.78 (μm) in the DMC (GSD 20cm, GSD 8cm) and UltraCamX (GSD 20cm, GSD 8cm) blocks, respectively. These values are around 0.12 pixel which are 12 and 7.2 (μm) for the DMC

and UltraCamX cameras, respectively. These values meet very well the expected precision of the automatic tie point transfer techniques in CCD-array aerial images.

Fig. 3.6 External accuracy in the four blocks of in-situ calibration scenarios ('without APs' indicates using the three IO parameters but not the Legendre APs).

Fig. 3.7 The calibration results of the three IO parameters in the four blocks of in-situ calibration scenarios, with respect to various std. dev. preassumptions of GPS/INS positions (by using the Legendre APs).

Fig. 3.8 The calibration results of the IMU misalignments in the four blocks of in-situ calibration scenarios, with respect to various std. dev. preassumptions of GPS/INS positions (by using the Legendre APs).
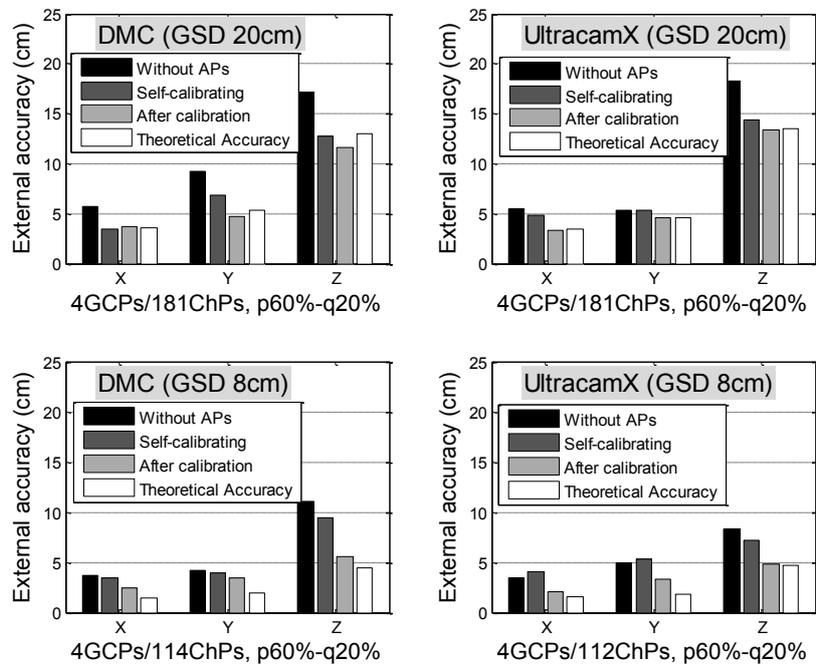
Fig. 3.9 External accuracy in the four blocks of operational project scenarios ('without APs' indicates using the three IO parameters but not the Legendre APs).

Operational project scenario

There are 4 GCPs and 20% side overlapping level in the blocks of the operational project scenario. The IMU misalignments and the three IO parameters, and the Legendre model of $M = 4$, $N = 3$ are employed in the adjustment. This derived external accuracy is indicated as "self calibrating". Due to 4 GCPs available only, the GPS/IMU observations must be weighted carefully to achieve the best accuracy.

The quality of the in-situ calibration is evaluated as well in the blocks of operational scenarios. The in-situ calibration results of the three IO parameters and image distortion are fixed as known values in the corresponding "reduced" operational scenario, i.e., it assumes that the camera has been fully calibrated. Self-calibration is not needed, while the IMU misalignment parameters are still free unknowns (the IMU parameters can be fixed as well). The derived external accuracy is called "after calibration" which is compared to "self calibrating", "without APs" and theoretical ones.

The external accuracy in all the four blocks is illustrated in Fig. 3.9. From those results, the 'self-calibrating' by using the Legendre APs improves the accuracy and the "after calibration" yields further refinement. The "after calibration" accuracy is very close to the optimal theoretical one in every block. Therefore, these tests not only recognize the sufficient accuracy obtained by the Legendre APs in the blocks of operational scenarios, but confirm the good efficiency of the Legendre APs in the in-situ calibration.

3.3.2 Tests on Fourier self-calibration model

The empirical tests on the Fourier self-calibration model are performed parallel to those on the Legendre models in the last subsection. The Fourier models of first order are used in all the tests. The results are illustrated in Fig. 3. 10 – Fig. 3.13, parallel to Fig. 3.6 – Fig. 3.9.

Generally, the Fourier model obtains results (accuracy and system calibration) very similar to the Legendre model, while the former needs much fewer unknown APs (16 unknowns) than the latter (66 or 34 unknowns). The details on these tests are not repeated.
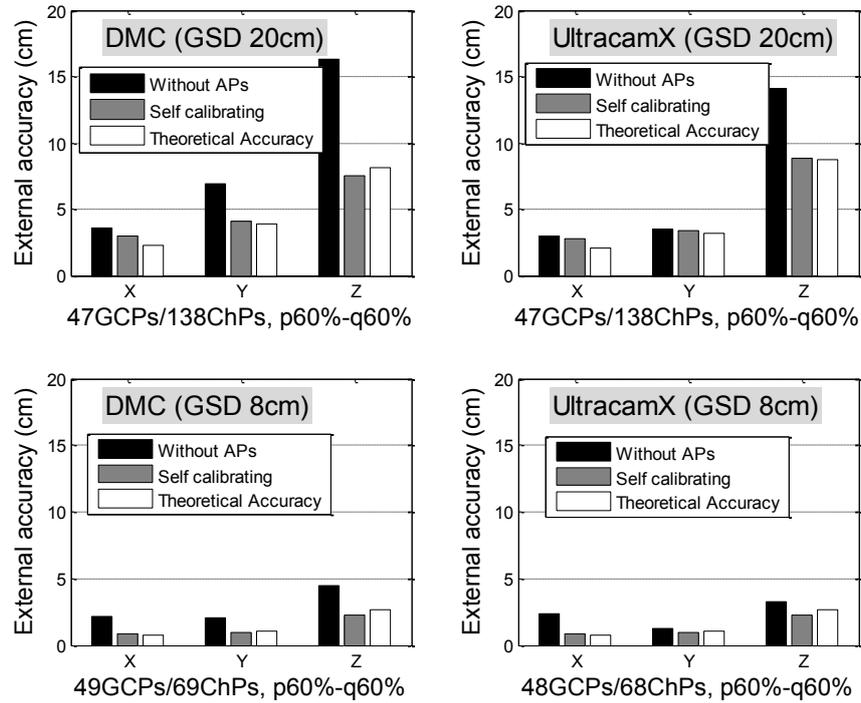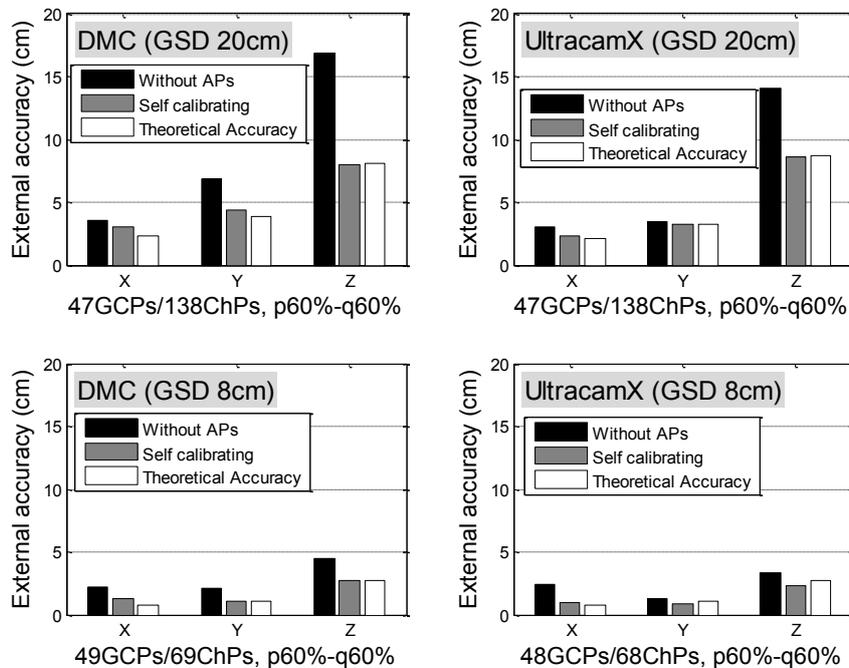

Fig. 3. 10 External accuracy in the four blocks of in-situ calibration scenarios ('without APs' indicates using the three IO parameters but not the Fourier APs).
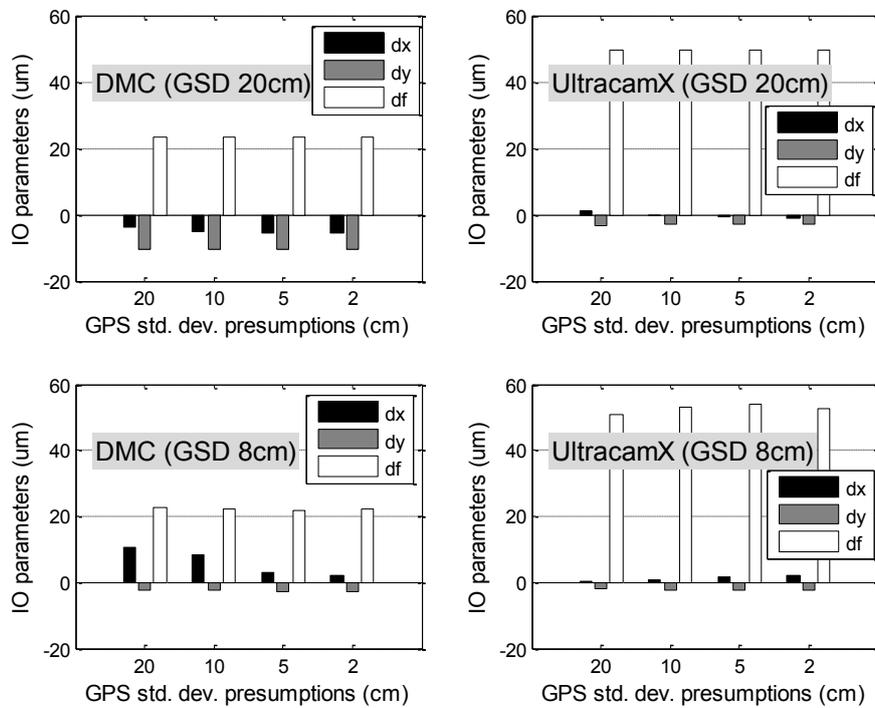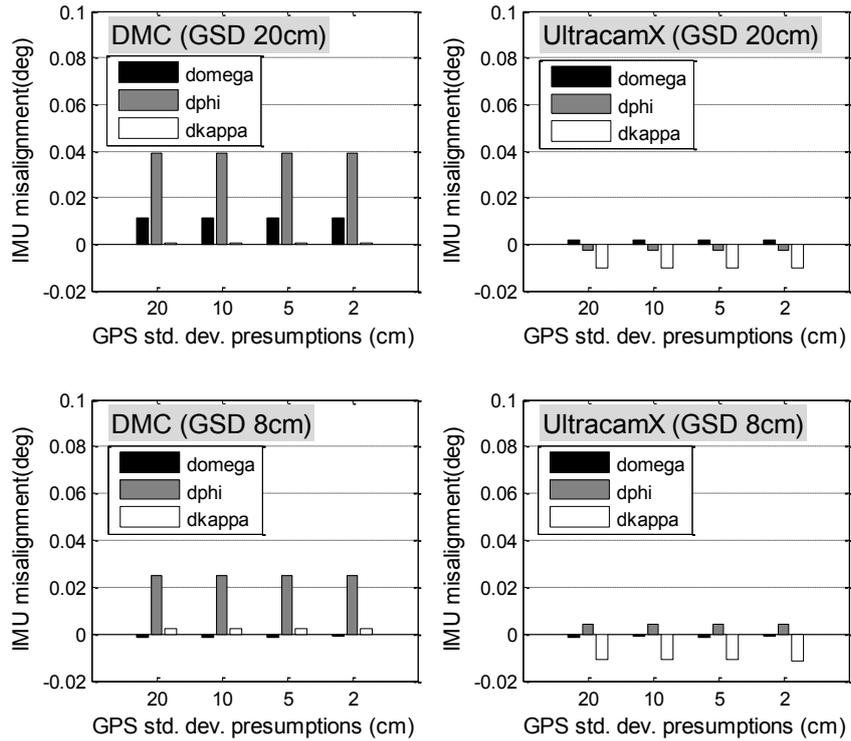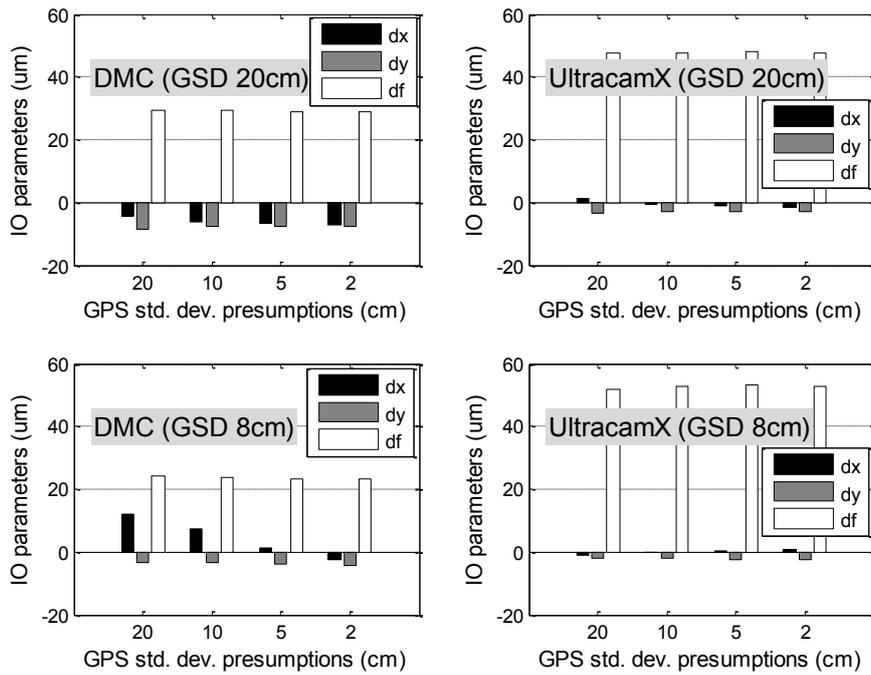
Fig. 3.11 The calibration results of the three IO parameters in the four blocks of in-situ calibration scenarios, with respect to various std. dev. preassumptions of GPS/INS positions (by using the Fourier APs).
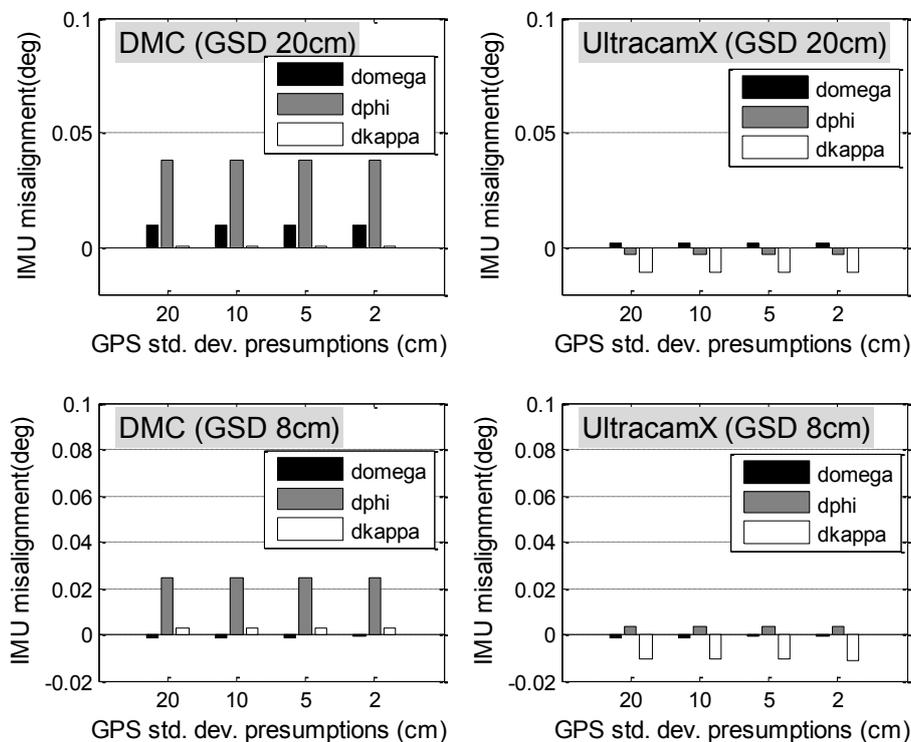
Fig. 3.12 The calibration results of the IMU misalignments in the four blocks of in-situ calibration scenarios, with respect to various std. dev. preassumptions of GPS/INS positions (by using the Fourier APs).
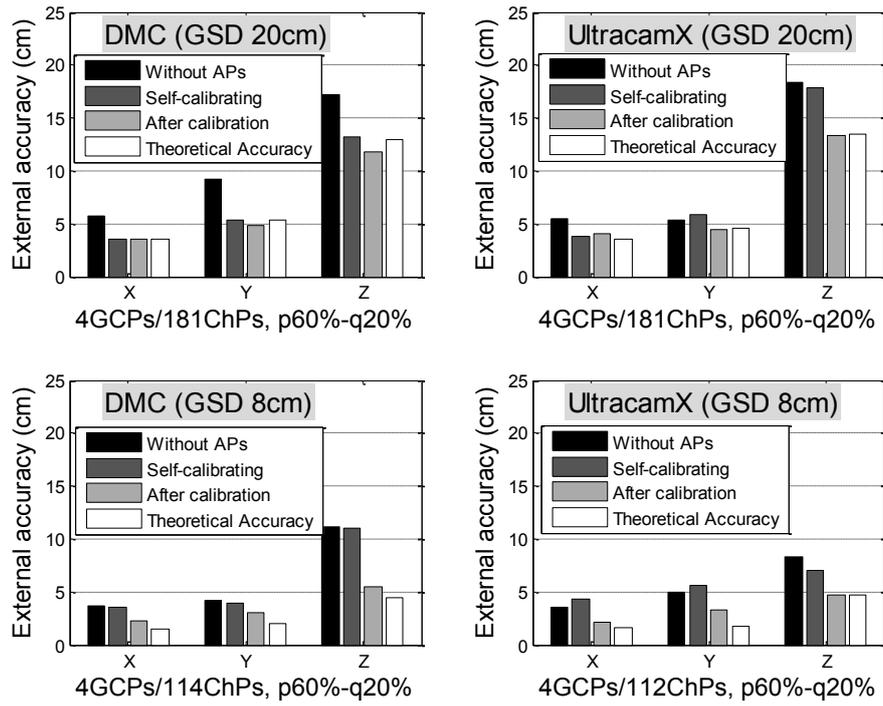
Fig. 3.13 External accuracy in the four blocks of operational project scenarios ('without APs' indicates using the three IO parameters but not the Fourier APs).
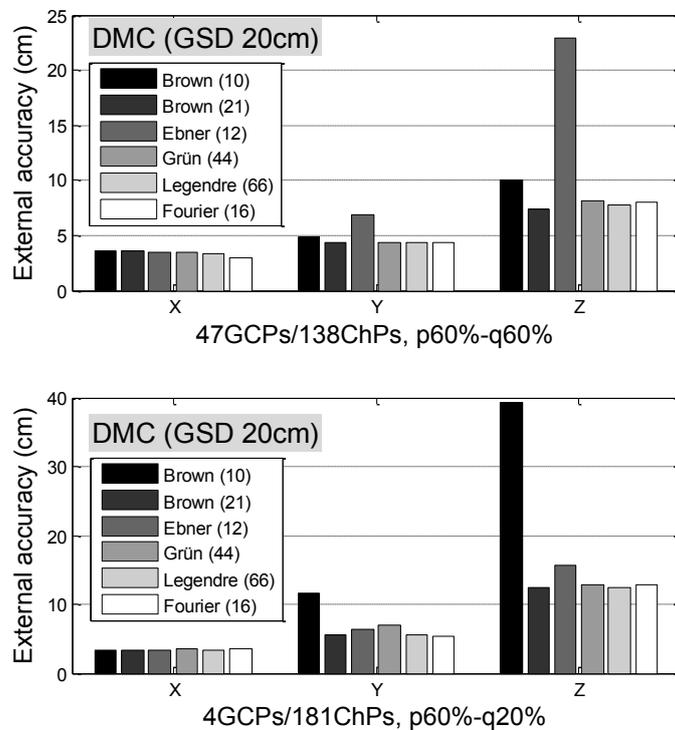
Fig. 3.14 Accuracy comparisons of different self-calibration models in the 'DMC (GSD 20cm)' block of two scenarios: the in-situ calibration (top) and the operational project (bottom).
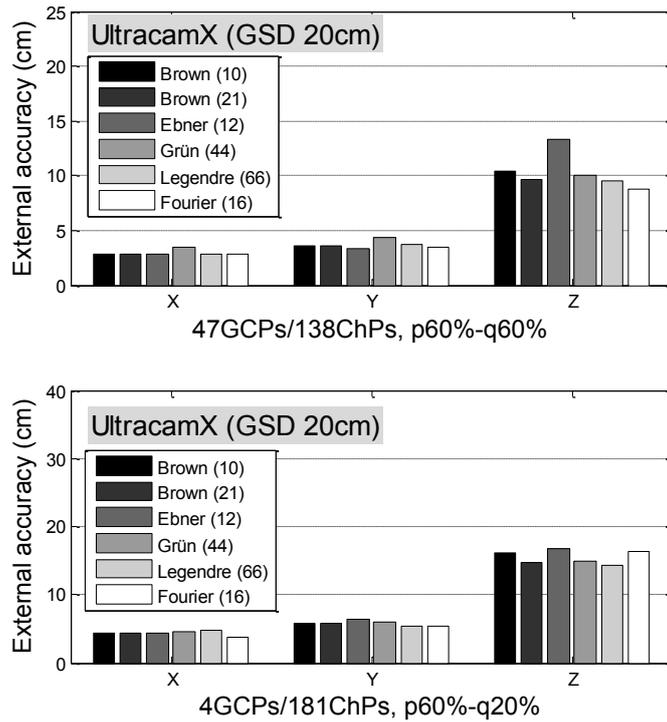
Fig. 3.15 Accuracy comparisons of different self-calibration models in the 'UltraCamX (GSD 20cm)' block of two scenarios: the in-situ calibration (top) and the operational project (bottom).
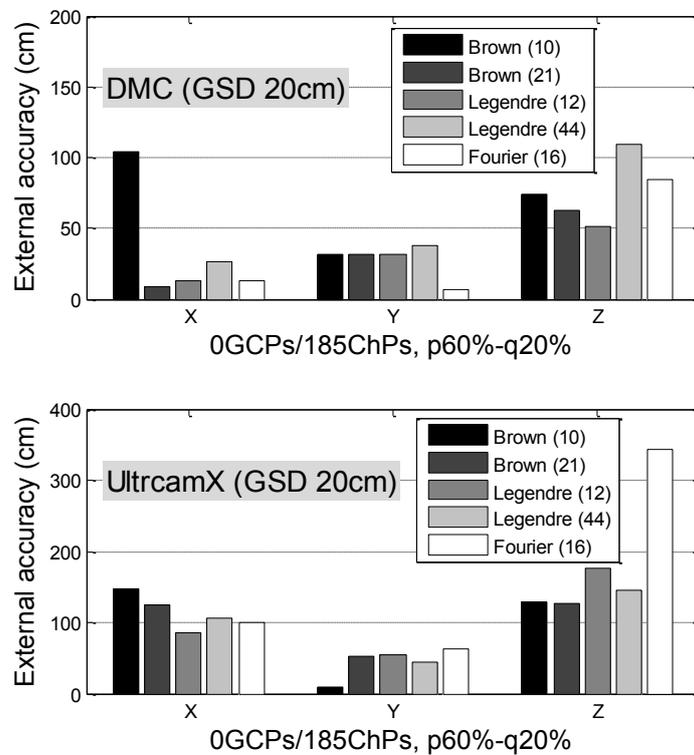
Fig. 3.16 Accuracy comparisons of different self-calibration models in the 'DMC (GSD 20cm)' (top) and 'UltraCamX (GSD 20cm)' (bottom) blocks, with zero GCP and 20% side-overlapping levels.

3.4 Comparisons: airborne camera calibration

In this section, comparisons are made among different self-calibration models in airborne camera calibration, with respect to external accuracy, correlation analyses and system calibration. The self-calibration models taken into account include the 10-parameter physical model (Brown, 1971; Fraser, 1997), the extended Brown model (Brown, 1976), the models by Ebner (1976), the models by Grün (1978), the Legendre and the Fourier models. They are denoted respectively by "Brown (10)", "Brown (21)", "Ebner (12)", "Grün (44)", "Legendre (n)" and "Fourier (n)", where the figure in parentheses indicates the number of the unknown APs and 'n' implies the number of the Legendre and the Fourier APs depending on the chosen degrees. The comparisons are performed fairly in same block configurations (same GCP and ChP distribution and same overlapping levels) and with the same adjustment strategies (same weights on measurements and correction parameters).

3.4.1 External accuracy

We compare the external accuracy in the 'DMC (GSD 20cm)' and the 'UltraCamX (GSD 20cm)' blocks of the in-situ and the operational scenarios. The results are illustrated in Fig. 3.14 and Fig. 3.15 (noting the different scales in vertical axes in the figures).

In the 'DMC (GSD 20cm)' block, it is obvious that "Ebner (12)" and "Brown (10)" obtain rather worse accuracy than the others. Yet, the reasons are quite different for their worse performance. On the one hand, "Ebner (12)" performs poorly because the algebraic polynomial of second order is insufficient to calibrate the image distortion. Polynomials of higher degree are required for better approximation, according to the approximation principle. The considerable improvement is clearly achieved by using the Grün models of fourth order and the Legendre APs of fifth order. On the other hand, "Brown (10)" fails mainly due to the fact that the classical close range self-calibration model is inappropriate for calibrating these airborne cameras. The distortion of aerial images (especially after lab calibration) is not dominated by the radial distortion which is the main one in close range cameras. As the distortion plotted in Fig. 3.19 and Fig. 3.20 below, there is no significant radial tendency in the distortion of both the DMC and the UltraCamX cameras. The good performance of the "Brown (21)" model is due to that this model includes several high order polynomial terms which although were supposed compensate film deformation and unflatness (Brown, 1976). All these self-calibration models perform more closely in the 'UltraCamX (GSD 20cm)' block, because the distortion of the UltraCamX camera is quite small (see Table 3.4 below). From these results it is seen that the "Brown (21)", "Legendre (66)" and "Fourier (16)" obtain similarly the best accuracies in these blocks.

It is noticed that the Fourier model (16 APs) obtain similar accuracy as the Legendre model (66 APs), but use much fewer APs. Fewer APs imply better efficiency. Mathematically, fewer APs indicate that the distortion function can be faster approximated by the Fourier series than the polynomials. Fewer APs help to improve the stability of the block geometry against overparameterization. This is a practical advantage of the Fourier model over the polynomial model.

The models of "Brown (10)", "Brown (21)", "Legendre (12)", "Legendre (44)" and "Fourier (16)" are further compared in the two blocks with zero GCP and 20% side overlapping ("Legendre (12)" and "Legendre (44)" perform similarly (or slightly better) to "Ebner (12)" and "Grün (44)", respectively). The accuracy results in these very weak blocks are illustrated in Fig. 3.16. In the 'DMC (GSD 20cm)' block, the "Legendre (12)" obtains the best accuracy in the vertical direction, while "Fourier (16)" gets best in horizontal accuracy. In the 'UltraCamX (GSD 20cm)' block, the "Brown (21)", "Legendre (12)" and "Legendre (44)" obtain quite similar accuracy in all three dimensions. "Fourier (16)" performs much worse in the vertical direction, close to 350cm.

The results in Fig. 3.16 demonstrate that there is no self-calibration model which can certainly outperform others in these very weak blocks without GCP. This is mainly due to that the accuracy in a block without GCPs depends quite heavily on the precision of GPS/IMU observations and the role of self-calibration models may become less significant. Further, the accuracies are about 20–100cm in

the horizon and 50–200cm in the vertical in the blocks without GCP (Fig. 3.16), while they are about 5cm in horizon and 10–15cm in vertical in the blocks with 4 GCPs (Fig. 3.14 (bottom) and Fig. 3.15 (bottom)). 4 GCPs can improve accuracy even more than ten times. The significance of GCPs is clearly shown in these tests. It is thus strongly recommended that GCPs should be introduced into the photogrammetric mapping, even though GPS/IMU system may be able to acquire quite precise observations of the EO parameters. Even a small number of GCPs at the corners of the block can substantially improve the accuracy.

3.4.2 Correlation analyses

Correlation analyses deserve more importance in integrated senor orientation than aerial triangulation, since the heterogeneous observations from multiple sensors may contain various systematic errors. Each systematic error should be calibrated independently from others. The coupling effects should be minimized and low correlations should be guaranteed among different correction parameters.

We examine the correlations between the self-calibration APs and EO parameters, the three IO parameters and the IMU misalignment parameters. Table 3.2 and Table 3.3 depict two typical examples in the DMC (GSD 20cm) and UltraCamX (GSD 20cm) blocks of in-situ calibration scenarios. 'Intra-corr' indicates the intra-correlations of self-calibration APs. '< 0.1' denotes the percentage of correlations smaller than 0.1 and 'max' is the maximum correlation. As "Brown (10)" and "Ebner (12)" deliver rather poor external accuracy (Fig. 3.14 and Fig. 3.15), their performance in correlations is not illustrated here.

Table 3.2 Correlation analyses in the DMC (GSD 20cm) block of an in-situ calibration scenario.

APs	corr.	EO	IO	IMU	Intra-corr
Brown APs (21)	< 0.1	98%	78%	86%	78%
	max	0.19	0.87	0.55	0.92
Grün APs (44)	< 0.1	100%	80%	83%	88%
	max	---	0.73	0.53	0.93
Legendre APs (66)	< 0.1	100%	97%	100%	96%
	max	---	0.44	---	0.57
Fourier APs (16)	< 0.1	100%	89%	92%	92%
	max	---	0.45	0.20	0.53

Table 3.3 Correlation analyses in the UltraCamX (GSD 20cm) block of an in-situ calibration scenario.

APs	corr.	EO	IO	IMU	Intra-corr
Brown APs (21)	< 0.1	99%	72%	85%	75%
	max	0.15	0.60	0.29	0.95
Grün APs (44)	< 0.1	100%	81%	87%	78%
	max	---	0.52	0.23	0.87
Legendre APs (66)	< 0.1	100%	95%	98%	90%
	max	---	0.39	0.11	0.65
Fourier APs (16)	< 0.1	100%	88%	94%	94%
	max	---	0.34	0.16	0.53

Interesting observations can be obtained from Table 3.2 and Table 3.3. First, all the four groups of APs hold very low correlations with the EO parameters; this is nearly certain since EO is independently observed by navigation systems. Second, the Legendre and the Fourier APs, rather than "Brown (21)" and "Grün (44)", deliver much lower correlations with the three IO and the IMU misalignment parameters. For the columns "IO" and "IMU" in Table 3.2 , although the Fourier APs (89% and 92%) seem slightly worse in '< 0.1' than the Legendre APs (97% and 100%, respectively), these differences are negligible because of the similar 'max' correlations, which are 0.45 and 0.20 for the Fourier APs, and 0.44 and <0.1 respectively for the Legendre APs. This occurs similarly in the UltraCamX (GSD 20cm) block, as depicted in Table 3.3. Third, the 'Intra-corr' shows the orthogonality of the Legendre and the Fourier APs. The intra-orthogonality, though having not much impact on calibration and accuracy, helps the stability of the adjustment process.

The Legendre model outperforms the Grün model in correlation analyses in both Table 3.2 and Table 3.3. This confirms the theoretical conclusions in Section 2.2.3 that the Legendre model should be preferred to other polynomial models.

The Legendre and the Fourier models perform similarly best in correlation analyses. Therefore, they minimize the coupling effects and can derive more reliable calibration results than others.

3.4.3 Calibrations of three IO parameters and IMU misalignments

The calibration results of the three IO parameters and the IMU misalignments are examined in the two blocks of in-situ calibration scenarios: DMC (GSD 20cm) and UltraCamX (GSD 20cm); they are illustrated in Fig. 3.17 and Fig. 3.18, respectively. The "Brown (21)", "Legendre (66)" and "Fourier (16)" models are taken into account.

It is observed in Fig. 3.17 that the Legendre and the Fourier models obtain quite coincident results of the three IO parameters, while the "Brown (21)" model gets diverse results, particularly in the focal length calibration in the DMC (GSD 20cm) block. It is found in Fig. 3.18 that the three sets of APs yield similar calibrations of the IMU misalignments, while the results obtained by the Legendre and the Fourier APs are closer. It is reasonable and expectable that the Legendre and the Fourier APs obtain coincident calibration results, since both calibrate effectively the image distortion and have low correlations with the three IO and the IMU misalignment parameters. The high correlations between the "Brown (21)" APs and the three IO parameters (Table 3.2 and Table 3.3) are probably the reason causing the biases in the IO calibration results. As it has lower correlation with the IMU misalignment parameters, "Brown (21)" obtains more consistent results with "Legendre (66)" and "Fourier (16)".
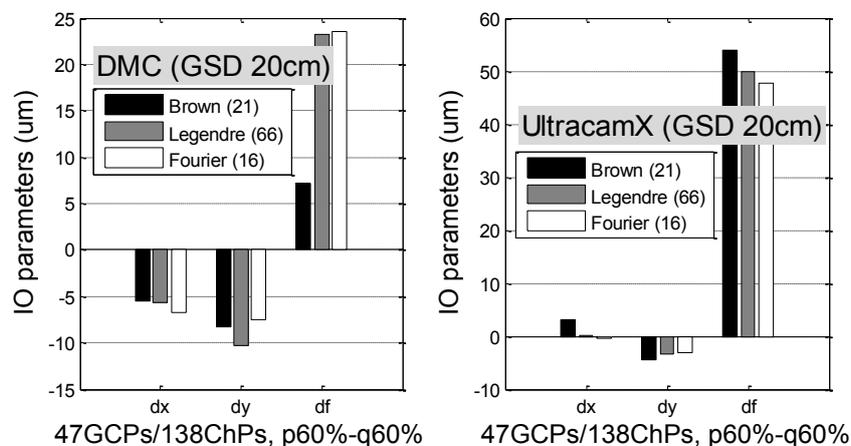

Fig. 3.17 The calibration results of the three IO parameters in the 'DMC (GSD 20cm)' (left) and 'UltraCamX (GSD 20cm)' (right) blocks of in-situ calibration scenarios.
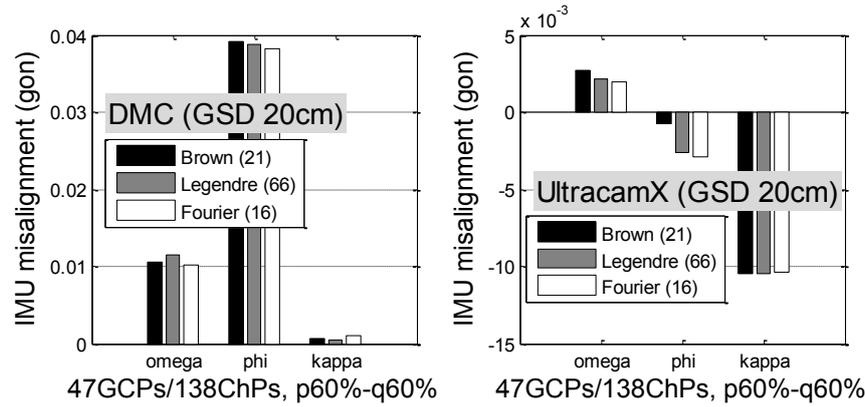
Fig. 3.18 The calibration results of the IMU misalignments in the 'DMC (GSD 20cm)' (left) and 'UltraCamX (GSD 20cm)' (right) blocks of in-situ calibration scenarios.

3.4.4 Distortion calibration

So far, the Legendre and the Fourier models perform quite closely in external accuracy, correlation analyses and the calibrations of the three IO parameters and the IMU misalignments, except that the Fourier model needs fewer APs for full calibration. In this subsection, we illustrate an important difference between these two models in the distortion calibration.

Fig. 3.19 and Fig. 3.20 illustrate the distortion determined by self-calibration models in the DMC (GSD 20cm) and UltraCamX (GSD 20cm) blocks of in-situ calibration scenarios, respectively. The left and right plots of distortion are determined by the fifth order Legendre model ("Legendre (66)") and the first order Fourier model ("Fourier (16)"), respectively. The distortion is plotted in 9×13 grid points.

It is observed from Fig. 3.19 and Fig. 3.20 that there is no significant symmetric radial pattern in these two multi-head cameras (the distortion of these composed virtual images is definitely different from that of single-head cameras). It is further found that, while the distortions determined by these two models look quite similar, the Legendre APs produce larger distortion results particularly around the extremity of image format. The Fourier APs produce more homogenous distortion result over the whole image dimension.

The differences in distortion calibration are more clearly depicted in Table 3.4, where it describes the mean and max values of the distortion on the 9×13 pattern points in the four blocks of in-situ calibration scenarios. It is observed from the columns "Legendre (66)" and "Fourier (16)" that, while the 'mean' values of both are close, the 'max' values derived by "Legendre (66)" are over twice larger than those by "Fourier (16)" (except in the DMC (GSD 20cm) block). To ensure these differences in 'max' are not caused by overparameterization, we reduce the order of the Legendre model and raise the order of the Fourier model, i.e., the fourth order Legendre model (44 APs) and the second order Fourier model (48 APs) are used. The distortion results are depicted in the columns "Legendre (44)" and "Fourier (48)" in Table 3.4, respectively. It is observed again that the Legendre APs result in much larger 'max' values than the Fourier APs. Therefore, the differences in 'max' values are unlikely the consequence of overparameterization. They are probably the negative effects of the elimination of four highly correlated terms in the Legendre APs (see Section 2.3.1). The elimination imposes four undesirable constraints and can bias the distortion determination via the polynomial APs. This may be a practical consequence of the theoretical defect of the polynomial models (including the Ebner, Grün and Legendre models). In contrast, the distortion determined by the Fourier APs should be more reliable and more realistic, due to their ideal theoretical properties.

Two other interesting observations are noteworthy. First, it is observed from Table 3.4 that the self-calibration models of *different orders* obtain different results of distortion determination. For example, in the 'DMC (GSD 20cm)' block, the 'mean' values are $2.92\mu m$ and $2.17\mu m$ by using the Fourier

models of the first order and the second order, respectively. These differences show the effects of overparameterization and underparameterization. While the self-calibration models of different orders may obtain similar external accuracy, the one deducing minimal distortion should be considered as the model of appropriate order. For the Legendre model, it is very likely that the fourth order "Legendre (44)" suffers underparameterization in the 'UltraCamX (GSD 8cm)' block, as it delivers larger 'max' and 'mean' values than "Legendre (66)". Both "Legendre (44)" and "Legendre (66)" perform quite similarly in the other three blocks. For the Fourier model, the second order "Fourier (48)" should be favored in the 'DMC (GSD 20cm)' block, while the first order 'Fourier (16)' is more appropriate in the other three blocks.

Second, those distortion results in Table 3.4 show that the distortion of a single camera vary at differnt flight heights (note that it is a same (DMC and UltraCamX) camera in the blocks of GSD 20cm and GSD 8cm). For example, the mean and max values of the DMC distortion determined by the Fourier model in the block of GSD 8cm are $1.01\mu m$ and $1.53\mu m$ respectively. They are much smaller than those corresponding values, $2.17\mu m$ and $5.21\mu m$, in the block of GSD 20cm. Similarly, for the UltraCamX camera, the mean and max values of distortion determination are $0.31\mu m$ and $0.72\mu m$ at the flight of GSD 8cm, while they are $0.54\mu m$ and $1.14\mu m$ at the higher flight of GSD 20cm. The distortion variations with flight heights are shown as well by applying the Legendre model. These variations are caused by the atmospheric influences (such as temperature, humidity and pressure) on distortion: all these influences increase with the flight altitude. This is a fact well recognized in photogrammetry (Heipke, et al., 2002), optical engineering (Lei & Tiziani, 1993) and remote sensing (Atkinson, 1993; Bannari et al., 1997). It is thus reasonable to suggest that the in-situ airborne camera calibration should be performed at a single height, same as that in related practical project.
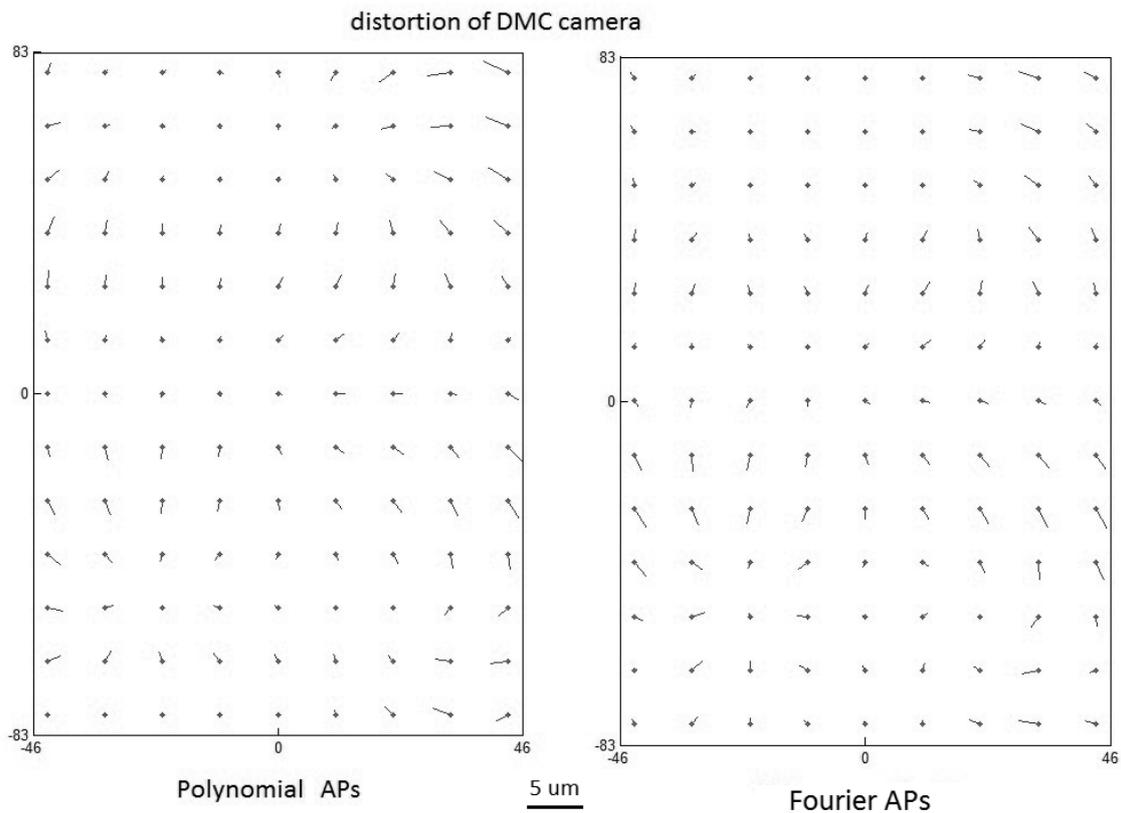

Fig. 3.19 The image distortion determined by 'Legendre (66)' (left) and 'Fourier (16)' (right) in the DMC (GSD 20cm) block of an in-situ calibration scenario.
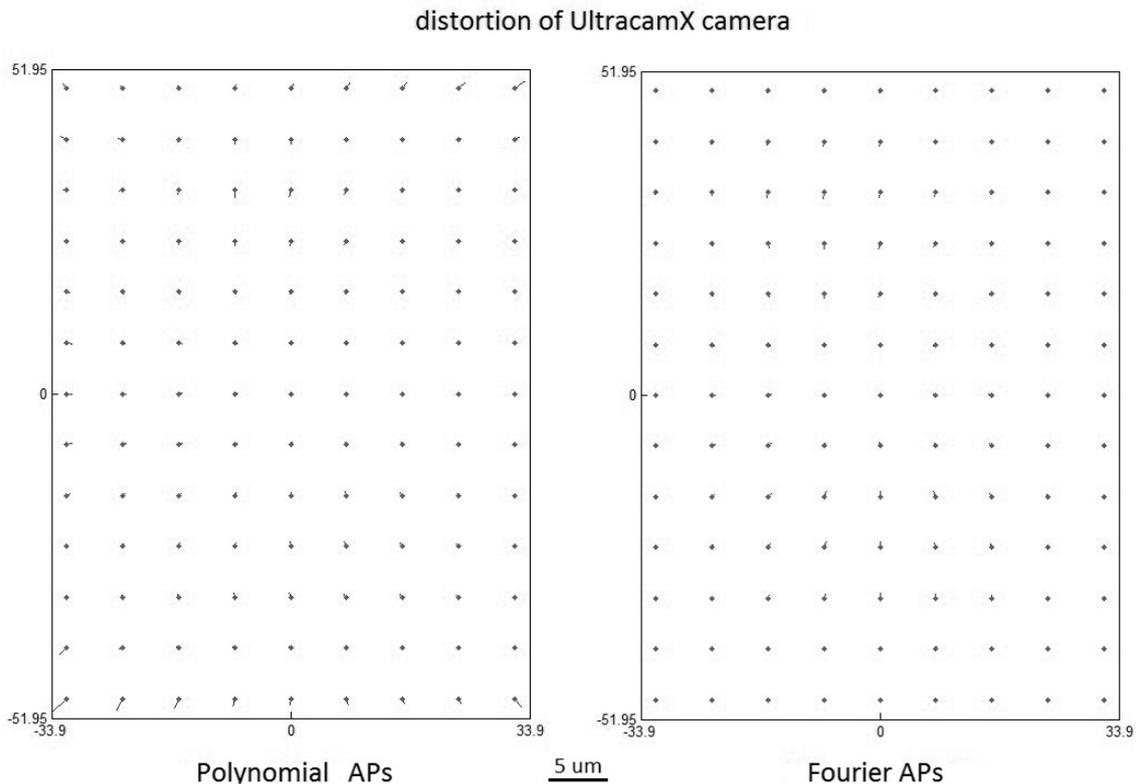
Fig. 3.20 The image distortion determined by 'Legendre (66)' (left) and 'Fourier (16)' (right) in the UltraCamX (GSD 20cm) block of an in-situ calibration scenario.

Table 3.4 Mean and max values of the distortion determined by the Legendre APs and the Fourier APs in the four blocks of in-situ calibration scenarios (unit:μm).

Mean (Max)	Legendre (44)	Legendre (66)	Fourier (16)	Fourier (48)
DMC (GSD 20cm)	2.36 (5.67)	2.39 (5.34)	2.92 (5.30)	2.17 (5.21)
DMC (GSD 8cm)	0.83 (4.66)	0.95 (3.61)	0.97 (1.54)	1.01 (1.53)
UltraCamX (GSD 20cm)	0.68 (3.28)	0.71 (3.32)	0.54 (1.14)	0.79 (1.94)
UltraCamX (GSD 8cm)	0.52 (2.42)	0.40 (1.74)	0.31 (0.72)	0.44 (1.23)

3.4.5 Overparameterization and statistical test

Two empirical examples of overparameterization are illustrated in Fig. 3.21. The Legendre models of fifth order (66 APs) and the sixth order (92 APs), and the Fourier models of first order (16 APs) and second orders (48 APs), are applied in the DMC (GSD 20cm) block of an operational project scenario. The overparameterization of "Legendre (92)" and "Fourier (48)" can be observed in Fig. 3.21. Nevertheless, the quantitative effect of overparameterization is certainly case-dependent, while it is not quite severe in these two examples (less than 4cm).

Besides correlation analysis, another statistical approach being often used in photogrammetry is statistical test (see Rao (2001) for the theoretical details). It removes the statistically insignificant APs in order to reduce the overparameterization effect. For both the Legendre and the Fourier APs, we refer "numerically insignificant AP" as the AP whose magnitude is smaller than 0.1. A numerically insignificant AP corresponds to the distortion smaller than $0.1\mu m$. It is usually found in our

experiments that, the parameters which are *statistically* insignificant (in the sense of 95% confidence level) are *numerically* insignificant, and vice versa.

Two examples in Fig. 3.22 illustrate the effects of statistical tests on the external accuracy in the DMC (GSD 20cm) block of an operational project scenario. Three different strategies are used: without eliminating any APs, eliminating the insignificant APs of the 68% confidence level and eliminating the insignificant APs of the 95% confidence level. They are denoted in Fig. 3.22 by 'without elimination', 'with 68% CL' and 'with 95% CL', respectively. The 68% and 95% levels correspond to 2-σ and 3-σ thumb rules under the normal distribution, respectively. These strategies of statistical tests are applied to the Legendre model of fifth order (66 APs) and the Fourier model of first order (16 APs). It is observed from Fig. 3.22 that applying statistical tests and eliminating insignificant APs does not necessarily improve the accuracy. Instead, retaining the insignificant parameters may be beneficial. This was mentioned as well in Ackermann (1981). The negative effects (if present) of insignificant APs can be somewhat released by the high stability and reliability of the integrated sensor orientation block.

Undoubtedly, rather than statistical tests, selecting the appropriate degree of the Legendre and the Fourier APs is much more critical to avoid overparameterization and to improve accuracy.
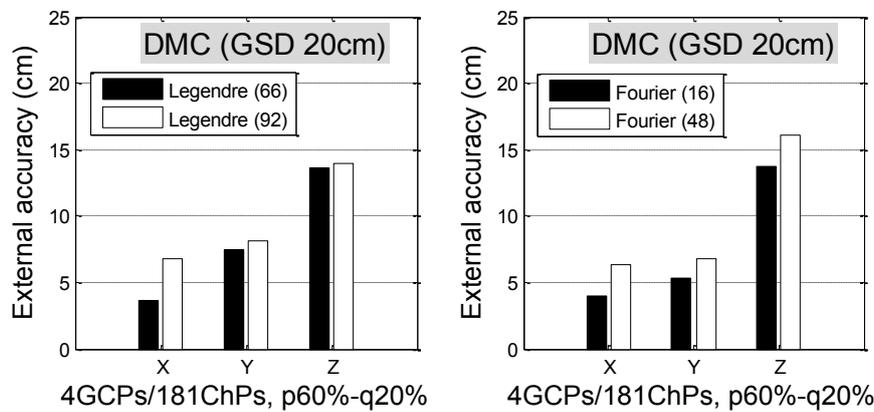

Fig. 3.21 The effects of overparameterization on the external accuracy in the DMC (GSD 20cm) block of an operational project scenario.
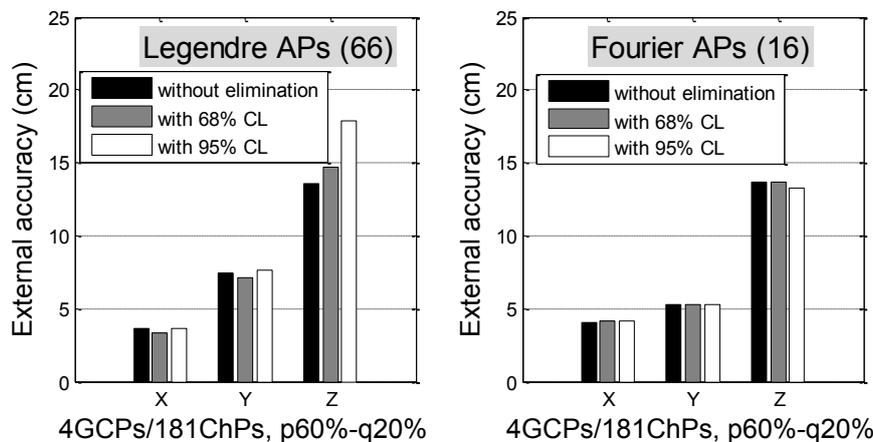

Fig. 3.22 External accuracy by applying different strategies of statistical tests in the DMC (GSD 20cm) block of an operational project scenario.

3.5 Tests in close range photogrammetry

The empirical experiments are carried out to examine the correlation analyses and the refined model of in-plane distortion in Section 2.4.3.

3.5.1 High correlations

The 10-image and 4-image simulation datasets in Section 3.1.2 are utilized. Non-zero $\Delta x_0, \Delta y_0, \Delta f$ and K_1, and $K_2 = K_3 = P_1 = P_2 = 0$ are introduced into the simulated camera. $P_1 = P_2 = 0$ indicates null decentering distortion and makes fair comparisons among the formulae (2.43), (2.50) and (2.51). The EO parameters are precisely given in self-calibration adjustment. The correlations between Δx_0 and P_1, and between Δy_0 and P_2, are depicted in Table 3.5.

It is observed from Table 3.5 that (2.50) obtain smaller correlations than the original Brown formulae (2.43); (2.51) which most resemble the polynomial models (2.49) deliver the lowest correlations in the both experiments. The formulae (2.51) reduce remarkably the correlations from over 0.90 to a much lower level, around 0.30 or even smaller. These results confirm the theoretical analyses in Section 2.4.3, that high correlations between principal point and the decentering distortion parameters are because (2.43) do not follow (2.49) to minimize correlations. In other words, these high correlations are essentially caused by the polynomial representation of the decentring distortion in the Brown model. High correlations in the polynomial self-calibration models are a distinctive characteristic of camera orientation (three IO parameters $\Delta x_0, \Delta y_0$ and Δf, and three exterior rotation angles ω, φ and κ), and they are nearly independent of the block geometry. These high correlations exist in all self-calibration models including the linear polynomial terms x, y and xy; they can be circumvented only by following the elimination rule of (2.49).

As the high correlations are inherent in the Brown model due to the polynomial representation of the decentering distortion, it needs to study their quantitative influence on the principal point location in self-calibration.

3.5.2 Principal point location

The non-zero $\Delta x_0, \Delta y_0, \Delta f, K_1, P_1$ and P_2 are introduced into the virtual camera. Considering that the decentering distortion rarely exceeds $10\mu m$ at the extremity of image format (Fraser, 1997), the extreme decentering distortion of the virtual camera is set to increase gradually from $1\mu m$ to $10\mu m$.

Two calibration strategies are performed in the highly redundant 10-image network. The parameters $\Delta x_0, \Delta y_0, \Delta f$ and K_1 are used in the adjustment of the first strategy, while in the second strategy P_1 and P_2 in (2.43) are additionally employed. The first strategy is designed to demonstrate the impact of uncompensated decentering distortion on the location of the principal point; the second one is intended to show their interaction in self-calibration.

The errors of $\Delta x_0, \Delta y_0$ and Δf (by comparing the calibration results and the true values), and sigma zero estimate a posteriori (denoted by $\hat{\sigma}_0$), are illustrated in Fig. 3.23 and Fig. 3.24 where the "max decentering distortion" indicates the distortion at the image extremity. The $\hat{\sigma}_0$ stands for a posteriori estimate of the std. dev. of the precision of image measurements. It is calculated as

$$\hat{\sigma}_0 = \sqrt{\left(\sum_i e_i^2\right)/N_{red}} \qquad (3.1)$$

where $\{e_i\}$ are the image residuals and N_{red} is the redundancy number (equal to the number of constraints minus the number of unknowns). Note that N_{red} is very large in a redundant network and it is nearly not influenced by self-calibration APs.

Table 3.5 Correlation analyses between the principal point shift and the decentering distortion of different formulae.

$(\Delta x_0 - P_1) / (\Delta y_0 - P_2)$	Eq. (2.43)	Eq. (2.50)	Eq. (2.51)
10-image	0.94/0.92	0.63/0.66	0.30/0.33
4-image	0.91/0.87	0.69/0.43	0.39/0.04
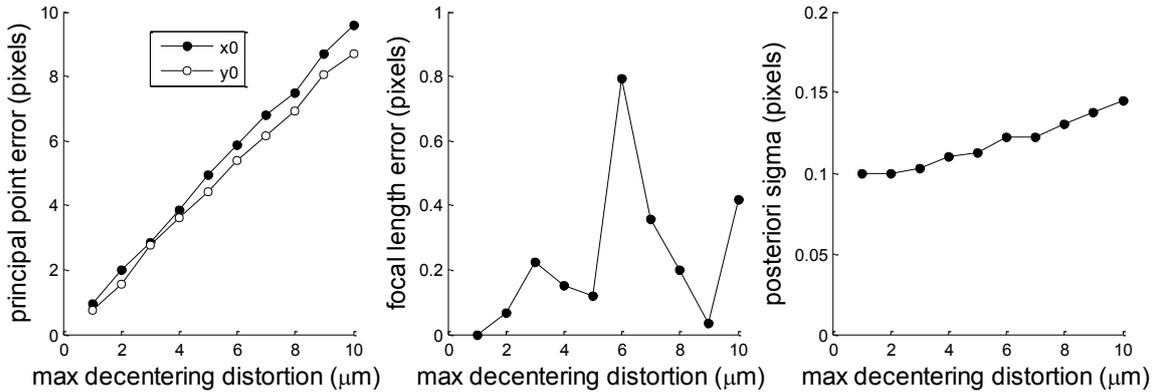
Fig. 3.23 The calibration results of principal point (left), focal length (middle) and $\hat{\sigma}_0$ (right) vary with the uncompensated decentering distortion.
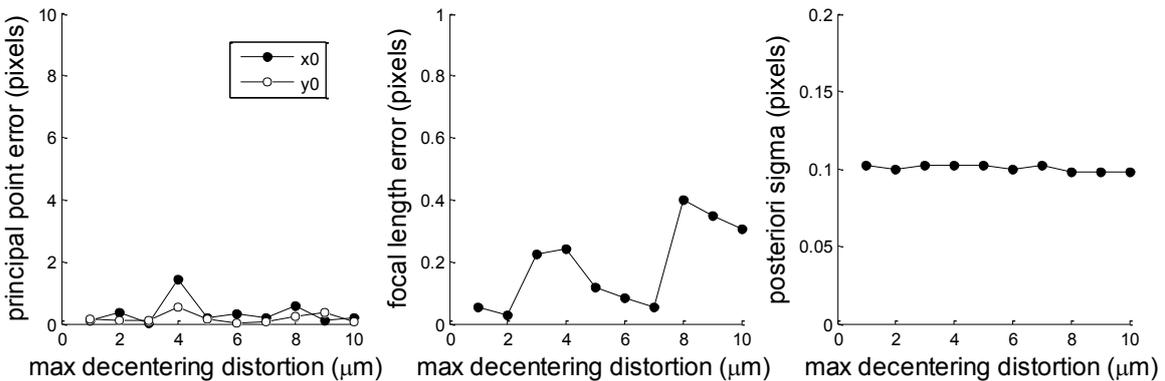
Fig. 3.24 The calibration results of principal point (left), focal length (middle) and $\hat{\sigma}_0$ (right) vary with different decentering distortion (using the decentering distortion parameters in self-calibration).

In the experiments of the first strategy (Fig. 3.23), the errors of the principal point location grow substantially with the increasing decentering distortion. This implies that the remaining decentering distortion does bias the principal point location due to the high correlations between them. On the other hand, it is certain from the increasing $\hat{\sigma}_0$ that the decentering distortion cannot be entirely compensated by the parameters Δx_0 and Δy_0. This uncompensated effect can be perceived when the $\hat{\sigma}_0$ estimate is significantly larger than 0.1 pixels. This corresponds to the decentering distortion at extremity being over $4\mu m$ and the principal point error being over 4 pixels. In other words, less than 4 pixels' bias of the principal point location is undetectable in this self-calibration due to the high correlations. It is noted as well from Fig. 3.23, that the impact of the uncompensated decentering distortion on Δf is trivial, less than 1 pixel; the impact does not increase with the decentering distortion. This must be attributed to the very low correlations between Δf and the decentering distortion parameters (smaller than 0.30 in this case).

In the experiments of the second strategy (Fig. 3.24), the high correlations between the principal point shift and the decentering distortion parameters are higher than 0.90, independent of the magnitudes of the decentering distortion. The calibration results show the precise location of the principal point, with errors less than 1 pixel. The precise location is nearly not impacted by the varied decentering distortion. The $\hat{\sigma}_0$ estimates are invariantly close to the true value 0.1 pixels. These results illustrate that the interaction between the principal point shift and the decentering parameters are trivial in self-calibration. Again, the focal length calibration is little influenced by the varied decentering distortion.

The focal length of the virtual camera is also changed to be 12 mm and 20 mm, and the experiments of the two strategies are repeated. Similar observations are obtained as those in Fig. 3.23 and Fig. 3.24. It can therefore be safely concluded that, although it is highly correlated with the decentering distortion parameters, the principal point can be reliably and precisely located in a self-calibration under the appropriate image configurations. This is a very encouraging result. It explains why the Brown model has worked so well in practice regardless of high correlations. As the negative effects of high correlations are trivial, the early works, which attempted to circumvent the high correlations between the principal point shift and the decentering parameters, become unnecessary.

The precise location of the principal point irrespective to high correlations may not be surprising. It should be noted that, although high correlations do cause the risk of miscalibration, it is usually circumstance-dependent whether the miscalibration is practically significant. On the one hand, high correlation stands mathematically for a significant linear relation between two parameters. On the other hand, the quantitative influence of one parameter on another depends on many factors, such as the magnitudes of parameters and the scaling factor (geometrically, the gradient of the linear dependence). The scaling factor of the linear correlations between Δx_0 and P_1, and between Δy_0 and P_2, might be quite small (though unproved here). The limited magnitude of the decentering distortion, which is usually smaller than $10\mu m$, is also beneficial.

As the decentering distortion has been shown to be significant in most digital camera lens (Brown, 1966; Fraser, 1997; McGlone et al., 2004) and the harmful effects of high correlations are insignificant in self-calibration, it is suggested that the decentering distortion parameters should be employed in self-calibration whenever possible. The use of the decentering distortion parameters not only reduces the residuals of image measurements, but also improves the accuracy of the principal point location.

3.5.3 In-plane distortion

The simulation data and the empirical data with 12 mm focal length in Section 3.1.2 are experimented to evaluate the performance of the two in-plane distortion formulae (2.45) and (2.52). The experiments of 10-image simulation, 4-image simulation and the empirical test of ten images are denoted by 'simulation-10', 'simulation-4' and 'practical-10', respectively. The values of $\Delta f = 50\mu m$ and $B_1 = B_2 = 0$ are introduced into the virtual cameras. The self-calibration results and the correlation between B_1 and Δf (denoted by R_{fB}) are depicted in Table 3.6.

In both experiments 'simulation-10' and 'simulation-4', (2.45) and (2.52) obtain the same $\hat{\sigma}_0$. This is mainly due to the zero in-plane distortion, i.e., $B_1 = B_2 = 0$, thus (2.45) and (2.52) has no impact on the $\hat{\sigma}_0$ estimate. The slight refinement of Δf and R_{fB} is observed by using (2.52), particularly in the case of 'simulation-4' where the network geometry is weak. The refined performance is due to that (2.52) which include additional terms $-B_1\bar{y}$ follow the spirit of (2.49) to minimize correlations. In the practical experiments 'practical-10', (2.52) obtain slightly smaller R_{fB} than (2.45). The difference of Δf calibration is insignificant. This may be due to quite small in-plane distortion which is smaller than 0.05 pixels in this digital camera.

These results coincide with the theoretical conclusion in Section 2.4.3, that (2.52) perform similarly to (2.45) but help to reduce the correlation between B_1 and Δf and to refine the Δf calibration. The amount of refinement by using (2.52) depends on the magnitude of the in-plane distortion and the image configuration.

Table 3.6 Self-calibration results by using two in-plane distortion models.

Experiments	Models	$\widehat{\sigma}_0$ (μm)	Δf (μm)	R_{fB}
Simulation-10	Eq. (2.45)	0.41	50.3	-0.81
	Eq. (2.52)	0.41	50.0	-0.75
Simulation-4	Eq. (2.45)	0.38	48.3	-0.78
	Eq. (2.52)	0.38	50.2	-0.60
Practical-10	Eq. (2.45)	0.26	46.1	-0.83
	Eq. (2.52)	0.26	45.8	-0.80

Table 3.7 Statistical values of the self-calibration by using three different self-calibration models.

Statistics	Cameras	Brown model (10)	Radial + Legendre (18)	Radial + Legendre (32)	Radial + Fourier (22)
$\widehat{\sigma}_0$ (μm)	f = 8mm	0.42	0.41	0.37	0.38
	f = 12mm	0.26	0.25	0.25	0.25
Max correlation	f = 8mm	0.89	-0.63	-0.62	-0.52
	f = 12mm	0.92	-0.80	-0.73	-0.88
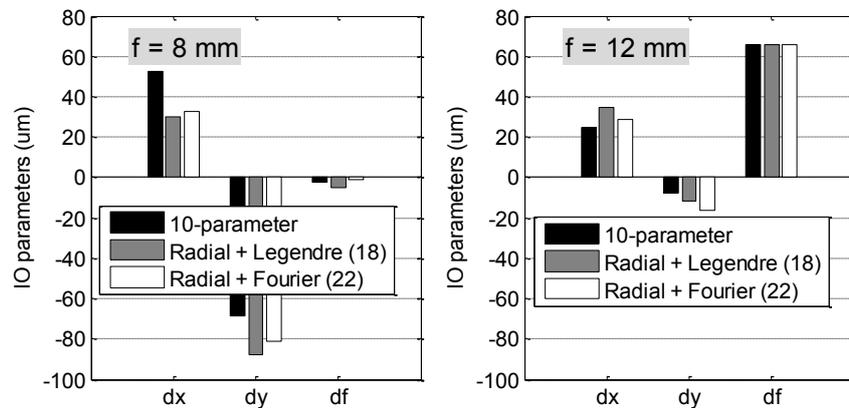
Fig. 3.25 The calibration results of the three IO parameters for the lens systems with focal length 8 mm (left) and 12 mm (right), by using three different self-calibration models.

3.5.4 Combined models

It is suggested in Section 2.3.3 that the Legendre or the Fourier APs should be combined with the radial distortion parameters to calibrate the distortion which contains significant radial tendency. In this subsection, the combined models of "Radial + Legendre" and "Radial + Fourier" are tested in calibrating the two close range lenses introduced in Section 3.1.2. The Legendre model of second order and the Fourier model of first order are chosen; the "Radial + Legendre" and "Radial + Fourier" models have thus 18 and 22 APs (together with Δx_0, Δy_0 and Δf), respectively. They are denoted by "Radial + Legendre (18)" and "Radial + Fourier (22)", respectively. The APs' number of the combined models has little influence on the redundancy N_{red} which is about 4,000 in the experiments.

The performance of these two combined models is compared to the classical 10-parameter model (2.47). The calibrations of the three IO parameters by using the three self-calibration models are illustrated in Fig. 3.25; $\hat{\sigma}_0$ and the max correlations between the three IO parameters and other APs are depicted in Table 3.7.

For the first lens with $f = 8mm$, the "Radial + Fourier (22)" model obtains smallest $\hat{\sigma}_0$ while the 10-parameter get max $\hat{\sigma}_0$. The $\hat{\sigma}_0 = 0.41$ in "Radial + Legendre (16)" is mainly due to the underparamterization of the second order Legendre APs. The $\hat{\sigma}_0$ is decreased to 0.37 when the degree of the Legendre model is increased to the third order, as illustrated in the column of "Radial + Legendre (32)". From Fig. 3.25 (left), the "Radial + Legendre" and "Radial + Fourier" models obtain closer calibration results of the three IO parameters.

For the second lens with $f = 12mm$, the three models get very similar $\hat{\sigma}_0$. Comparing the results of "Radial + Legendre (16)" and "Radial + Legendre (32)", it is interestingly found that increasing the order of the Legendre model does not further reduce $\hat{\sigma}_0$. This indicates that the Legendre model of second order does not suffer underparameterization in this case. Moreover, it is seen from Fig. 3.25 (right) that very coincident results of the three IO parameters are obtained by all the three models.

The posterior check after the experiments finds that the lens system with $f = 8\,mm$ does not well fit the uEye camera (the radial distortion at the image extremity is even over 100 pixels). The classic 10-parameter model might be unsuitable in such case, while the combined models appear to be quite effective. The combined models are capable to calibrate not only the radial distortion, but other distortion by using the Legendre or the Fourier model.

These experiments demonstrate the good performance of the combined "Radial + Legendre" and "Radial + Fourier" models in close range camera calibration. They particularly show the generic effectiveness of the Legendre and the Fourier models. These two models, based on approximation principle, are able to compensate the decentering, the in-plane and the out-of-plane distortion, and others. These combined models can be very useful in the cases where the Brown or the 10-parameter model is inadequate, such as the calibration of all-reflective cameras (Seidl et al., 2011) and the current example of the lens with 8mm focal length.

3.6 Discussions

3.6.1 Physical and mathematical self-calibration models

The high performance of the Legendre and the Fourier self-calibration models has been identified in a number of empirical tests on airborne camera calibration. Both theoretical justification and practical tests show that these two models should be preferred to many conventional mathematical counterparts such as those by Ebner (1976), Grün (1978) and El-Hakim & Faig (1977). The combined models of "Radial + Legendre" and "Radial + Fourier" are shown to be quite effective even in the close range camera calibration.

However, this should not lead to a hasty conclusion that the Legendre and Fourier models (and the combined models) are even preferable to the physical models. Instead of picking a winner, it is more appropriate and more reasonable to discuss the advantages and disadvantages of the mathematical and the physical self-calibration models, from both theoretical and practical viewpoints.

It needs to specify the range of mathematical and physical models to be discussed:

- the physical self-calibration models indicate those established on the base of the knowledge on distortion sources, such as those by Brown (1971, 1976), Fraser (1997) and Jacobson (1982, 2007); and

- the mathematical self-calibration models indicate those established on the abstract principle of function approximation, such as those by Ebner (1976), Grün (1978) and El-Hakim & Faig (1977), the Legendre and the Fourier models.

On the one hand, the physical self-calibration models are usually quite compact and efficient since they are built on the base of precise knowledge on distortion. Each AP in the physical models is physically interpretable. Nevertheless, physical models may encounter underparameterization due to the limit of knowledge. They may need to be altered to fit different camera manufacturing technologies (such as multi- or single-head cameras, and all-reflective cameras). Some physical APs may be highly correlated with other correction parameters.

On the other hand, the mathematical self-calibration models are established (explicitly or implicitly) on the abstract mathematical principle of function approximation. They are independent of the physical sources of distortion. Particularly, the Legendre and the Fourier self-calibration models are theoretically rigorous, flexible and generically effective. While the calibration accuracy of the physical models depends on how precise the empirical knowledge is on distortion, the Legendre and the Fourier models are capable to compensate the distortion of very small magnitude (smaller than 0.05 pixels in the tests in Section 3.4.4). They are thus very useful in the cases where the empirical knowledge is biased or insufficiently precise while very high accuracy is desired. The Legendre and the Fourier APs are very low correlated with other parameters and thus able to deliver reliable and precise calibration results. Yet, the mathematical APs are not physically interpretable. The risk of overparameterization needs to be cautioned.

A synthetic view, which follows the principle of the physical and the mathematical modeling approaches in Section 2.1.1, may be helpful to further understand the advantages and disadvantages. Mathematically speaking, an unknown (distortion) function may be divided into two parts: one with significant tendency and one lacking apparent pattern. The first part should be modeled using empirical functions via the physical modeling approach, while the second part, which is difficult to be exactly modeled, can be approximated via the mathematical modeling approach. Practically, the physical models can be used to compensate the major distortion (such as the radial distortion), while the mathematical models should be favored to compensate the remaining distortion which is not accounted by the physical models or for which it is hard to find close forms. In a word, it is rather fair that "each must be considered within its own right" (Ackermann, 1981) for the physical and the mathematical models. Their advantages and disadvantages are summarized in Table 3.8.

To take the advantages of both the physical and the mathematical self-calibration models, it is recommendable to apply their combination if necessary. The combined models exploit the knowledge on distortion as well as take advantages of function approximation. The combined "Radial + Legendre" and "Radial + Fourier" models are proposed in our work. They are shown to be quite effective in calibrating both the airborne cameras and the close range cameras (it is an interesting question why the degrees of the Legendre and the Fourier models are usually higher in airborne camera calibration than those in close range camera calibration? This is mainly because the precision of calibration is application-dependent. In aerial photogrammetry, the distortion of small magnitude may considerably degrade the external accuracy, due to very large scale H/f where H is the flight height (or the scene depth in the close range case). Therefore, the Legendre and the Fourier models of sufficiently high degree are desired in airborne camera calibration. However, the scale is much smaller in close range photogrammetry. The remained tiny distortion may be practically trivial, while the overparameterization should be avoided to maintain the block stability).

3.6.2 Calibration network

For a successful self-calibration, an appropriate self-calibration model and an adequate calibration network (image configuration) are necessary. This can be better understood from the following stochastic equation which is the linearization of the collinearity equations (1.4):

Table 3.8 Advantages and disadvantages of the physical and the mathematical self-calibration models in photogrammetry.

	Physical APs	**Mathematical APs**
Advantages	Compact and efficient;	Rigorous, flexible, generic and effective;
	Physically interpretable;	Independent of the physical sources of distortion;
	Capable to compensate the radial distortion (main distortion in many lenses);	Capable to compensate very small distortion;
		Low correlated with other parameters;
	Significant for close range application.	Significant for large scale application (aerial and space) and wherever the knowledge on distortion is unavailable.
Disadvantages	Dependent on the physical knowledge;	Not physically interpretable;
	Risk of high correlation;	Risk of overparameterization.
	Risk of underparameterization.	

$$y = \mathrm{A}x + \mathrm{B}z + \varepsilon, \varepsilon \sim (0, \mathrm{P}^{-1}) \tag{3.2}$$

where

- y stands for the observations (vector);
- x stands for the EO parameters and the coordinates of object points (the unknowns in the ideal collinearity equations (1.3));
- z stands for the correction parameters (including self-calibration APs) and ε for the random noise; and
- A and B are the design matrix or coefficient matrix, and P^{-1} the variance matrix.

All these parameters are relevant to a successful self-calibration. Particularly,

- an adequate A indicates an calibration network of sufficiently strong geometry;
- an adequate B indicates an appropriate calibration model; and
- the adequate ε and P^{-1} indicate the sufficient precision of observations.

An adequate A is critical for the precise solutions of x and z. As illustrated in Section 3.2.2, when A is inadequate (block geometry is weak), one cannot obtain the precise estimates of x and z, even if B is perfect (calibration model is perfect).

The pyhsical interpretation of the matrix A depends on the types of netwrok geometry. Brown (1989) suggested the following criteria to get an adequate A for the close range camera calibration:

(1) a single camera must be used to take at least three images of the object;
(2) both the interior geometry of the camera and the point to be measured on the object must remain stable during the measurement process;
(3) the photogrammetric network must be strong and exercise a high degree of convergence;
(4) at least one image must have a roll angle that is significantly different from the others; and
(5) a relatively large number of well distributed points should be used.

According to the simulation study in Section 3.2.2 and the practical tests in Section 3.3 and Section 3.4, the following requirements should be satisfied to produce an adequate design matrix A for the in-situ airborne camera calibration:

(1) a sufficient number of GCPs are well distributed in the block;
(2) high side overlapping levels are beneficial. The cross flights are not mandatory but maybe helpful;

(3) at least one flight is in different direction. It corresponds somehow to the fourth criterion in the Brown's suggestion. The inverse directions of adjacent flight lines are recommended; this flight pattern is of practical and economic convenience; and

(4) a flight of a single height should be operated since the atmospheric influences on lens distortion may vary with altitude, as mentioned in Section 3.4.4.

3.7 Concluding remarks

Extensive tests are preformed to evaluate the performance of the new calibration models developed in last chapter.

The high performance of the Legendre and the Fourier self-calibration models has been identified in the practice of airborne camera calibration. They are rigorous, generic, flexible and effective. They possess many advantages on the conventional counterparts. In general, they are able to calibrate the distortion of digital frame airborne cameras of large-, medium- and small-formats, mounted in single- and multi-head systems.

The correlation analyses in the Brown model are carried out in simulation and practical experiments. The new in-plane distortion model is shown to get lower correlations with focal length and better calibration of it.

By discussing the advantages and disadvantages of the mathematical and the physical models, it is recommended that the mathematical and the physical models should be combined together in many calibration applications.

4 Auto-Calibration in Computer Vision

"I had no need of that hypothesis."

—— Pierre-Simon Laplace (1749 – 1827).

4.1 Projective geometry

While photogrammetry utilizes *Cartesian* coordinates in *Euclidean* geometry, computer vision applies *homogenous* coordinates in *projective* geometry. Homogenous coordinates have an advantage that the points, lines and planes at infinity can be represented using finite coordinates.

4.1.1 Homogenous coordinates in projective geometry

The homogenous coordinates of a point $(x, y)^T$ in the two-dimensional (2D) space are $(x, y, 1)^T$, and the homogenous coordinates of a 3D point $(x, y, z)^T$ are $(x, y, z, 1)^T$. Further, the homogenous representation of a line $(ax + by + c = 0)$ in the 2D space is naturally $(a, b, c)^T$, and that of a line $(ax + by + cz + d = 0)$ in the 3D space is $(a, b, c, d)^T$.

The homogenous coordinates have the following distinctive properties.

(1) For any $a \neq 0$, $(x, y, 1)^T$ and $(ax, ay, a)^T$ represent the same point in the 2D space. Analogously, $(x, y, z, 1)^T$ and $(ax, ay, az, a)^T$ are the same point in the 3D space for $a \neq 0$;
(2) The point at infinity in the 2D and 3D space is represented as $(x, y, 0)^T$ and $(x, y, z, 0)^T$, respectively;
(3) For any $k \neq 0$, $(a, b, c)^T$ and $(ka, kb, kc)^T$ represent a same line in the 2D space; $(a, b, c, d)^T$ and $(ka, kb, kc, kd)^T$ are the same line in the 3D space;
(4) The point x lies on the line l if and only if $x^T l = 0$; and
(5) The intersection point of two lines l and l' is represented as $x = l \times l'$, where $\times$ denotes the cross product operation. Parallel lines intersect at a point at infinity.

The homogenous representation of the central projection in projective geometry is a linear equation, i.e., equation (1.11).

4.1.2 Fundamental matrix and essential matrix

The fundamental matrix and the essential matrix are two basic concepts in computer vision. The homogeneous coordinates of an image point are indicated by $x = (x, y, 1)^T$. x and x' are the corresponding points in epipolar geometry. They satisfy

$$xFx' = 0 \tag{4.1}$$

where the matrix F is named as the *fundamental matrix*. The fundamental matrix, independent of scene structure, is the algebraic representation of epipolar geometry when the calibration matrices are unknown. It is a matrix with rank 2 and 7 degrees of freedom (a 3×3 matrix has 8 degrees of freedom by ignoring a scale factor, e.g., the norm of the matrix is one).

The epipolar geometry can be further represented by an *essential matrix* if the calibration matrices are known. An important property of the essential matrix is described in the following theorem.

Theorem 3 (Essential Matrix)

> *A 3×3 real non-zero matrix* E *is an essential matrix, if and only if two of its singular values are equal, and the third is zero. Equivalently,* E *is an essential matrix if and only it satisfies* detE $= 0$ *and the following algebraic formula,*

$$2EE^TE - tr(E^TE)E = 0 \qquad (4.2)$$

> *where* $tr(\cdot)$ *denotes the trace of a matrix.*

A proof of this theorem is given in Appendix D.3. It can be further shown that (4.2) provides two independent constraints. The essential matrix has thus rank 2 and 5 degrees of freedom. At least seven and five corresponding points are therefore needed to compute the fundamental matrix and essential matrix, respectively. An algebraic relation between the fundamental matrix and the essential matrix is given by

$$E = K'^TFK \qquad (4.3)$$

where K and K′ are the two calibration matrices in epipolar geometry. As the skew parameter is zero in most practices (Hartley & Zisserman, 2003), the camera matrix with zero-skew is given as

$$K = \begin{pmatrix} f_p & 0 & u_0 \\ 0 & \alpha f_p & v_0 \\ 0 & 0 & 1 \end{pmatrix}. \qquad (4.4)$$

Many outstanding works have been accomplished on the fundamental matrix and the essential matrix. For intensive materials the readers are referred to such as Luong & Faugeras (1996) and Hartley & Zisserman (2003).

4.1.3 Camera auto-calibration

Auto-calibration is to determine a constant calibration matrix, K = K′ in (4.3), by using only image correspondences from multiple views. The skew parameter is often fixed as zero as (4.4). Auto-calibration does NOT require any prior information on camera motion, scene constraints or the internal parameters. Image distortion is not accounted and camera is "undistorted".

There are four unknowns in calibration matrix to be calibrated. Two fundamental matrices are thus principally sufficient to calculate a calibration matrix, since each essential matrix offers two independent constraints.

4.1.4 Focal length calibration from two-view

A recent study is on estimating a constant focal length from two views by fixing the other internal parameters and given image correspondences (Stewénius et al., 2005; Sturm et al., 2005; Li, 2008). Yet, not all of them are capable to obtain a good calibration of focal length. The performance of the method in Li (2008) may depend on the definition of the interval of kernel-voting. Moreover, these methods need to know principal point and aspect ratio (and the skew parameter) in advance. Yet, the information on the principal point is often unavailable in practice.

In this chapter, we will study calibrating the focal length from two views by given aspect ratio only but without any knowledge of the principal point. This two-view calibration method is more flexible and more useful.

4.2 Auto-calibration solution

Our auto-calibration solution is based on the fundamental matrix and the two constraints of the essential matrix, i.e., equation (4.2). Its main virtues are threefold. Firstly, it utilizes an appropriate center-oriented coordinate transformation, with which the focal length and aspect ratio can be well estimated independent of the unknown principal point shift. Consequently, in contrast to the conventional methods which reconstruct simultaneously all the internal parameters, our method utilizes a *recursive* procedure. It first estimates focal length and aspect ratio, and then calculates the principal point by fixing the estimates of focal length and aspect ratio. The principal point estimate returns to update the calibration of the focal length and aspect ratio, and so on so forth. Secondly, the technique of error propagation is introduced to select the optimal geometrical constraints. The selection of optimal constraints is important for precise calibration and fast convergence. Thirdly, the Levenberg–Marquardt algorithm is adopted for the final nonlinear optimization by using the recursive results as the initial values. This nonlinear procedure is very fast since it is performed on the four unknown internal parameters.

4.2.1 Coordinate transformation

The pixel coordinates of image points, denoted by $(u, v, 1)^T$, are transformed by multiplying with a matrix T_m:

$$\begin{pmatrix} x \\ y \\ 1 \end{pmatrix} = T_m \begin{pmatrix} u \\ v \\ 1 \end{pmatrix}, \qquad T_m = m_t \begin{pmatrix} 1 & 0 & -\tilde{u}/2 \\ 0 & 1 & -\tilde{v}/2 \\ 0 & 0 & 1/m_t \end{pmatrix} \tag{4.5}$$

where $(\tilde{u}, \tilde{v})$ indicates image resolution (unit: pixels) and m_t is a positive scale factor. T_m transforms the pixel coordinates to a new center-oriented coordinate system.

The new coordinates $(x, y, 1)^T$ will be used in our auto-calibration procedure. Consequently, the output of the internal parameters can be transferred back to the pixel coordinates by using

$$f_p = \frac{f}{m_t}, \qquad \begin{pmatrix} u_0 \\ v_0 \\ 1 \end{pmatrix} = T_m^{-1} \begin{pmatrix} x_0 \\ y_0 \\ 1 \end{pmatrix} = \begin{pmatrix} \dfrac{x_0}{m_t} + \dfrac{\tilde{u}}{2} \\ \dfrac{y_0}{m_t} + \dfrac{\tilde{v}}{2} \\ 1 \end{pmatrix} \tag{4.6}$$

where f, x_0 and y_0 are the focal length and the principal point in the new coordinates.

It will be demonstrated that the selection of m_t may play a significant role particularly in two-view calibration. It is suggested empirically that

$$m_t \in \{1 \times 10^{-1}, 1 \times 10^{-2}, 1 \times 10^{-3}, 1 \times 10^{-4}, 1 \times 10^{-5}, 1 \times 10^{-6}\}. \tag{4.7}$$

For self-calibration from multiple views, $m_t = 1 \times 10^{-6}$ is often selected.

4.2.2 Mathematical derivations

Let $F = USV^T$ by using the singular value decomposition (SVD) of the fundamental matrix F. Denote

$$U = (u_{ij}), \qquad V = (v_{ij}), \qquad i, j = 1, 2, 3$$
$$S \triangleq \begin{pmatrix} s_1 & 0 & 0 \\ 0 & s_2 & 0 \\ 0 & 0 & 0 \end{pmatrix} \tag{4.8}$$

where U and V are the orthogonal matrix and satisfy $UU^T = VV^T = I_{3\times3}$ (identity matrix).

Noticing $tr(AB) = tr(BA)$ for any matrices A and B, it is obtained from (4.2) and (4.3):

$$2KFK^TKF^TK^TKFK^T - tr(KF^TK^TKFK^T)KF^TK^T = 0 \tag{4.9}$$

$$0 = 2SV^TK^TKVSU^TK^TKUS - tr(SV^TK^TKVSU^TK^TKU)S$$
$$\triangleq 2SNSMS - tr(SNSM)S \tag{4.10}$$

where

$$M = M^T = U^TK^TKU \triangleq (m_{ij})$$
$$N = N^T = V^TK^TKV \triangleq (n_{ij}) \; . \tag{4.11}$$
$$i, j = 1, 2, 3$$

K^TK is called the dual image of the absolute conic (DIAC) which was important in early calibration literatures (Hartley & Zisserman, 2003).

Denote

$$T \triangleq SNSMS = (t_{ij}), \qquad i, j = 1, 2, 3. \tag{4.12}$$

The matrix T has the form as:

$$T = \begin{pmatrix} t_{11} & t_{12} & 0 \\ t_{21} & t_{22} & 0 \\ 0 & 0 & 0 \end{pmatrix} \tag{4.13}$$

where

$$t_{11} = s_1(s_1^2 m_{11} n_{11} + s_1 s_2 m_{12} n_{12})$$
$$t_{12} = s_2(s_1^2 m_{12} n_{11} + s_1 s_2 m_{22} n_{12})$$
$$t_{21} = s_1(s_2^2 m_{12} n_{22} + s_1 s_2 m_{11} n_{12}) \tag{4.14}$$
$$t_{22} = s_2(s_2^2 m_{22} n_{22} + s_1 s_2 m_{12} n_{12})$$

and

$$tr(SNSM) = \frac{t_{11}}{s_1} + \frac{t_{22}}{s_2} . \tag{4.15}$$

Then, the following three formulae can be derived from (4.10) – (4.15):

$$s_1^2 m_{11} n_{11} - s_2^2 m_{22} n_{22} = 0 \tag{4.16}$$

$$s_1 m_{12} n_{11} + s_2 m_{22} n_{12} = 0 \tag{4.17}$$

$$s_1 m_{11} n_{12} + s_2 m_{12} n_{22} = 0. \tag{4.18}$$

Obviously, these three interdependent equations, of which any two are independent, correspond to the two independent constraints in (4.2). For instance, (4.18) can be derived by inserting (4.17) (using $s_2 m_{22} = -s_1 m_{12} n_{11}/n_{12}$) into (4.16).

Equations (4.16) – (4.18) are the fundamental constraints in our calibration method. They are named as the *Constraints I, II* and *III*, respectively. They can be viewed as the functions of the four internal parameters, denoted by $C_i(f, \alpha, x_0, y_0)$ $(i = 1, 2, 3)$ or represented as $C(f, \alpha, x_0, y_0)$ in general. The three constraints contain m_{ij} and n_{ij} $(i, j = 1, 2)$ only. m_{ij} $(i, j = 1, 2)$ are derived as

$$\begin{aligned}
m_{11} &= (u_{11}^2 + \alpha^2 u_{21}^2)f^2 + u_{31}(u_{31} + 2u_{11}x_0 + 2u_{21}y_0) \\
&\quad + 2u_{11}u_{21}x_0y_0 + u_{11}^2 x_0^2 + u_{21}^2 y_0^2 \\
&= (u_{11}^2 + \alpha^2 u_{21}^2)f^2 + (u_{31} + u_{11}x_0 + u_{21}y_0)^2
\end{aligned} \tag{4.19}$$

$$\begin{aligned}
m_{12} = m_{21} &= (u_{11}u_{12} + \alpha^2 u_{21}u_{22})f^2 + u_{31}u_{32} + (u_{12}u_{31} + u_{11}u_{32})x_0 \\
&\quad + (u_{22}u_{31} + u_{21}u_{32})y_0 + +(u_{21}u_{12} + u_{11}u_{22})x_0y_0 + u_{11}u_{12}x_0^2 + u_{21}u_{22}y_0^2 \\
&= (u_{11}u_{12} + \alpha^2 u_{21}u_{22})f^2 + (u_{31} + u_{11}x_0 + u_{21}y_0)(u_{32} + u_{12}x_0 + u_{22}y_0)
\end{aligned} \tag{4.20}$$

$$\begin{aligned}
m_{22} &= (u_{12}^2 + \alpha^2 u_{22}^2)f^2 + u_{32}(u_{32} + 2u_{12}x_0 + 2u_{22}y_0) \\
&\quad + 2u_{12}u_{22}x_0y_0 + u_{12}^2 x_0^2 + u_{22}^2 y_0^2 \\
&= (u_{12}^2 + \alpha^2 u_{22}^2)f^2 + (u_{32} + u_{12}x_0 + u_{22}y_0)^2
\end{aligned} \tag{4.21}$$

Similar formulae can be built as well for n_{ij} $(i, j = 1, 2)$, just replacing u_{ij} by v_{ij} in (4.19) – (4.21).

4.2.3 Recursive solution

As the first approximation of (4.19) and (4.21), we adopt

$$\begin{aligned}
(u_{31} + u_{11}x_0 + u_{21}y_0)^2 &\approx u_{31}^2 \\
(u_{32} + u_{12}x_0 + u_{22}y_0)^2 &\approx u_{32}^2
\end{aligned} \tag{4.22}$$

Then, (4.17) and (4.19) can be reduced as (4.23) and (4.24), respectively:

$$m_{11} \approx (u_{11}^2 + \alpha^2 u_{21}^2)f^2 + u_{31}^2 \tag{4.23}$$

$$m_{22} \approx (u_{12}^2 + \alpha^2 u_{22}^2)f^2 + u_{32}^2 . \tag{4.24}$$

Similar approximation of n_{11} and n_{22} can be derived similarly to (4.23) and (4.24), respectively.

As the Constraint I (4.16) contains the terms m_{ii} and n_{ii} $(i = 1, 2)$ only, it can be reduced to be a function of f^2 and α^2 by using (4.23) and (4.24). The reduced Constraint I is

$$\begin{aligned}
&s_1^2[(u_{11}^2 + \alpha^2 u_{21}^2)f^2 + u_{31}^2][(v_{11}^2 + \alpha^2 v_{21}^2)f^2 + v_{31}^2] \\
&- s_2^2[(u_{12}^2 + \alpha^2 u_{22}^2)f^2 + u_{32}^2][(v_{12}^2 + \alpha^2 v_{22}^2)f^2 + v_{32}^2] = 0
\end{aligned} \tag{4.25}$$

The approximation (4.22) which disregards the unknown principal point shift makes a recursive solution possible and feasible. Given more than two fundamental matrices, the f and α can be calculated from (4.25)-alike equations. Solving two (4.25)-alike equations is a plain work and the

simple elimination technique is workable. Particularly, eliminating α gets a fourth order polynomial of f^2, and eliminating f obtains a sixth order polynomial of α^2. Subsequently, the estimates of f and α are applied as fixed values into the constraints (4.16) – (4.18) to calculate the principal point. The principal point calculation is then turned back to (4.16) – (4.18) to refine the calibration of f and α. This recursive process proceeds until the convergent limit is satisfied. The details on recursion are presented in the next subsections.

According to this recursive theme, by given x_0 and y_0, the three constraints are the functions of f^2 and α^2 with the general form

$$a_1\alpha^4f^4 + a_2\alpha^2f^4 + a_3\alpha^2f^2 + a_4f^4 + a_5f^2 + a_6 = 0 \tag{4.26}$$

where the coefficients $\{a_i\}_{i=1,\dots,6}$ are the polynomials of x_0 and y_0. Analogously by given f^2 and α^2, the three constraints can be rewritten as the functions of x_0 and y_0 with the general form

$$\begin{aligned} b_1x_0^4 + b_2x_0^3y_0 + b_3x_0^3 + b_4x_0^2y_0^2 + b_5x_0^2y_0 + b_6x_0^2 + b_7x_0y_0^3 + b_8x_0y_0^2 \\ +b_9x_0y_0 + b_{10}x_0 + b_{11}y_0^4 + b_{12}y_0^3 + b_{13}y_0^2 + b_{14}y_0 + b_{15} = 0 \end{aligned} \tag{4.27}$$

where the coefficients $\{b_i\}_{i=1,\dots,15}$ are the polynomials of f^2 and α^2. Both $\{a_i\}$ and $\{b_i\}$ can be derived from (4.16) – (4.18).

Two important issues are noteworthy. First, the factor m_t in (4.5) has a remarkable impact on the approximation (4.25), since the matrices U and V varies with m_t. The appropriate m_t should be chosen so that the approximation (4.22) holds well as much as possible or, equivalently, (4.25) approximates as closely as possible to (4.16). Second, although (4.25) is equal to (4.16) with $x_0 = y_0 = 0$, (4.25) may not be viewed to equal the assumption of zero principal point shift. The approximation (4.22) holds if $|u_{11}x_0 + u_{21}y_0| \ll |u_{31}|$ (or $u_{11}x_0 + u_{21}y_0 \approx -2u_{31}$) and $|u_{12}x_0 + u_{22}y_0| \ll |u_{32}|$ (or $u_{12}x_0 + u_{22}y_0 \approx -2u_{32}$). These conditions are certainly much weaker than zero assumption $x_0 = y_0 = 0$.

4.2.4 Principal point calculation

There are solutions potential to calculate the principal point x_0 and y_0 from two (4.27)-alike equations. Using elimination technique will obtain a 44th-oder univariate polynomial of x_0 or y_0. Deriving a polynomial of such high order is however technically difficult and numerically unstable. The numerical methods based on the algebraic geometry techniques might be useful, but they can be very slow and unstable (Cox et al., 2004). The automatic generator (Kukelova et al., 2008) had been employed for solving the equations, but it was totally blocked by the complexity of (4.27). The nonlinear iterative techniques which require good initial values may thus lead to a poor convergence.

In fact, a simple approximation can easily circumvent these difficulties, thanks to the convenience of the coordinate transformation. It holds $|x_0, y_0| \ll 1$ with an appropriate transformation ($m = 1e - 6$ for example). Then, the terms higher than second order are numerically insignificant and can be ignored. (4.27) can thus be simplified as

$$b_6x_0^2 + b_9x_0y_0 + b_{10}x_0 + b_{13}y_0^2 + b_{14}y_0 + b_{15} = 0 \,. \tag{4.28}$$

It turns out to be rather easy to solve x_0 and y_0 from two (4.28)-alike equations. That is, eliminating x_0 (y_0) leads to a fourth order polynomial of y_0 (x_0). Our numerical simulation shows that, (4.27) and (4.28) deliver almost the same real solutions of x_0 and y_0 while (4.27) obtains many complex solutions which are certainly nonsense.

4.2.5 Optimal geometric constraints

We know from last two subsection that any two constraints are able to calculate f and α by given x_0 and y_0; as well, any two constraints are able to calculate x_0 and y_0 by fixing f and α. As one fundamental matrix provides three constraints (4.16) – (4.18), n fundamental matrices obtain *3n* constraints, of which *2n* are independent. Solving simultaneously all the constraints may be computationally inefficient, but also geometrically unfavorable. Some constraints may be appropriate to compute specific internal parameters, while others are less favorable. For example, the epipolar geometry which is close to the degenerate cases will produce false fundamental matrix, and they should be degraded in auto-calibration. Therefore, it is reasonable and even necessary to select the constraints which are geometrically appropriate to compute the internal parameters. This can be accomplished by using the technique of error propagation analysis, as described as follows.

The partial derivatives of a constraint $C(f, \alpha, x_0, y_0)$, which is a function of the internal parameters, are performed as

$$dC(f, \alpha, x_0, y_0) = e_f df^2 + e_\alpha d\alpha^2 + e_x dx_0 + e_y dy_0 \tag{4.29}$$

where

$$\begin{aligned} e_f &= \frac{\partial C(f, \alpha, x_0, y_0)}{\partial f^2}, \qquad e_\alpha = \frac{\partial C(f, \alpha, x_0, y_0)}{\partial \alpha^2} \\ e_x &= \frac{\partial C(f, \alpha, x_0, y_0)}{\partial x_0}, \qquad e_y = \frac{\partial C(f, \alpha, x_0, y_0)}{\partial y_0} \end{aligned}. \tag{4.30}$$

e_f, e_α, e_x and e_y are the functions of the internal parameters as well. Their absolute magnitudes indicate the numerical impact of erroneous estimates f^2, α^2, x_0 and y_0, respectively. While it is hard to be proved rigorously, the numerical simulation shows the general rules that

    (1) for the Constraint I, e_x and e_y are often quite small while e_f and e_α are significant. This indicates that the Constraint I is robust to the deviations of x_0 and y_0 but sensitive to the changes of f^2 and α^2; and

    (2) in contrast, the Constraints II and III are sensitive to the changes of x_0 and y_0 but not to the changes of f^2 and α^2.

Therefore, the Constraint I should be used to calculate f and α, while the Constraints II and III are preferred to compute x_0 and y_0. These two rules coincide with the approximation in Section 4.2.3 where it is suggested the reduced Constraint I should be used to calculate f and α in the first recursion.

Consequently, we need to analyze the error propagations of x_0 and y_0 to the Constraints I, and the error propagations of f^2 and α^2 to the Constraints II and III. The mathematical process of error propagation is detailed as follows.

Error propagations in the Constraint I

Given erroneous x_0 and y_0, the coefficients of the Constraint I should be normalized to avoid the impact of scale factor. The normalization of the constraints I (4.26) is performed as

$$\begin{aligned} \mathrm{c} &= (a_1, \dots, a_6)^T \\ a_i &\triangleq \frac{a_i}{\|\mathrm{c}\|}, \qquad i = 1, 2, \dots, 6 \end{aligned} \tag{4.31}$$

where the normalized coefficients are still denoted as a_i without ambiguity. $\|\cdot\|$ is the norm which can be taken as Euclidean one:

$$\|c\| = \|(a_1, \ldots, a_6)^T\| = \sqrt{\sum_{i=1}^{6} a_i^2} \, . \tag{4.32}$$

The partial derivatives of the normalized a_i ($i = 1, 2, \ldots, 6$) with respective to x_0 and y_0 are

$$e_{a_i} = e_x^i dx_0 + e_y^i dy_0 \tag{4.33}$$

where

$$e_x^i = \frac{\partial a_i}{\partial x_0}, \qquad e_y^i = \frac{\partial a_i}{\partial y_0} \, . \tag{4.34}$$

Then

$$\frac{e_{a_i}}{x_0 y_0} = \frac{e_x^i}{y_0} \frac{dx_0}{x_0} + \frac{e_y^i}{x_0} \frac{dy_0}{y_0} \tag{4.35}$$

$$\left(\frac{1}{x_0 y_0}\right)^2 e_{a_i}^2 = \left(\frac{e_x^i}{y_0}\right)^2 \left(\frac{dx_0}{x_0}\right)^2 + \left(\frac{e_y^i}{x_0}\right)^2 \left(\frac{dy_0}{y_0}\right)^2 \, . \tag{4.36}$$

As dx_0 and dy_0 are unknown, it is assumed that $|dx_0/x_0| \approx |dy_0/y_0|$. By further Neglecting the unknown constant $(x_0 y_0)^{-2}$, it obtains

$$e_{a_i}^2 \cong \left(\frac{e_x^i}{y_0}\right)^2 + \left(\frac{e_y^i}{x_0}\right)^2 \, . \tag{4.37}$$

For the first recursion without any prior estimate of x_0 and y_0, (4.37) is replaced by

$$e_{a_i}^2 \cong \left[\left(e_x^i\right)^2 + \left(e_y^i\right)^2\right]\big|_{x_0=y_0=0} \, . \tag{4.38}$$

Then the total error propagation of the erroneous x_0 and y_0 to the Constraint I C_1, denoted by e_{C1}, is

$$e_{C1} = \sqrt{\sum_{i=1}^{6} e_{a_i}^2} \, . \tag{4.39}$$

Error propagations in the Constraints II and III

Analogously, with given erroneous f^2 and α^2, the normalization of the coefficients is performed on the Constraint II (the Constraint III as well) of the form (4.28):

$$C = \left(b_6, b_9, b_{10}, b_{13,} b_{14}, b_{15}\right)^T$$

$$\|c\| = \sqrt{\sum_i b_i^2}, \ \ b_i \triangleq b_i/\|c\|, \ i = 6, 9, 10, 13, 14, 15 \tag{4.40}$$

The partial derivatives of the normalized b_i ($i = 6, 9, 10, 13, 14, 15$) with respective to f^2 and α^2 are

$$e_{b_i} = e_f^i df^2 + e_\alpha^i d\alpha^2 \tag{4.41}$$

where

$$e_f^i = \frac{\partial a_i}{\partial f^2}, \qquad e_\alpha^i = \frac{\partial a_i}{\partial \alpha^2}. \tag{4.42}$$

Analogous to (4.35) – (4.39), we have

$$\frac{e_{b_i}}{f^2 \alpha^2} = \frac{e_f^i}{\alpha^2} \frac{df^2}{f^2} + \frac{e_\alpha^i}{f^2} \frac{d\alpha^2}{\alpha^2} \tag{4.43}$$

$$\left(\frac{1}{f^2 \alpha^2}\right)^2 e_{b_i}^2 = \left(\frac{e_f^i}{\alpha^2}\right)^2 \left(\frac{df^2}{f^2}\right)^2 + \left(\frac{e_\alpha^i}{f^2}\right)^2 \left(\frac{d\alpha^2}{\alpha^2}\right)^2. \tag{4.44}$$

Assuming $|df^2/f^2| \approx |d\alpha^2/\alpha^2|$ and neglecting the factor $(f^2 \alpha^2)^{-2}$, it obtains

$$e_{b_i}^2 \cong \left(e_f^i/\alpha^2\right)^2 + \left(e_\alpha^i/f^2\right)^2 \tag{4.45}$$

The error propagations of the erroneous f^2 and α^2 to the Constraint II C_2 (and to the Constraint III C_3 as well), denoted by e_{C2} (e_{C3}), is

$$e_{C2} = \sqrt{\Sigma_i e_{b_i}^2}, \; i = 6, 9, 10, 13, 14, 15. \tag{4.46}$$

Optimal constraints

Appropriate constraints can be picked using the results of error propagations. Any two Constraints I, whose error propagations of given x_0 and y_0 are denoted by $e_{C1,1}^2$ and $e_{C1,2}^2$, result in a fourth-order univariate polynomial of f^2 and a sixth-order polynomial of α^2. The polynomial of f^2 and that of α^2 are both *weighted* as $\left(e_{C1,1}^2 \cdot e_{C1,2}^2\right)^{-1}$. Then, all the polynomials of f^2 (and those of α^2) can be ordered by the weights. The polynomials of three top weights are selected as *optimal* constraints to compute f^2 (and α^2). There are reasons for selecting the *three* top-weight polynomials. First, while the polynomial of the highest weight usually delivers optimal solution, this is not theoretically guaranteed. Second, the error propagation analyses include the approximate conditions: $|dx_0/x_0| \approx |dy_0/y_0|$ and $|df^2/f^2| \approx |d\alpha^2/\alpha^2|$. This may result in that the polynomial of the highest weight may not necessarily be the polynomial which has the minimum error propagations. Third, it is somehow inspired by the fact that there are three polynomials of f^2 derived from three views.

Similar principle is applied to select the three constraints of top weights to calculate the principal point by using (4.40) – (4.46). The only difference lies in using either the Constraint II or the Constraint III of a single fundamental matrix. It is mainly due to the fact that two of the three constraints (4.16) – (4.18) of a fundamental matrix are independent. While (4.16) has been used to estimate focal length and aspect ratio, either (4.17) or (4.18) can be adopted to calculate the principal point. Thus for each fundamental matrix, (4.17) or (4.18) which has smaller error propagation is picked using the strategy (4.40) – (4.46). Then, the three constraints of top weights are selected among the n constraints of the n fundamental matrices.

The selection of optimal constraints is able to significantly reduce computation. This selection strategy permits that each internal parameter can be solved from three polynomials of top weights. Without this strategy otherwise, $3n(3n-1)/2$ polynomials from n fundamental matrices need to be solved for each internal parameter.

Unique optimal solution

Certainly, not all solutions derived from the three optimal constraints are reasonable. The reasonable solutions must be real and satisfy

$$f > 0, \quad \alpha > 0, \quad |x_0| \leq \frac{m_t \tilde{u}}{2}, \quad |y_0| \leq \frac{m_t \tilde{v}}{2} \tag{4.47}$$

More practical constraints, such as $^1/_n < \alpha < n$ ($n = 4$ for example), can also be adopted.

Various reasonable solutions may remain after the check (4.47). The common criterion of minimal mean square error (MMSE) is adopted to obtain a unique optimal solution. Particularly, the reasonable solutions of f are denoted by $\{f_i\}_i$, and the univariate polynomials of f are indicated by $\{P_n(f)\}_n$ (there are $n(n\text{-}1)/2$ univariate polynomials derived from n fundamental matrices). Then, the unique optimal solution f^* should satisfy

$$f^* = \min_i \sum_n P_n^2(f_i) . \tag{4.48}$$

The criteria similar to (4.48) are performed to obtain the unique optimal solutions of α, x_0 and y_0.

Convergent criterion

Assume the calibration are $\{f_{l-1}, \alpha_{l-1}, x_{0l-1}, y_{0l-1}\}$ and $\{f_l, \alpha_l, x_{0l}, y_{0l}\}$ at the $l-1$-th and l-th recursion, respectively. A common convergent criterion is given as

$$\left|\frac{f_l - f_{l-1}}{f_l}\right| < 10^{-3}, \left|\frac{\alpha_l - \alpha_{l-1}}{\alpha_l}\right| < 10^{-3},$$
$$\left|\frac{x_{0l} - x_{0l-1}}{x_{0l}}\right| < 10^{-3}, \left|\frac{y_{0l} - y_{0l-1}}{y_{0l}}\right| < 10^{-3} \tag{4.49}$$

$$l > \mathrm{L} \tag{4.50}$$

where L indicates the maximum recursive step. The recursive procedure is stopped if either (4.49) or (4.50) is met.

Briefly, the recursion contains two main steps. The unique estimates of f_l and α_l are obtained using x_{0l-1}, y_{0l-1}, all the Constraints I of the form (4.26) (or (4.25) in the first recursion), the selection of optimal constraints and the MMSE criterion. Then, the unique estimates of x_{0l} and y_{0l} are obtained using f_l, α_l, the Constraints II and III of the form (4.28), the selection of optimal constraints and the MMSE criterion. The recursion proceeds until convergence.

4.2.6 Nonlinear optimization

Undoubtedly, the results of the recursive procedure are sub-optimal. In order to take advantage of the whole multi-view geometry, the nonlinear optimization is recommended for the final refinement with the recursive results being used as initial values. The optimization is performed on all the 3*N constraints of the N fundamental matrices.

The Levenberg–Marquardt algorithm is adopted in our method. The initial value of the damping factor λ can be set as 10^{-3} as usual. This nonlinear optimization runs very fast since there are only four unknown internal parameters. The readers are referred to such as Hartley & Zisserman (2003) and Madsen et al. (2004) for more materials on nonlinear optimization.

4.2.7 Summaries of auto-calibration method

The auto-calibration method is insofar completed. It contains a coordinate transformation, the recursive procedure and nonlinear optimization. The inputs include the image correspondences of pixel coordinates (and known skew parameter), image resolution, the max iteration of the recursive procedure, and the max iteration of the nonlinear optimization (Levenberg–Marquardt algorithm); the output is the calibration matrix. The flow chart of our method is depicted in Fig. 4.1.

As this auto-calibration method is built on the base of the fundamental matrix and the constraints (4.2) and (4.3), the accurate computation of the fundamental matrix becomes thus vital in this work. The normalized 8-point algorithem is adopted, which was firstly presented in Longuet-Higgins (1981) and later refined via a normalization strategy by Hartley (1997). Although it is sub-optimal, this algorithm is fast, accurate and obtaining a unique fundamental matrix from epipolar geometry. The algebraic minimization and the Gold-Standard methods can be used if more accuracy is desired (Hartley & Zisserman, 2003).

4.2.8 Two-view calibration

As a second result of the auto-calibration method, it presents a new idea to compute focal length from two views with the known aspect ratio but not necessarily the principal point. The approximation of the Constraint I, i.e. equation (4.25), is capable to calculate f when α is known a priori (in fact $\alpha = 1$ for many CCD cameras). Four solutions at most can be derived from the 4th-order polynomial (4.25), while the (unique or multiple) positive real solutions are sensible only.

The role of m is particularly significant in the two-view calibration. As will be demonstrated in Section 4.3, different m deliver quite different focal length calibrations, and appropriate m which depends on the epipolar geometry should be selected.

Compared to the previous methods (Stewénius et al., 2005; Sturm et al., 2005; Li, 2008), our method has significant advantages in simplicity and flexibility: it is analytical and does not require the known principal point. It is interesting to note that the method of Sturm et al. (2005) utilized a quadratic equation which assumes $\alpha = 1$ and known (zero) principal point. Although this quadratic equation appears quite similar to (4.25), they are remarkably different. First, (4.25) is derived from the constraint (4.16) by using the approximation (4.22), which is much weaker than the assumption of known principal point used in Sturm's method. Second, Sturm's method can be considered, just numerically, as a special case of our method with $m = 1$. However, $m = 1$ is certainly not a good choice in many cases and it may obtain very poor calibration.

4.3 Experiments: N=2 views

Focal length calibration from two views is experimented in this section, while the auto-calibration from N≥3 views is investigated in the next section.

4.3.1 Test datasets

Simulation datasets

The virtual camera used in all simulation experiments is depicted as follows:

Focal length: $f = 2000$;

Aspect ratio: $\alpha = 1$;
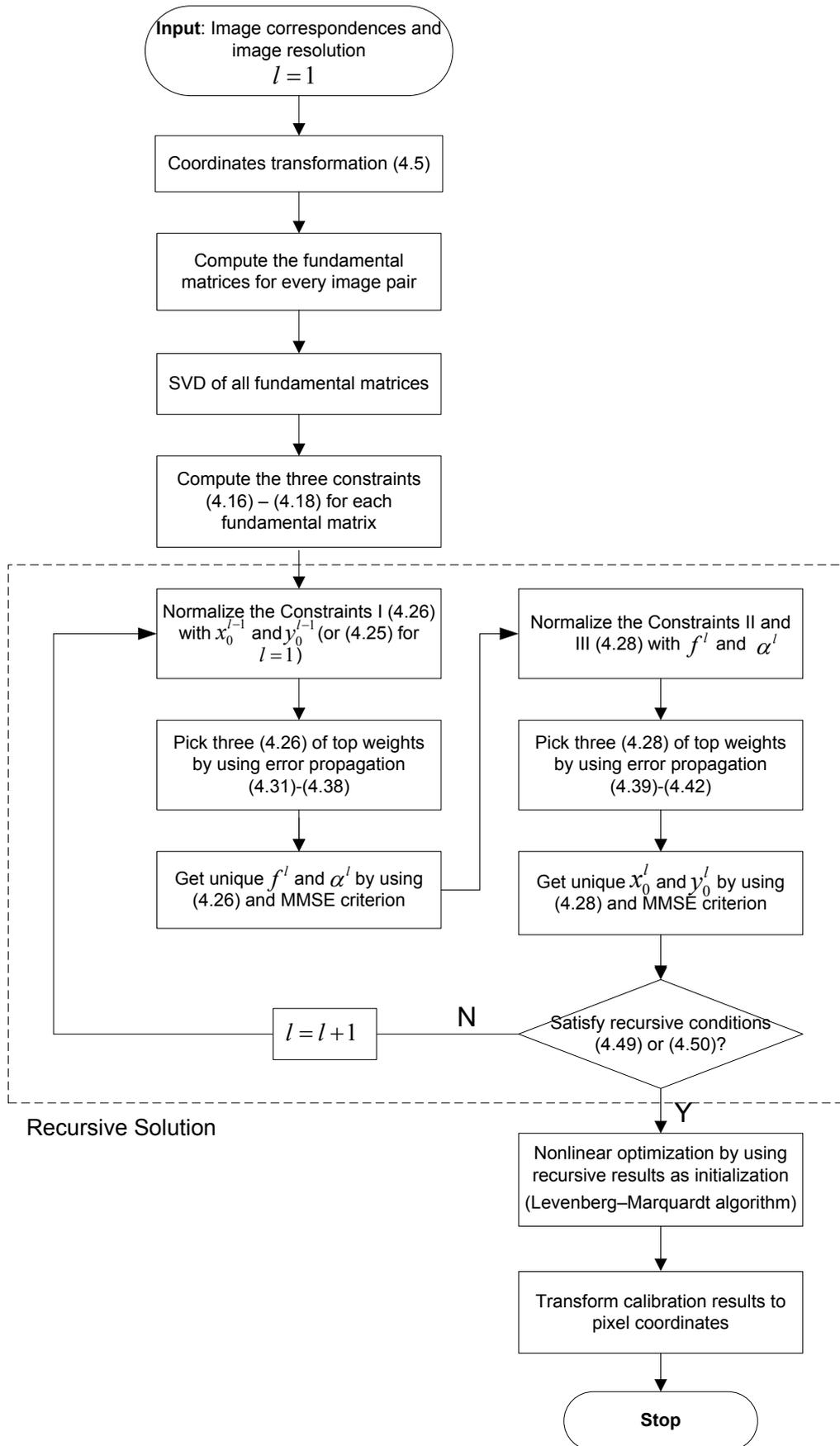
Skew parameter: 0;

Fig. 4.1 The flow chart of our camera auto-calibration method.

Castle

Fountain

Castel Vecchio

Piazza Erbe

Fig. 4.2 Practical test datasets for the focal length calibration from two views (from top to bottom: Castle, Fountain, Castel Vecchio and Piazza Erbe).

Image resolution: 1400×1400; and

Principal point: varied.

The extrinsic parameters of the camera at three different poses are

$$P1: X_1 = \{-3000, 2000, 7370\}, R_1 = \begin{bmatrix} -0.866 & 0 & -0.500 \\ 0 & 1 & 0 \\ 0.500 & 0 & -0.866 \end{bmatrix};$$

$$P2: X_2 = \{0, 0, 9000\}, R_2 = \begin{bmatrix} 1 & 0 & 0 \\ 0 & -0.985 & -0.174 \\ 0 & 0.174 & 0.985 \end{bmatrix}; \text{ and}$$

$$P3: X_3 = \{3000, 1000, 7370\}, R_3 = \begin{bmatrix} 0.940 & 0 & 0.342 \\ 0 & 1 & 0 \\ -0.342 & 0 & -0.940 \end{bmatrix}.$$

In each image pair there are around 100 corresponding points imaged from a 3D scene.

Practical datasets

Four practical image pairs, named as 'Castle', 'Fountain', 'Castel Vecchio' and 'Piazza Erbe', are used, as demonstrated in Fig. 4.2. The image resolutions are $3072 \times 2048, 3072 \times 2048, 1024 \times 768$ and 1024×768, respectively. The aspect ratio is $\alpha = 1$ and the skew parameter is zero. These images are taken from Fusiello et al. (2004) and Strecha et al. (2008).

4.3.2 With known principal point

Our method and the methods by Sturm et al. (2005) and Li (2008) are tested in the case of known principal point, by using the three stereo views of the simulation datasets: $P1\_P2$, $P1\_P3$ and $P2\_P3$. Without losing generality it assumes zero principal point shift, i.e., $u_0 = v_0 = 0$. The interval of kernel-voting is set as $[1500, 2500]$ for the method of Li (2008), and $m = 10^{-6}$ is adopted in our method. The noise of image measurements increases from 0.1 to 1 pixel. The experiments are performed 100 times for every noise level. The mean absolute errors of focal length calibration, denoted by Δf, are computed as

$$\Delta f = \frac{1}{N} \sum_{n=1}^{N} |f_n - f| \tag{4.51}$$

where $N = 100$, $\{f_n\}$ are the calculation results and f is the true focal length.

It is demonstrated in Fig. 4.3 how Δf varies with the noise levels. It is found from those results that, while Δf obtained by all the three methods increases gradually with the noise levels, Li's method obtains inferior results and more sensitive to the noise. The errors of Li's method grow considerably with the noise levels and reach up to over 100 pixels for one pixel's noise. Moreover, the methods of ours and Sturm et al. (2005), which are entirely analytical, are much faster than Li's method. Our method with $m = 10^{-6}$ performs quite similarly to Sturm's method which takes $m = 1$. It indicates that the coordinate transformation (or m) has little influence on the focal length calibration when the principal point is given. However, the role of m is critical when the principal point is unknown, as shown in next subsections.

4.3.3 With unknown principal point

The unknown principal point shift of the virtual camera is set as $u_0 = v_0 = 50$ and the noise is 0.1 pixel; m is chosen as those in (4.7). The variations of Δf with m in the three stereos ($P1\_P2$, $P1\_P3$ and $P2\_P3$) are illustrated in Fig. 4.4. It is easily found from Fig. 4.4 that the focal length calibration

varies substantially with m in every stereo-view. The minimum calibration errors with the appropriate selection of m are 15.5, 5.1, and 28.4 for the three stereos, respectively; while the maximum errors are 117.4, 51.1 and 424.3, respectively. The maximum errors are even over ten times worse than the minimum errors. These results show clearly the significant role of coordinate transformation in focal length calibration.

Moreover, $m = 10^{-1}$ and $m = 10^{-2}$ obtain almost the same calibration result in the three stereos; $m = 10^{-5}$ and $m = 10^{-6}$ get quite similar errors as well. The impact of a certain range of m seems very close. To further investigate the impact of m, the principal point u_0 and v_0 are shifted randomly over $[-100, 100]$ for 100 times. We use $m = 10^{-5}, 10^{-6}$ for stereo $P1\_P2$, $m = 10^{-1}, 10^{-2}$ for stereo $P1\_P3$, and $m = 10^{-5}, 10^{-6}$ for stereo $P2\_P3$. The differences by using different m in each stereo are illustrated in Fig. 4.5. Obviously, the differences are rarely over 0.5 pixels in all the cases. Therefore, these experiments show that a certain range of m act similarly in two-view calibration. This is a main reason why the suggested m in (4.7) is a discrete set.

It is a critical issue whether or not the appropriate selection of m is dependent on the principal point shift. If so, the *optimal* selection of m becomes nonsense since the principal point is unknown a priori. Fortunately, it can be shown that the optimal selection of m is independent of the principal point.

To show this, the principal point u_0 and v_0 are shifted randomly over $[-100, 100]$ for 100 times. We count the number when each m in (4.7) obtains minimum absolute errors of focal length. Particularly, it is performed as follows:

- for each random principal point shift, the m_j ($j = 1, 2, \ldots, 6$) in (4.7) are applied into (4.25) and the absolute errors of focal length, denoted by e_j ($j = 1, 2, \ldots, 6$), are obtained; and
- count the number c_j ($j = 1, 2, \ldots, 6$) when m_j obtains minimum absolute error (denoted by e^*). To neglect slight numerical difference, other m_i which satisfy $e_i - e^* < \delta$ are considered as obtaining minimum error as well. It is set $\delta = 0.001 * f$ in these experiments.

The numbers c_j ($j = 1, 2, \ldots, 6$) are illustrated in Fig. 4.6. It is found from these results that $m = 10^{-4}$, $m = 10^{-5}$ and $m = 10^{-6}$ obtain minimum errors for all the random principal point shifts in the stereo $P1\_P2$; $m = 10^{-1}$ and $m = 10^{-2}$ in the stereo $P1\_P3$, and $m = 10^{-5}$ and $m = 10^{-6}$ in the stereo $P2\_P3$, always get minimum errors of focal length. There are quite a few times for other m to get the minimum errors when the random principal point shift is close to zero; the impact of m is not significant on focal length calibration in these cases, as mentioned in Section 4.3.2.

In a word, these experiments show evidently that m plays a critical role in focal length calibration when the principal point is unknown; the choice of m is independent of the principal point shift, i.e., the optimal m depends on the essential matrix rather the fundamental matrix of epipolar geometry. Techniques are desired to automatically select the optimal m.

4.3.4 Practical tests

Our analytical method as well as that in Li (2008) is tested using the practical datasets. The corresponding points are extracted using the open VLFeat library by Vedaldi & Fulkerson (2010). The normalized 8-point algorithm, together with the RANSAC (RANdom SAmple Consensus) technique eliminating the outliers, is used to compute the fundamental matrix. Both $m = 0.1$ and $m = 10^{-6}$ are used in our method; the interval of kernel-voting for Li (2008) is set as $[-300 + f, f + 300]$ where f is the true focal length.

The results of focal length calibration are depicted in Table 4.1. It is found from these results that our method achieves very good accuracy. The error is even smaller than 4 pixels in the data 'Castel Vecchio' with $m = 10^{-6}$. $m = 10^{-6}$ performs better than $m = 10^{-1}$ in all the datasets except 'Castel'. The calibration error is about 45 pixels in the 'Castle' and it is much worse than others. This may be caused by that many feature points lie in the plane of the wall of the 'Castle', while a single plane is known as a degenerate case to compute the fundamental matrix.
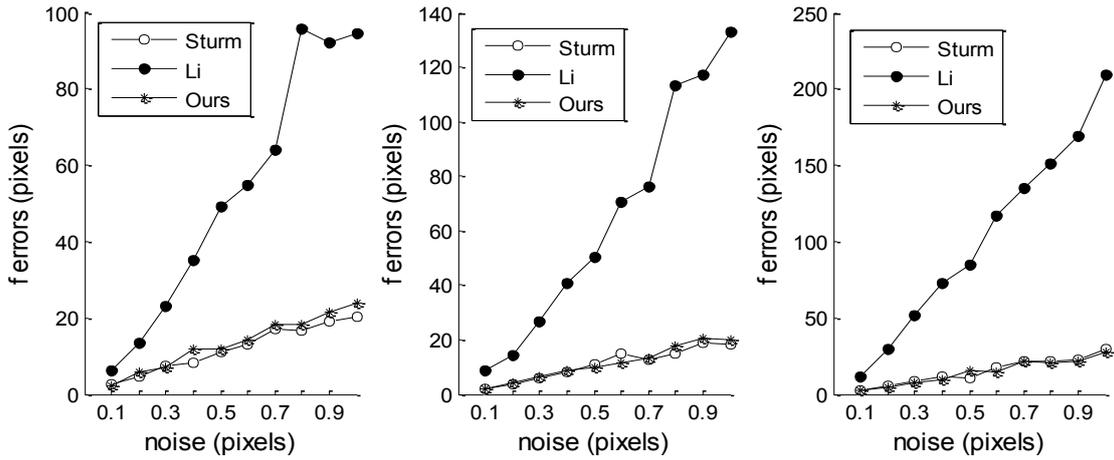
Fig. 4.3 The errors of the focal length calibration vary with different noise levels, with known principal point. The stereo views are $P1\_P2$ (left), $P1\_P3$ (middle) and $P2\_P3$ (right).
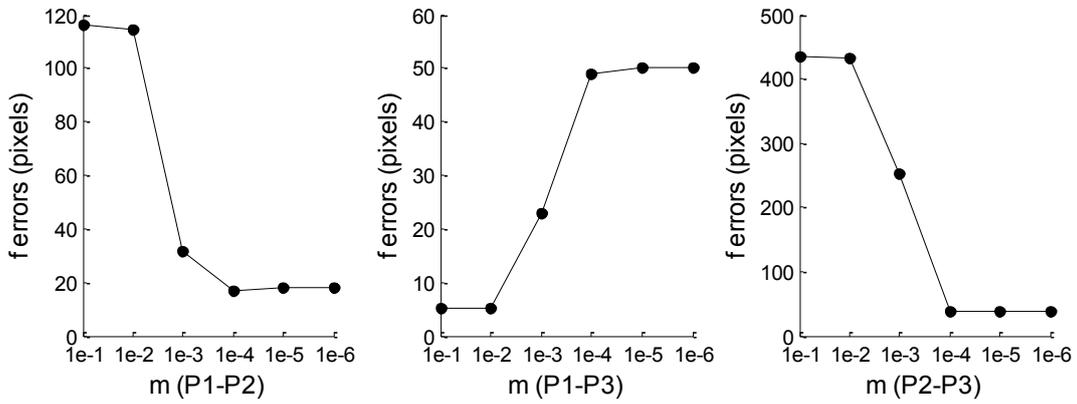

Fig. 4.4 The errors of the focal length calibration vary with different m in different pair views, with an unknown principal point.
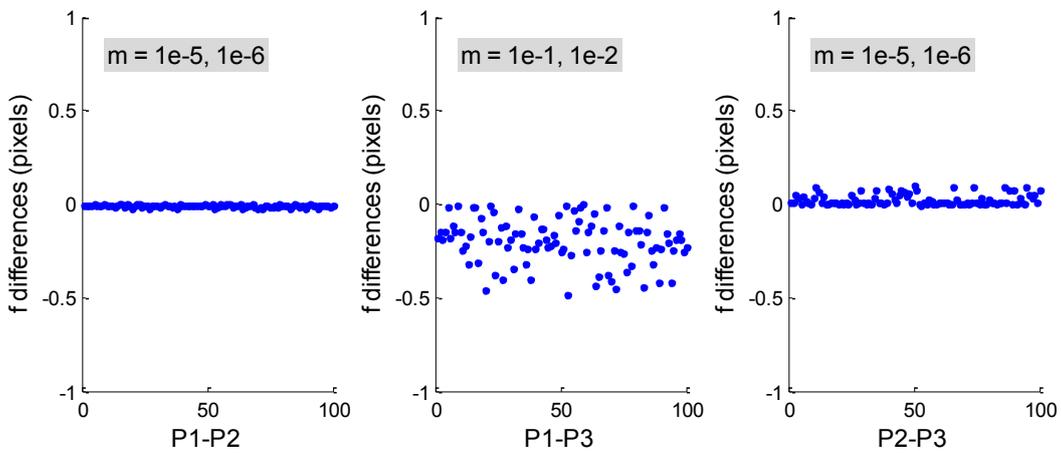

Fig. 4.5 The differences of focal length calibration vary with 100 random unknown principal points, when m is chosen as two different values.
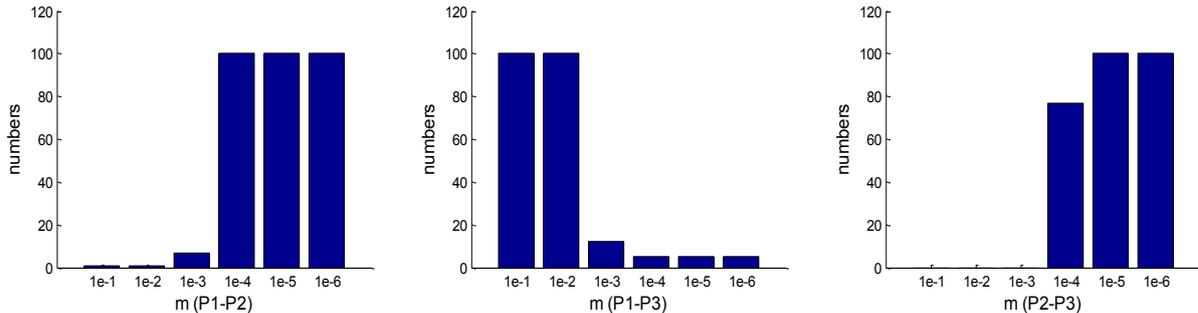
Fig. 4.6 The numbers different m obtain the minimum absolute errors of focal length calibration with 100 random unknown principal points.

Table 4.1 Practical test results of the two-view focal length calibration (unit: pixels).

Datasets	True f	Li (2008)	Ours with $m = 10^{-1}$	Ours with $m = 10^{-6}$
Castle	2761.82	2819	2805.83	2716.44
Fountain	2761.82	2691	2738.66	2770.75
Castel Vecchio	1341	1399	1328.43	1337.03
Piazza Erbe	1341	1410	1353.35	1345.35

Moreover, our method outperforms Li's method in all the cases in Table 4.1. This may be due to two reasons. The first reason is the impact of noise. It is known that the precision of SIFT features (Lowe, 2004) is around sub-pixel, while Li's method seems quite sensitive to the noise as illustrated in Fig. 4.3. The second one might be that, Li's method utilizes the two constraints in (4.2), while our work suggest that using the constraint (4.16) only can be more effective.

4.4 Experiments: N≥3 views

4.4.1 Test datasets

Simulation datasets

The simulation datasets of three views in Section 4.3.1 are used to test the auto-calibration method.

Practical datasets

We employ two practical image sets, 'Castel Vecchio' and 'Piazza Erbe', which contain four and three images, respectively. They are demonstrated in Fig. 4.7.

All the experiments are implemented in MATLAB, in one PC with 32-bit Windows Seven system, CPU 2.5GHz and 3GB RAM.

Castel Vecchio_1   Castel Vecchio_2

Castel Vecchio_3   Castel Vecchio_4

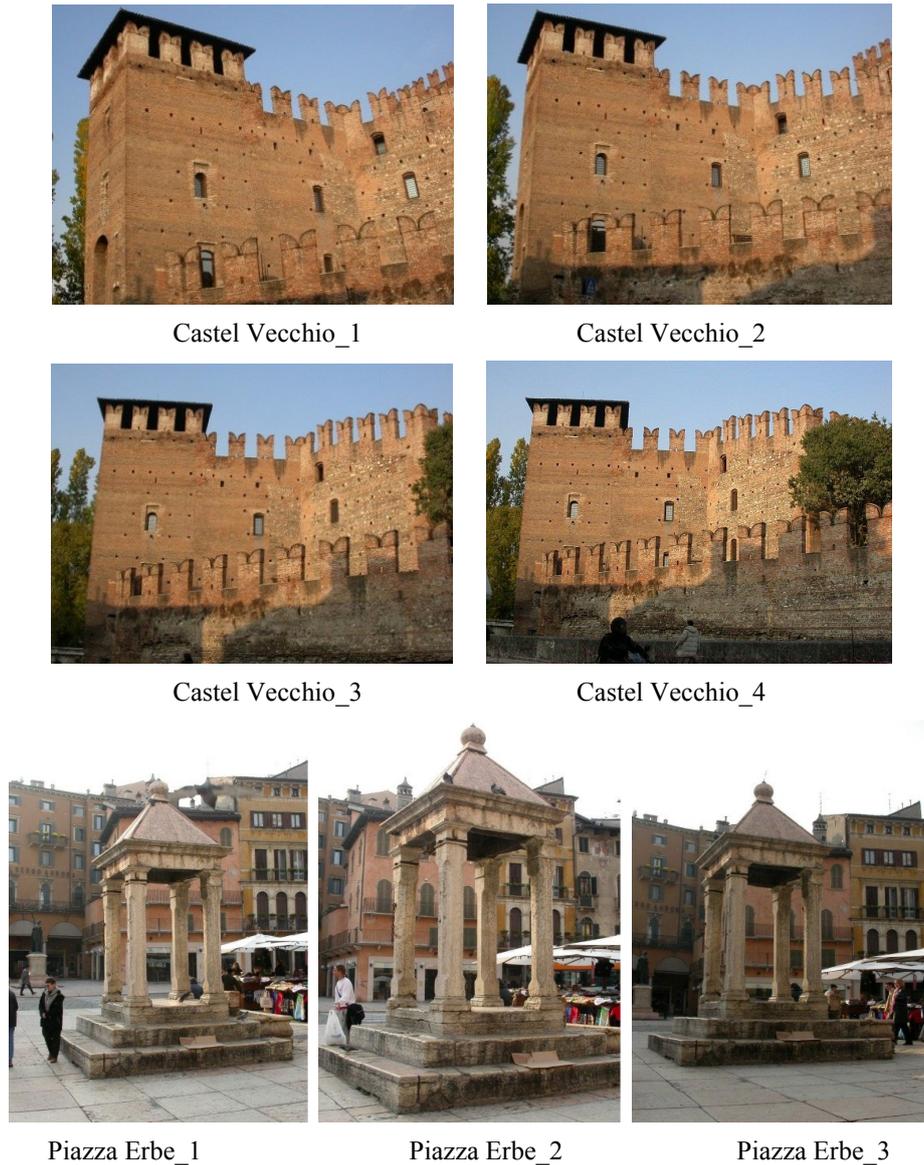Piazza Erbe_1   Piazza Erbe_2   Piazza Erbe_3

Fig. 4.7 Practical test datasets for the camera auto-calibration: Castel Vecchio (4 images) and Piazza Erbe (3 images).
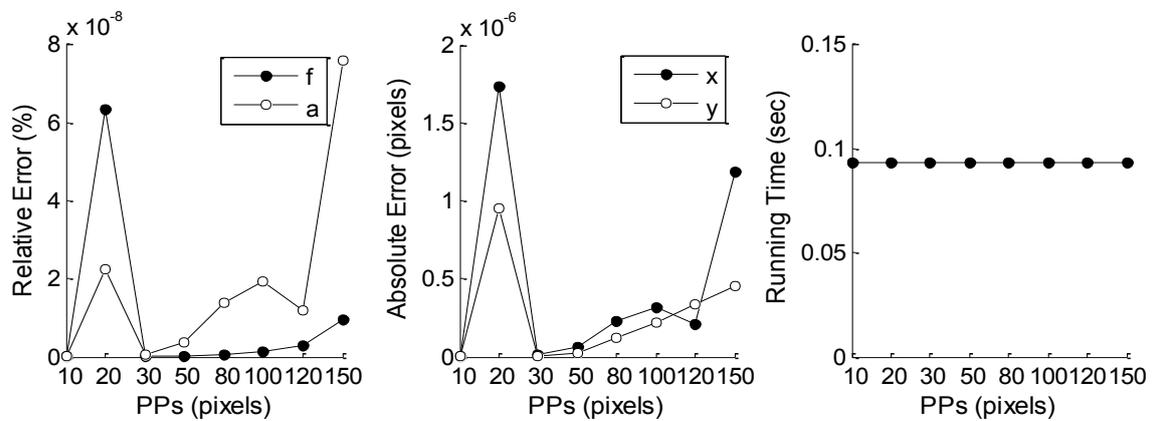

Fig. 4.8 Auto-calibration evaluation with respect to different principal point shifts, by given the perfect fundamental matrices.
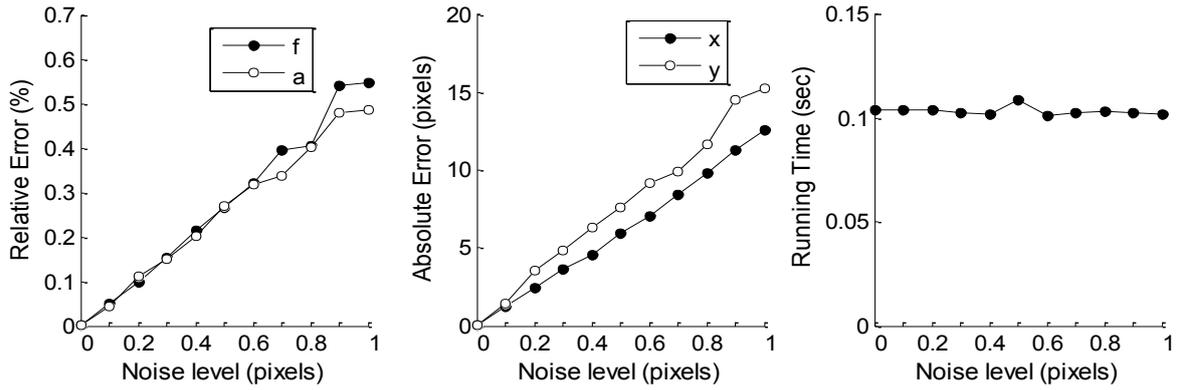
Fig. 4.9 Auto-calibration evaluation with respect to different noise levels.
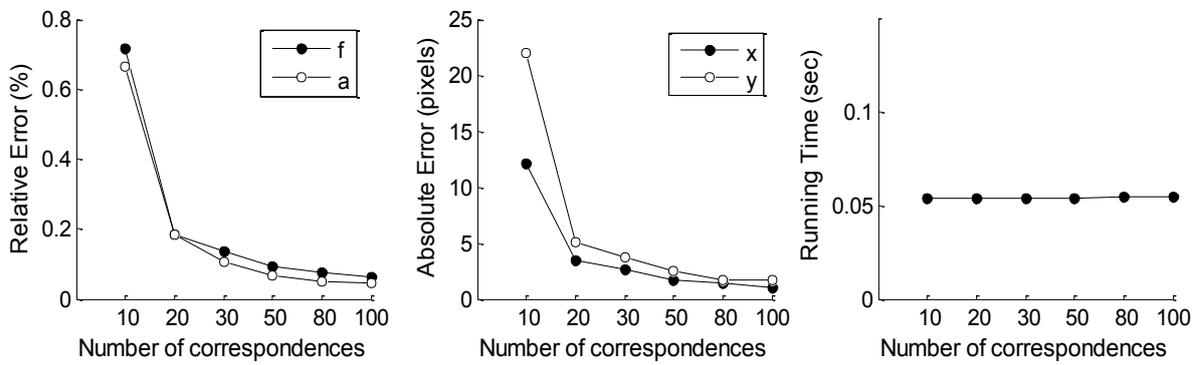

Fig. 4.10 Auto-calibration evaluation with respect to different numbers of image correspondences.
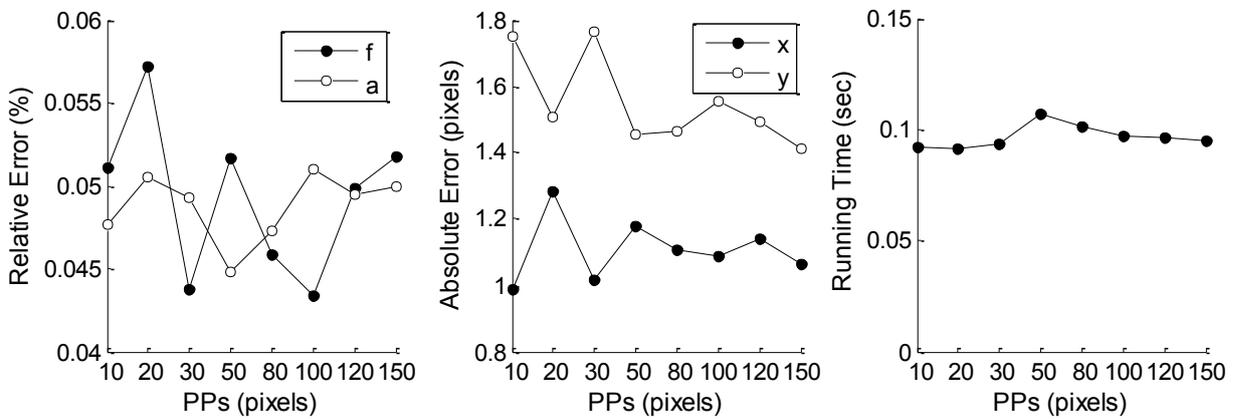

Fig. 4.11 Auto-calibration evaluation with respect to different principal point shifts.

4.4.2 Simulation tests

The simulation evaluations are performed with respect to different noise levels, different principal point shifts and different numbers of image correspondences. Each simulation experiment runs 100 times. The accuracy of focal length and aspect ratio is quantified by the relative error (%) and the principal point is evaluated by the absolute error (unit: pixels).

Given perfect fundamental matrices

We first evaluate the performance of our calibration method when all fundamental matrices are perfectly given. The results are illustrated in Fig. 4.8, with respect to the principal point varying from 0 to 150 pixels. "PPs" in Fig. 4.8 stands for the principal point shift. The relative errors of f and α are impressively smaller than 10^{-7}%, and the absolute errors of the principal point are less than 2×10^{-6} pixels. The running time is around 0.1 seconds in all the cases. The performance of auto-calibration is clearly independent of the amount of the principal point shift.

Noise effect

The computation of the fundamental matrix is impacted by the noise, whose effect on our auto-calibration method is evaluated here. There are about 100 correspondences for each image and the real principal point shift is 50 pixels. We illustrate in Fig. 4.9 the calibration results with respect to the noise levels which increasing from 0.0 to 1.0 pixel.

It is observed from Fig. 4.9 that the relative errors of f and α and the absolute errors of the principal point increase *linearly* with the noise levels. For the noise smaller than 0.2 pixels, the relative errors of f and α are smaller than 0.1% and the absolute error of the principal point is smaller than 5 pixels; and they are around 0.5% and 14 pixels when the noise is one pixel. The linear increase of errors show our method is quite robust to the noise. The running time is around 0.1 second, independent of the noise level.

Number of image correspondences

The impact of the number of the image correspondences, which increase from 10 to 100, is illustrated in Fig. 4.10. The noise level is 0.1 pixels and the real principal point shift is 50 pixels.

It is found from Fig. 4.10 that the calibration errors decrease substantially with the increasing number of image correspondences. When there are around 100 image correspondences, the relative errors of f and α are around 0.07% and the absolute error of the principal point are 2 pixels. The running time is about 0.06 second in all the cases.

Effect of principal point shifts

Here we again demonstrate in Fig. 4.11 the calibration results with respect to different principal point shifts, with the noise of 0.1 pixels and around 100 correspondent points. The principal points are shifted from 10 to 150 pixels. It is seen from Fig. 4.11 that the relative errors of f and α are around 0.05% and the absolute error of the principal point is smaller than 2 pixels. It is obvious that the calibration performance is entirely independent of the magnitude of the principal point shift.

Table 4.2 Practical test results of the camera auto-calibration from N≥3 views.

Datasets	Methods	f (pixels)	α	u_0(pixels)	v_0(pixels)	Time (Sec)
Castel Vecchio	True values	1341	1.00	521	382	---
	Fusiello (2004)	1328	0.942	582	328	1200
	Ours (1, 2, 3)	1363.84	0.960	534.43	438.54	0.25
	Ours (1, 2, 3, 4)	1355.98	0.974	528.70	419.09	0.33
Piazza Erbe	True values	1341	1.00	521	382	---
	Fusiello (2004)	1368	0.942	450	402	1920
	Ours (1, 2, 3)	1352.26	1.043	509.68	364.72	0.58

4.4.3 Practical tests

The test results using the practical images in Fig. 4.7 are demonstrated in Table 4.2, where the calibration results of Fusiello et al. (2004) are depicted as well (the source codes of Fusiello et al. (2004) are unfortunately unavailable right now). The first three images and all the four images of 'Castel Vecchio' are tested separately.

For the first three images of 'Castel Vecchio', the errors of f, u_0 and v_0 are 22.84, 13.43 and 56.54 pixels, respectively. They are decreased to be 14.98, 7.70 and 37.09 pixels respectively, when all the four images are used. The aspect ratio α is refined from 0.96 to 0.97 as well. Obviously, more images are being used, more accurate the calibration is. On the other hand, the v_0 calibration is much worse than u_0. It is mainly caused by the close directions of the v image axes of the four images. It can be found in Fig. 4.7 that the v axes of all the 'Castel Vecchio' images are close to the vertical direction. Small difference in rotation angles may lead to poor calibration. Compared to the results in Fusiello et al. (2004), our method obtains comparable f and v_0, and much better α and u_0. For the 'Piazza Erbe' images, our method achieves rather good accuracy. The errors of f, u_0 and v_0 are 11.26, 11.32 and 17.28 pixels, respectively; the errors of α is 0.043. These results are better than those obtained by Fusiello et al. (2004). Another main advantage of our method is the fast speed. Generally, our method runs less than one second which is less than one thousandth of the time costed by Fusiello et al. (2004).

4.5 Discussions

Although the promising results have been demonstrated in Section 4.3 and Section 4.4, our calibration method is not mature yet. There are critical issues to be addressed for the calibration from two views and N≥3 views, as discussed as follows.

4.5.1 Focal length calibration from two views

First, how to select automatically the optimal m? The critical role of m has been shown in calibrating focal length when the principal point is unknown. It has been shown as well that the optimal selection of m is independent of the principal point shift. Therefore, a technique is desired to automatically select an appropriate m for focal length calibration.

Second, how many solutions of focal length can be derived from (4.25)? Theoretically, at most four reasonable solutions of f (real and positive) can be obtained from a 4th-oder polynomial (4.25) with given α. It might obtain none, single or multiple reasonable solutions. In our simulation experiments when the principal point u_0 and v_0 vary randomly over $[-100, 100]$ (unit: pixels) and there are around 80 image correspondences, we always get a single reasonable solution. Nevertheless, more theoretical investigations are beneficial on the number of solutions (the work on degenerate configuration of two-view calibration was studied in Sturm et al. (2005)).

Third, it is suggested that (4.17) and (4.18) should be ignored in focal length calibration. These two formulae occasionally obtain comparable but mostly get much worse results than (4.16). Their inadequacy is mainly caused by that they include the terms m_{12} and n_{12} which can be influenced severely by the unknown principal point x_0 and y_0. For m_{12}, the sign of the 'constant' term $(u_{31} + u_{11}x_0 + u_{21}y_0)(u_{32} + u_{12}x_0 + u_{22}y_0)$ can be opposite to the sign of $u_{31}u_{32}$ after approximation. Changing the sign of the constant terms in a polynomial can seriously corrupt the roots. (4.17) and (4.18) are thus unfavorable for focal length calibration due to the considerable influence of unknown principal point on m_{12} and n_{12}. On the other hand, as the 'constant' term $(u_{31} + u_{11}x_0 + u_{21}y_0)^2$ in m_{11} always keeps as non-negative as u_{31}^2 after approximation, m_{11} (m_{22}, n_{11} and n_{22} as well) is numerically less impacted by the unknown principal point. Equation (4.16), which includes terms m_{11},

m_{22}, n_{11} and n_{22} but not m_{12} or n_{12}, should thus be preferred to calibrate focal length from two views when principal point is unknown.

4.5.2 Auto-calibration from N≥3 views

First, how to select m in auto-calibration? While the optimal selection of m is vital in two-view calibration, its significance can be less considerable in the auto-calibration from N≥3 views. Unlike two-view calibration, there are more than one (4.25)-alike equations being used in auto-calibration. The error of focal length, if significant in the first recursion, can be gradually reduced in the subsequent recursive procedure. Most importantly, the approximation (4.28) requires essentially selecting small m, for example $m = 10^{-6}$ which works quite well in the experiments. Nevertheless, it is worth further exploring the impact of m on auto-calibration.

Second, the selection of optimal geometric constraints in Section 4.2.5 should be a mandatory step in our auto-calibration method. The selection has two main advantages. First, it reduces the cost of computation. Without this selection strategy, 3N(3N-1)/2 polynomials from N fundamental matrices need to be solved for each internal parameter. Second, it helps the stability of auto-calibration since it can disregard the poor solution from inadequate epipolar geometry. For the fundamental matrices which are acquired from the cases close to the degenerate configurations (for example, pure camera translation), the significance of their constraints (4.16) – (4.18) can be degraded by the error propagation technique and the weighting strategy. The inadequate geometry can thus be filtered in the recursive procedure. Nevertheless, this selection strategy may be further refined.

Third, the error propagation technique in Section 4.2.5 is adopted to address a problem: to estimate the impact of erroneous coefficients on the solutions of an algebraic polynomial. We presented a solution which appears quite adequate in auto-calibration. There may be other more efficient methods for this problem.

Fourth, our auto-calibration method is basically using the Kruppa equations which may be not the sufficient conditions of auto-calibration (Hartley & Zisserman, 2003). The modulus constraint may need to be incorporated into our present method.

4.6 Concluding remarks

A new method is proposed to address the challenging problem of camera auto-calibration in geometric computer vision. This method contains three main steps: a coordinate transformation, recursive procedure and nonlinear optimization. A new idea of the focal length calibration from two views without the knowledge of the principal point is proposed as well.

The three formulae (4.16) – (4.18) which equal the two independent constraints of an essential matrix in (4.2) are derived. They are of vital importance for establishing the recursive procedure. Their significance may be found in other applications. Although both the techniques of focal length calibration and the auto-calibration are not mature yet, the promising results have been demonstrated in both simulation and practical tests. The potential refinements are discussed in Section 4.5.

5 Summary

> *"I know nothing except the fact of my ignorance."*
>
> —— Socrates (470 BC – 399 BC).

5.1 Contributions

This work starts with emphasizing the common mathematical fundamentals of photogrammetry and geometric computer vision, i.e., both the collinearity equations in photogrammetry and the projection equation in geometric computer vision can be derived from the mathematical central projection. It reviews the development of the camera calibration techniques in photogrammetry and geometric computer vision, with emphases on their commons and distinctions.

This work studies the camera self-calibration in photogrammetry and computer vision, largely from a mathematical viewpoint as well as together with the physical and practical considerations. There are several contributions in this work.

First, it is pointed out that photogrammetric self-calibration (or building self-calibration models) can – to a large extent – be considered as a *function approximation* problem in mathematics. The unknown function of distortion can be approximated by a linear combination of specific mathematical basis functions. This is the most significant theoretical contribution in this work. Particularly,

- it provides a solid mathematical foundation for many conventional self-calibration models, such as those by Ebner (1976), Grün (1978) and El-Hakim & Faig (1977);
- it introduces a theoretical base, on which we are able to discuss the theoretical advantages and disadvantages of different mathematical self-calibration models. This is a very important rule for selecting appropriate models in practice;
- it leads directly to building the Legendre self-calibration models by using algebraic polynomials as the basis functions, and to developing the Fourier self-calibration models by using the bivariate Fourier series;
- its significance is shown as well in the correlation analyses of the Brown self-calibration model in close range photogrammetry; and
- it offers a synthetic view on the self-calibration models in both aerial and close range photogrammetry. The mathematical self-calibration models, which are originated for aerial applications, can be useful in close range camera calibration due to their approximation nature.

Second, the Legendre and the Fourier self-calibration models are developed on the base of the approximation principle. There are important notes on these mathematical self-calibration models:

- Among the algebraic polynomials, the Legendre polynomials should be preferred to construct self-calibration models since they obtain *optimal* approximation in the least-squares sense. The Legendre self-calibration model can be considered as a superior generalization of the Ebner's and the Grün's polynomial models, to which the Legendre models of second and fourth orders should be preferred, respectively. This is confirmed in the practical tests as well;
- from a theoretical viewpoint, the Fourier series should be the *optimal* basis functions to build photogrammetric self-calibration model due to their perfect theoretical charateristics. The advantages of the Fourier self-calibration model over the polynomial models lie in that they

are more theoretically rigorous, usually need fewer APs and obtain more reliable distortion calibration. The Fourier model should be preferred in in-situ airborne camera calibration; and

- both the Legendre and the Fourier self-calibration models are orthogonal, rigorous, generic, flexible and effective. A number of empirical tests show that both models are capable to calibrate the distortion of the frame-format airborne cameras of large-, medium- and small-formats, mounted in single- and multi-head systems (including the DMC, DMC II, UltraCamX, UltraCamXp, DigiCAM cameras and so on).

Third, it is shown in close range photogrammetry that high correlations between the principal point and the decentering distortion parameters are inherent in the Brown self-calibration model due to the polynomial nature of the model. These high correlations are an essential characteristic of camera orientation (three IO parameters Δx_0, Δy_0 and Δf, and three exterior rotation angles ω, φ and κ), independent of block geometry. It is further shown that, although it is highly correlated with the decentering distortion parameters, the principal point can be reliably and precisely located in a self-calibration under appropriate image configurations. A refined model of in-plane distortion is proposed, which helps to reduce the correlation with the focal length and improve the calibration of it. Moreover, the advantages and disadvantages of the pysical and the mathematical self-calibration models are discussed. The combined "Radial + Legendre" and "Radial + Fourier" models are recommended in many calibration pratices due to their high flexibility and effectiveness.

Fourth, a new method is presented to address the challenging problem of camera auto-calibration in geometric computer vision. It requires only the image correspondences and zero skew parameter. This method includes a coordinate transformation, a recursive procedure and a nonlinear optimization. In the recursion, it firstly estimates the focal length and aspect ratio and then calculates the principal point. The nonlinear optimization, with the recursive results being used as initial values, is performed via the Levenberg–Marquardt algorithm. This method can be very efficient to obtain a unique calibration.

Fifth, a new idea is proposed to calibrate focal length from two views without the knowledge of the principal point, by given the aspect ratio and image correspondences (and zero skew). With an appropriate coordinate transformation which plays a key role, this analytical method is able to calibrate focal length regardless of unknown principal point.

5.2 Discussions

5.2.1 Photogrammetric self-calibration models

Camera calibration is always a central work in photogrammetry. Developing appropriate self-calibration models is vital in calibration activities and many other applications in photogrammetry and remote sensing.

Self-calibration model is essentially a mathematical representation of distortion. There are two general modeling approaches, i.e., physical and mathematical modeling, as mentioned in Section 2.1. The physical modeling uses specific functions to model the empirical knowledge of distortion. The mathematical modeling presumes that the exact knowledge on distortion is unavailable or the exact modeling is difficult; it thus applies the abstract principle of function approximation to approximate the unknown distortion function. The advantages of disadvantages of these two modeling approaches are described in Table 3.8.

It should be noted that, although the mathematical self-calibration models do 'merely' approximate the distortion, this does not mean that these approximate models are less accurate than the exact physical models. The performance of the physical models is limited by our (perhaps imperfect) empirical knowledge on distortion. Distortions may vary with different cameras and they may not be represented and compensated by a specific physical model. Another usual nuisance of the physical models is that

they may need to make a good balance between the exact modeling and reducing correlations. In contrast, the mathematical models are independent on distortion sources. Their efficiency is theoretically guaranteed and they are able to address very complicated distortion. The Legendre and the Fourier self-calibration models are able to get arbitrary accuracy of calibration by choosing sufficiently high degree. Therefore, the mathematical models of appropriate degree are factually able to obtain comparable or even better calibration than the physical models. The combined models, such as the "Radial + Legendre" and "Radial + Fourier" models in Section 2.4, may exploit the advantages of both the physical and mathematical models.

The comparisons between the Legendre and the Fourier self-calibration models are noteworthy. While the advantages of the Fourier model have been shown over the Legendre model, it was not intended to indicate that the Fourier model is superior. First, the Fourier model usually but not always needs fewer APs for calibration. Rigorously speaking, it is circumstance-dependent which model needs fewer APs. Mathematically, it depends on whether the distortion function is approximated more efficient by the algebraic polynomials or by the Fourier series. If polynomials are more suitable, then the Legendre model needs fewer APs; otherwise, the Fourier model is more efficient. Second, it is true on the one hand that the Fourier model is preferable in the in-situ airborne camera calibration due to its theoretical advantages (see Section 2.3 and Section 3.4); on the other hand, our experiences show that the Legendre model occasionally gets better performance in the blocks with few GCPs. Therefore, both the Legendre and the Fourier self-calibration models will find their significance in camera calibration.

5.2.2 Photogrammetry and geometric computer vision

It has been well recognized that photogrammetry and geometric computer vision are two closely neighboring disciplines. They have many similar tasks and goals such as calibration, orientation and reconstruction. Lots of work share their interest in both photogrammetry and computer vision, such as relative orientation (Philip, 1996; Nistér, 2004), the spatial resection of single image or the so-called PnP problem (Masry, 1981; Lepetit et al., 2009), point feature detection (Förstner & Gülch, 1986; Lowe, 2004) and bundle adjustment (Triggs et al., 2000). It should be acknowledged that much work was originally studied in photogrammetry while later advanced significantly in computer vision. This encourages the inter-communications between these two disciplines (Hartley & Mundy, 1993; Förstner, 2002, 2009).

Although much remarkable progress has been made, the relationship between photogrammetry and geometric computer vision seems still quite remote. The exchange difficulty may be due to several facts. First, the traditions, philosophies and applications of the two disciplines are distinctive. For photogrammetry which was originated in surveying and mapping, accuracy is the primary goal and most photogrammetric work are post-processing. For lots of real-time vision work, on the other hand, accuracy is defined by applications and the processing speed becomes a critical issue (meanwhile it is aware of that more and more photogrammetric work become involved in the real-time applications). Second, the language is an obstacle. Quit different languages are used in these two fields. One has to spend time in learning another language before understanding a foreign work. Third but not least, while geometry remains as one of the major concerns in photogrammetry, the main trend in computer vision has been moved from geometry to learning and recognition (see the programs of the three top computer vision conferences (CVPR, ECCV and ICCV) in the recent years, and the timeline of most active topics in computer vision as described in Szeliski (2011)).

While by no means aiming at an exhaustive study on the relationship between photogrammetry and geometric computer vision, it is attempted to make discussions from a mathematical viewpoint. As shown in the first chapter that the mathematical fundamentals of photogrammetry and geometric computer vision can be both derived from the central projection. The collinearity equations in photogrammetry are the *Cartesian* representation of the central projection in *Euclidean geometry*, while the projection equation in computer vision is the *homogeneous* representation of the central

projection in *projective geometry*. Consequently, many distinctions appear in the analytical methods of photogrammetry and geometric computer vision.

- Due to the nonlinearity of the collinearity equations, many analytical techniques in photogrammetry are nonlinear and iterative. In contrast, the linearity of the projection equation permits the liner matrix operations in vision techniques and this suffices the real-time applications.
- The Cartesian representation in photogrammetry enables exploiting many classical techniques of statistical inference, such as error estimation and statistical test. The homogeneous representation in computer vision is capable to take the advantages of the linear algebra, while the statistical inference in projective geometry was recently studied in Förstner (2005).
- Good initial values are often desired in the iterative photogrammetric techniques. The nonlinear optimization, usually using bundle adjustment, can achieve very high accuracy by given good initial values. This is also well acknowledged in vision society. Many vision techniques are benefited from the linearity of the camera matrix and do not suffer such nuisance of initial values (if they are). They can handle quite complex matters. The output of the vision techniques can well serve as the initialization for the photogrammetric techniques.
- All the parameters in the collinearity equations are physically interpretable, but those in the camera matrix are not. Consequently, the collinearity equations may have advantages in the applications of multi-sensor integration (for example a camera incorporated with a GPS/INS system). This is particularly true in aerial photogrammetry where the precise observations of GPS/INS systems serve as very good initial values of the camera EO parameters. On the other hand, projective geometry can be very powerful and convenient in the cases where camera is the only sensor available or camera is incorporated with low-precision navigation sensors. For example, focal length calibration from two views can be only fulfilled using projective geometry.

To summarize, we would like to emphasize that, (1) from a mathematical viewpoint, photogrammetry and geometric computer vision are two different representations and solutions of the camera geometry. In a way, photogrammetry is an art of analysis and statistics, while geometric computer vision is an art of algebra; (2) from an engineering viewpoint, the techniques of photogrammetry and geometric computer vision provide two powerful and efficient alternatives to address the challenges in practice. Both have their advantages and disadvantages, depending on the applications; (3) the accuracy, speed and others should not be the labels used to distinguish the techniques of photogrammetry and geometric computer vision; both their techniques can obtain high accuracy with a fast speed in certain applications; and (4) it is expected that the researchers and students in photogrammetry should learn the basic concepts and techniques of geometric computer vision, and hopefully vice versa.

5.3 Outlooks

There are works to be continued in the following years.

First, self-calibration models in photogrammetry. The self-calibration models should follow and fit the development of camera manufacturing techniques. The mathematical self-calibration models, particularly the Legendre and the Fourier models, will find their significance in the next years since they are rigorous and independent of distortion sources. Extensive tests are appreciated to demonstrate the advantages and disadvantages of these two models, and to enrich the practical experiences on applying different self-calibration APs. The combination of the mathematical APs and the physical APs should be always kept in consideration, in order to maintain precise calibration as well as to avoid overparameterization and high correlations.

Second, camera auto-calibration from N≥3 views and the focal length calibration from two-view in geometric computer vision. We present a new method to solve the auto-calibration problem and

propose a new problem to calibrate the focal length from two views without any knowledge on the principal point. Although there remain a few unsolved problems as discussed in Section 4.5, our methods show very promising potential to ultimately solve these challenging problems. The effects will be devoted in future refinements.

Third, geometry and image understanding. A common goal of photogrammetry in a broad sense and computer vision is getting information from images. This thesis studies the geometry issues in photogrammetry and computer vision. One has to recognize that the geometry is generally mature and moderately difficult, relative to image understanding and recognition which are still much challenging. It is very interesting to incorporate the successful achievements in geometry into other broader applications.

Finally, this thesis study would like to be ended with a quotation from the American computer scientist Alan Curtis Kay (1940 –):

"The best way to predict the future is to invent it."

Appendices

Appendix A: Traditional self-calibration models

The self-calibration model proposed by Brown (1976).

$$\Delta x = a_1 x + a_2 y + a_3 xy + a_4 y^2 + a_5 x^2 y + a_6 xy^2 + a_7 x^2 y^2$$
$$+\frac{x}{f}[a_{13}(x^2 - y^2) + a_{14}x^2y^2 + a_{15}(x^4 - y^4)]$$
$$+x[a_{16}(x^2 + y^2)^2 + a_{17}(x^2 + y^2)^4 + a_{18}(x^2 + y^2)^6] + a_{19} + a_{21}\,x/f$$

$$\Delta y = a_8 xy + a_9 x^2 + a_{10} x^2 y + a_{11} xy^2 + a_{12} x^2 y^2$$
$$+\frac{y}{f}[a_{13}(x^2 - y^2) + a_{14}x^2y^2 + a_{15}(x^4 - y^4)]$$
$$+y[a_{16}(x^2 + y^2)^2 + a_{17}(x^2 + y^2)^4 + a_{18}(x^2 + y^2)^6] + a_{20} + a_{21}\,y/f$$

The polynomial self-calibration model proposed by Ebner (1976).

$$\Delta x = a_1 x + a_2 y - a_3 2k + a_4 xy + a_5 l + a_7 xl + a_9 yk + a_{11} kl$$
$$\Delta y = -a_1 y + a_2 x + a_3 xy - a_4 2l + a_6 k + a_8 yk + a_{10} xl + a_{12} kl$$

with

$$k = x^2 - \frac{2}{3}b^2 \text{ and } l = y^2 - \frac{2}{3}b^2$$

$b = 0.4L$ where L is the length of the square image format.

The polynomial self-calibration model proposed by Grün (1978).

$$\Delta x = a_1 x + a_2 y + a_3 xy + a_4 l - a_6 \frac{10}{7}k + a_7 xp + a_8 yk + a_9 xl + a_{10} yq + a_{15} r + a_{16} xyp$$
$$+a_{17} kl + a_{18} xyq + a_{19} s + a_{25} yr + a_{26} xlp + a_{27} ykq + a_{28} xs + a_{33} lr + a_{34} xypq$$
$$+a_{35} ks + a_{39} yqr + a_{40} xps + a_{43} rs$$

$$\Delta y = -a_1 y + a_2 x + a_3 \frac{10}{7}l + a_5 k - a_6 xy + a_{11} xp + a_{12} yk + a_{13} xl + a_{14} yq + a_{20} r + a_{21} xyp$$
$$+a_{22} kl + a_{23} xyq + a_{24} s + a_{29} yr + a_{30} xlp + a_{31} ykq + a_{32} xs + a_{36} lr + a_{37} xypq$$
$$+a_{38} ks + a_{41} yqr + a_{42} xps + a_{44} rs$$

With

$$k = x^2 - \frac{1}{2}b^2, l = y^2 - \frac{1}{2}b^2, p = x^2 - \frac{17}{20}b^2, q = y^2 - \frac{17}{20}b^2$$

$$r^2 = x^2\left(x^2 - \frac{31}{28}b^2\right) + \frac{9}{70}b^2 \text{ and } s^2 = y^2\left(y^2 - \frac{31}{28}b^2\right) + \frac{9}{70}b^2$$

where $b = 0.4L$ where L is the length of the square image format.

The self-calibration model of spherical harmonics by El-Hakim & Faig (1977).

$$\Delta x = a_1 x + a_2 y + q \frac{x}{r}$$

$$\Delta x = -a_1 y + a_2 x + q \frac{y}{r}$$

where

$$q = a_3 r \cos \lambda + a_4 r \sin \lambda + a_5 r^2 + a_6 r^2 \cos 2\lambda + a_7 r^2 \sin 2\lambda + a_8 r^3 \cos \lambda +$$
$$+ a_9 r^3 \sin \lambda + a_{10} r^3 \cos 3\lambda + a_{11} r^3 \sin 3\lambda$$
$$r = \sqrt{x^2 + y^2} \ \text{ and } \ \lambda = \tan^{-1} y/x$$

Appendix B: Orthogonal polynomials

Definition B.1 (Orthogonal)

Two functions $f(x)$ and $g(x)$ in $\mathcal{L}^2[a, b]$ are said to be orthogonal over the interval $[a, b]$ with respect to a given continuous and non-negative weight function $\omega(x)$, if

$$\int_a^b f(x)g(x)\,\omega(x)dx = 0 . \tag{A.1}$$

For convenience, the notation of inner product is often used.

$$\langle f \cdot g \rangle = \int_a^b f(x)g(x)\,\omega(x)dx . \tag{A.2}$$

Definition B.2 (Orthogonal polynomial family)

An orthogonal polynomial family is $\{\phi_i(x)\}_{i=0,1,2,\ldots}$ where ϕ_i is of degree i exactly, defined so that

$$\langle \phi_i \cdot \phi_j \rangle = 0, i \neq j . \tag{A.3}$$

Particularly, this family is orthonormal if, in addition to (A.3), they satisfy

$$\langle \phi_i \cdot \phi_i \rangle = 1, i = 0, 1, 2, \ldots . \tag{A.4}$$

B.1 Legendre orthogonal polynomials

If the inner product is defined over the interval and by using the weight function as

$$[a, b] = [-1, 1], \quad \omega(x) = 1 . \tag{A.5}$$

Then we obtain the orthogonal Legendre polynomials. The first few univariate Legendre polynomials follow.

$$L_0(x) = 1$$

$$L_1(x) = x$$

$L_2(x) = (3x^2 - 1)/2$

$L_3(x) = (5x^3 - 3x)/2$

$L_4(x) = (35x^4 - 30x^2 + 3)/8$

$L_5(x) = (63x^5 - 70x^3 + 15x)/8$

$L_6(x) = (231x^6 - 315x^4 + 105x^2 - 5)/16$

B.2 Chebyshev orthogonal polynomials of the first kind

If the inner product is defined over the interval and by using the weight function as

$$[a, b] = [-1,1], \qquad \omega(x) = (1 - x^2)^{-\frac{1}{2}}. \tag{A.6}$$

Then we obtain the Chebyshev orthogonal polynomials of the first kind. The first few first few Chebyshev polynomials of the first kind follow.

$T_0(x) = 1$

$T_1(x) = x$

$T_2(x) = 2x^2 - 1$

$T_3(x) = 4x^3 - 3x$

$T_4(x) = 8x^4 - 8x^2 + 1$

$T_5(x) = 16x^5 - 20x^3 + 5x$

$T_6(x) = 32x^6 - 48x^4 + 18x^2 - 1$

The Chebyshev polynomials of the first kind have a very interesting relation to the cosine series, as given by

$$T_n(x) = \cos n\theta, \qquad \cos \theta = x, \qquad -1 \le x \le 1. \tag{A.7}$$

For more mathematical materials on orthogonal polynomials, the readers are referred to textbooks such as Mason & Handscomb (2003) or Oliver et al. (2010).

Appendix C: In-plane distortion and the skew parameter

Both the shear term B_2 of the in-plane distortion in photogrammetry and the skew parameter of the camera matrix in computer vision are proclaimed to account for the non-orthogonality between two image axes. It can be proved as follows that these two parameters are equal, up to a scale factor.

Proof. For the benefit of simplification, it assumes zero principal point shift $x_0 = y_0 = 0$ and $\alpha = 1$ without losing generality. Denote (the indications of terms follow those in the first chapter)

$$\begin{pmatrix} X' \\ Y' \\ Z' \end{pmatrix} \triangleq R^T \begin{pmatrix} X - X_0 \\ Y - Y_0 \\ Z - Z_0 \end{pmatrix}. \tag{A.8}$$

Then, it is derived from the collinearity equations (1.4) with the shear term B_2 that

$$\begin{aligned} x &= -fX'/Z' + B_2 y \\ y &= -fY'/Z' \end{aligned} \tag{A.9}$$

and it is obtained from the camera matrix (1.10) and the calibration matrix (1.13) that

$$\begin{pmatrix} x \\ y \\ 1 \end{pmatrix} = \begin{pmatrix} f & s & 0 \\ 0 & f & 0 \\ 0 & 0 & 1 \end{pmatrix} \begin{pmatrix} X' \\ Y' \\ Z' \end{pmatrix} = \begin{pmatrix} fX' + sY' \\ fY' \\ Z' \end{pmatrix}. \tag{A.10}$$

Following the scale invariance of the homogeneous coordinates, (A.10) is equivalent to

$$\begin{pmatrix} x \\ y \\ 1 \end{pmatrix} = \begin{pmatrix} fX'/Z' + s\,Y'/Z' \\ fY'/Z' \\ 1 \end{pmatrix} \tag{A.11}$$

and

$$\begin{aligned} x &= fX'/Z' + s\,y/f \\ y &= fY'/Z' \end{aligned}. \tag{A.12}$$

Noticing $-f$ in (A.9) are f in (A.10) (see Section 1.1.1), we have

$$B_2 = s/f. \tag{A.13}$$

Therefore, B_2 and s are the same, up to a positive constant factor f (f of a camera is a constant, whether known or not).

Q.E.D.

Appendix D: Proofs of the theorems

D.1 Proof of the Weierstrass theorem

A constructive proof of the Weierstrass theorem (for a real-valued function) using Bernstein polynomials is outlined here (Mason & Handscomb, 2003). The **Bernstein basis polynomials** of degree n are defined as

$$b_{n,v}(x) = \binom{n}{v} x^v (1-x)^{n-v} \tag{2.53}$$

where $x \in [0,1]$, $v = 0, 1, \ldots, n$, and $\binom{n}{v}$ is a binomial coefficient.

A linear combination of Bernstein basis polynomials

$$B(x) = \sum_{v=0}^{n} \beta_v b_{n,v}(x) \tag{2.54}$$

is called a Bernstein polynomial and β_v are coefficients.

Proof. Without losing generality, let f be a continuous function on the interval $[0,1]$. Consider the Bernstein polynomial

$$B_n(f)(x) = \sum_{v=0}^{n} f\left(\frac{v}{n}\right) b_{n,v}(x) \tag{2.55}$$

Suppose K is a random value distributed as the number of successes in n independent Bernoulli trials with probability x of success on each trial; in other words, K has a binomial distribution with parameters n and x. Then we have the expected value $E(K/n) = x$.

By the weak law of large numbers of probability theory,

$$\lim_{n\to\infty} P\left(\left|\frac{K}{n} - x\right| > \delta\right) = 0 \tag{2.56}$$

for every δ.

Because f, being continuous in a close bounded interval, must be uniformly continuous on that interval, one infers a statement of the form

$$\lim_{n\to\infty} P\left(\left|f\left(\frac{K}{n}\right) - f(x)\right| > \delta\right) = 0 \tag{2.57}$$

uniformly in x. Taking into account that f is bounded (on the given interval) one gets for the expectation

$$\lim_{n\to\infty} E\left(\left|f\left(\frac{K}{n}\right) - f(x)\right| > \delta\right) = 0 \tag{2.58}$$

Note that $E\left(\left|f\left(\frac{K}{n}\right) - f(x)\right|\right) \geq \left|E\left(f\left(\frac{K}{n}\right)\right) - E(f(x))\right| = \left|E\left(f\left(\frac{K}{n}\right)\right) - f(x)\right|$ and $E\left(f\left(\frac{K}{n}\right)\right) = B_n(f)$, then one gets the uniform convergence

$$\lim_{n\to\infty} |B_n(f)(x) - f(x)| = 0 \tag{2.59}$$

Q.E.D.

D.2 Proof of the Fourier theorem

We proof the result under the additional assumptions that f is defined on $[-\pi, \pi]$, f' is piecewise smooth and thus f'' is piecewise continuous. The proof for general cases can be seen in Folland (2009).

Proof. Since f is continuous, it can be represented as

$$f(x) = \frac{a_0}{2} + \sum_{n=1}^{\infty} (a_n \cos nx + b_n \sin nx) \tag{A.21}$$

where a_0, a_n and b_n ($n = 1, 2, ...$) are Fourier coefficients.

To prove the absolute convergence it suffices to show that $|a_n|, |b_n| \leq M/_{n^2}$ for some constant M independent of n. Then

$$\lim_{n \to \infty} \left| \frac{a_0}{2} + \sum_{n=1}^{n} (a_n \cos nx + b_n \sin nx) - f(x) \right| = 0 \tag{A.22}$$

uniformly in x.

Notice

$$
\begin{aligned}
a_n &= \frac{1}{\pi} \int_{-\pi}^{\pi} f(x) \cos nx \, dx = -\frac{1}{n\pi} \int_{-\pi}^{\pi} f'(x) \sin nx \, dx \\
&= \frac{1}{n^2 \pi} [f'(x) \cos nx]_{-\pi}^{\pi} - \frac{1}{n^2 \pi} \int_{-\pi}^{\pi} f''(x) \cos nx \, dx \\
&= \frac{1}{n^2 \pi} [f'(\pi^-) \cos nx - f'(-\pi^+) \cos nx] - \frac{1}{n^2 \pi} \int_{-\pi}^{\pi} f''(x) \cos nx \, dx
\end{aligned}
\tag{A.23}
$$

Since $f'(x)$ and $f''(x)$ are continuous on the close interval $[-\pi, \pi]$, $|f'(x)|$ and $|f''(x)|$ are bounded. Then there exist a constant M satisfying

$$
\begin{aligned}
|f'(\pi^-) \cos nx - f'(-\pi^+) \cos nx| &\leq \frac{M\pi}{2} \\
\left| \int_{-\pi}^{\pi} f''(x) \cos nx \, dx \right| &\leq \frac{M\pi}{2}
\end{aligned}
\tag{A.24}
$$

Then one obtains $|a_n| \leq M/_{n^2}$ and similarly $|b_n| \leq M/_{n^2}$.

Q.E.D.

D.3 Proof of the theorem on the essential matrix

A proof is given in Hartley & Zisserman (2003).

Proof. Given the known calibration matrix, a pair of normalized camera matrices can be formed as $P = [I|0]$ and $P' = [R|t]$. Then the essential matrix of this pair is

$$E = [t]_\times R = SR \tag{A.25}$$

where $S = [t]_\times$ and $[\ ]_\times$ is the matrix representation of the cross product and defined as

$$\left[\begin{pmatrix} a \\ b \\ c \end{pmatrix} \right]_\times = \begin{pmatrix} 0 & -c & b \\ c & 0 & -a \\ -b & a & 0 \end{pmatrix}. \tag{A.26}$$

Denote the matrix

$$W = \begin{pmatrix} 0 & -1 & 0 \\ 1 & 0 & 0 \\ 0 & 0 & 1 \end{pmatrix}, \qquad Z = \begin{pmatrix} 0 & 1 & 0 \\ -1 & 0 & 0 \\ 0 & 0 & 0 \end{pmatrix} \tag{A.27}$$

and it may be verified that W is orthogonal and Z is skew-symmetric.

The 3×3 skew-symmetric matrix S may be written as $S = k U Z U^T$ where U is orthogonal. Noting that, up to sign, $Z = \mathrm{diag}(1,1,0)W$, then up to scale, $S = U\mathrm{diag}(1,1,0)WU^T$, and $E = SR = U\mathrm{diag}(1,1,0)(WU^T R)$. This is a singular value decomposition of E with two equivalent singular values, as required. Conversely, a matrix with two equivalent singular values may be factored as SR in this way.

To prove (4.2), it is written as $E = USV^T = U\mathrm{diag}(a, b, 0)V^T$ using singular value decomposition and $\det E = 0$. Then

$$2EE^TE - tr(E^TE)E = 2USSSV^T - tr(VSSV^T)USV^T = 0$$
$$2SSS - tr(VSSV^T)S = 2\mathrm{diag}(a^3, b^3, 0) - (a^2 + b^2)\mathrm{diag}(a, b, 0) = 0 \tag{A.28}$$

It is equal to $a = b$ which indicates the singular values are equivalent.

Q.E.D.

Bibliography

The abbreviations of journals and conference proceedings used in bibliography follow.

J. P&RS: ISPRS Journal of Photogrammetry and Remote Sensing.

PE&RS: Photogrammetric Engineering & Remote Sensing.

IAPRS: International Archives of the Photogrammetry, Remote Sensing and Spatial Information Sciences (or formerly International Archives of Photogrammetry and Remote Sensing).

IJCV: International Journal of Computer Vision.

PAMI: IEEE Transactions on Pattern Analysis and Machine Intelligence.

CVPR: Proceedings of IEEE Conference on Computer Vision and Pattern Recognition.

ECCV: Proceedings of European Conference on Computer Vision.

ICCV: Proceedings of International Conference on Computer Vision.

Ackermann, F. (1981). Block adjustment with additional parameters. *Photogrammetria, 36*(3), 217-227.

Ackermann, F. (1994). Practical experience with GPS supported aerial triangulation. *Photogrammetric Record, 14*(84), 860–874.

Agapito, L., Hartley, R., & Hayman.E. (1999). Linear self-calibration of a rotating and zooming camera. *CVPR 1999*, (pp. 15-21).

Atkinson, P. (1993). The effect of spatial resolution on the experimental variogram of airborne MSS imagery. *International Journal of Remote Sensing, 14*(5), 1005-1011.

Bannari, A., Gibson, A., & Morin, D. (1997). The necessity of exterior orientation parameters for the rigorous geometric correction of MEIS-II airborne digital images. *Remote Sensing Reviews, 16*(1-2), 135-156.

Barazzetti, L., Mussio, L., Remondino, F., & Scaioni, M. (2011). Targetless camera calibration. *IAPRS, 38(5/W16)*. 8 pages on CD-ROM.

Barreto, J., & Daniilidis, K. (2005). Fundamental matrix for cameras with radial distortion. *ICCV 2005*, (pp. 625-632).

Berztiss, A. (1964). Least squares fitting of polynomials to irregularly spaced data. *SIAM Review, 6*(3), 203-227.

Blázquez, M., & Colomina, I. (2012). Relative INS/GNSS aerial control in integrated sensor orientation: models and performance. *J. P&RS, 67*, 120-123.

Bougnoux, B. (1998). From projective to euclidean space under any practical situation, a criticism of self-calibration. *ICCV 1998*, (pp. 790-796).

Brown, D. (1956). *The simultaneous determination of the orientation and lens distortion of a photogrammetric camera.* Air Force Missile Test Center Report No. 58-8. Florida: Patrick AFB.

Brown, D. (1964). *An advanced plate reduction for photogrammetric cameras.* Air Force Cambridge Research Laboratories Report No. 64-40. Massachusetts: USA Air Force.

Brown, D. (1966). Decentering distortion of lenses. *Photogrammetric Engineering, 32*(3), 444-462.

Brown, D. (1971). Close-range camera calibration. *Photogrammetric Engineering, 37*(8), 855-866.

Brown, D. (1972). Calibration of close range cameras. *International Archives of Photogrammetry, 19(5).* 26 pages.

Brown, D. (1976). The bundle method – progress and prospects. *International Archives of Photogrammetry, 21(3)*, pp. 1-33.

Brown, D. (1989). A strategy for multi-camera on-the-job self-calibration. *Schriftenreihe 14, Institut für Photogrammetrie der Universität Stuttgart, Festschrift Friedrich Ackermann zum 60. Geburtstag*, (pp. 9-21).

Caprile, B., & Torre, V. (1990). Using vanishing points for camera calibration. *IJCV, 4*(2), 127-140.

Chandraker, M., Agarwal, S., Kriegman, D., & Belongie, S. (2010). Globally optimal algorithms for stratified autocalibration. *IJCV, 90*(2010), 236-254.

Chen, T., Shibasaki, R., & Lin, Z. (2007). A rigorous laboratory calibration method for interior orientation of an airborne linear push-broom camera. *PE&RS, 73*(4), 369-374.

Clarke, T., & Fryer, J. (1998). The development of camera calibration methods and models. *Photogrammetric Record, 16*(91), 51-66.

Clarke, T., Wang, X., & Fryer, J. (1998). The principal point and CCD cameras. *Photogrammetric Record, 16*(92), 293-312.

Conrady, A. (1919). Decentered lens systems. *Monthly Notices of the Royal Astronomial Society, 79*, 384-390.

Cox, D., Little, J., & O'Shea, D. (2004). *Using Algebraic Geometry* (2nd ed.). New York: Springer-Verlag.

Cramer, M. (Ed.). (2009). *Digital Camera Calibration.* EuroSDR official publication No. 55.

Cramer, M. (2010). The DGPF-test on digital airborne camera evaluation – overview and test design. *Photogrammetrie-Fernerkundung-Geoinformation (PFG), 2010*(2), 75-84.

Cramer, M., Grenzdörffer, G., & Honkavaara, E. (2010). In-situ digital airborne camera validation and certification – the future standard? *IAPRS, 38(1).* 6 pages on CD-ROM.

Cramer, M., Kresse, W., Skaloud, J., Haala, N., Nittel, S., & Wallgrün, J. (2012). Data Capture. In W. Kresse, & D. Danko (Eds.), *Springer Handbook of Geographic Information* (pp. 211-301). Berlin: Springer-Verlag.

DGPF project. (2010). *Evaluation on digital airborne camera systems*. Retrieved July 2011, from http://www.ifp.uni-stuttgart.de/dgpf/DKEP-Allg.html

Ebner, H. (1976). Self-calibrating block adjustment. *Bildmessung und Luftbildwesen, 44*(4), 128-139.

El-Hakim, S., & Faig, W. (1977). Compensation of systematic image errors using spherical harmonics. *Proceedings of the American Society of Photogrammetry*, (pp. 492-499). papers from the 1977 Fall Technical Meeting.

Faig, W. (1975). Calibration of close-range photogrammetry systems: mathematical formulation. *PE&RS, 41*(12), 1479-1486.

Faugeras, O. (1993). *Three Dimensional Computer Vision: A Geometric Viewpoint.* Cambridge, MA: MIT Press.

Faugeras, O., Luong, Q., & Maybank, S. (1992). Camera self-calibration: theory and experiments. *ECCV 1992. LNCS 588*, pp. 321-334. Springer-Verlag.

Fitzgibbon, A. (2001). Simultaneous linear estimation of multiple view geometry and lens distortion. *CVPR 2001*, (pp. 18-21).

Folland, G. (2009). *Fourier Analysis and Its Applications.* American Mathematical Society.

Förstner, W. (2002). Computer vision and photogrammetry – mutual questions: geometry, statistics and cognition. *Bildteknik/Image Science, Swedish Society for Photogrammetry and Remote Sensing*, (pp. 151-164).

Förstner, W. (2005). Uncertainty and projective geometry. In E. Corrochano (Ed.), *Handbook of Geometric Computing* (pp. 493-534). Berlin: Springer-Verlag.

Förstner, W. (2009). Computer vision and remote sensing – lessons learned. In D. Fritsch (Ed.), *Photogrammetric Week 2009*, (pp. 241-249).

Förstner, W., & Gülch, E. (1986). A fast operator for detection and precise location of distinct points, corners and centers of circular features. *Proceedings of the ISPRS Workshop on Fast Processing of Photogrammetric Data*, (pp. 281-305).

Fraser, C. (1997). Digital camera self-calibration. *J. P&RS, 52*(4), 149-159.

Fraser, C., & Al-Ajlouni, S. (2006). Zoom-dependent camera calibration in digital close-range photogrammetry. *PE&RS, 72*(9), 1017-1026.

Fraser, C., Shortis, M., & Ganci, G. (1995). Multi-sensor system self-calibration. *Videometrics IV. SPIE 2598*, (pp. 2-18).

Fritsch, D. (1997). Experiences with the airborne three-line camera system DPA. In D. Fritsch (Ed.), *Photogrammetric Week 1997*, (pp. 63-74).

Fryer, J., & Brown, D. (1986). Lens distortion for close-range photogrammetry. *PE&RS, 52*(1), 51-58.

Fryer, J., & Fraser, C. (1986). On the calibration of underwater cameras. *Photogrammetric Record, 12*(67), 73-85.

Fryer, J., Clarke, T., & Chen, J. (1994). Lens distortion for simple C-mount lenses. *IAPRS, 30(5)*, pp. 97-101.

Fusiello, A., Benedetti, A., Farenzena, M., & Busti, A. (2004). Globally convergent autocalibration using interval analysis. *PAMI, 26*(12), 1633-1638.

Geyer, C., & Daniilidis, K. (2002). Paracatadioptric camera calibration. *PAMI, 24*(5), 687-695.

Granshaw, S. (1980). Bundle adjustment methods in engineering photogrammetry. *Photogrammetric Record, 10*(56), 181-207.

Grün, A. (1978). Progress in photogrammetric point determination by compensation of systematic errors and detection of gross errors. *IAPRS, 22(Part 3)*, pp. 113-140.

Habib, A., & Morgan, M. (2005). Stability analysis and geometric calibration of off-the-shelf digital cameras. *PE&RS, 71*(6), 733-741.

Habib, A., Morgan, M., & Lee, Y. (2002). Bundle adjustment with self-calibration using straight lines. *Photogrammetric Record, 17*(100), 635-650.

Hartley, R. (1994). Self-calibration from multiple views with a rotating camera. *ECCV 1994. LNCS 800*, pp. 471-478. Springer-Verlag.

Hartley, R. (1997). In defence of the 8-point algorithm. *PAMI, 19*(6), 580-593.

Hartley, R., & Kang, S. (2007). Parameter-free radial distortion correction with center of distortion estimation. *PAMI, 29*(8), 1309-1321.

Hartley, R., & Mundy, J. (1993). The relationship between photogrammetry and computer vision. *Integrating Photogrammetric Techniques with Scene Analysis and Machine Vision*, *SPIE proceedings vol. 1944*, pp. 92-105.

Hartley, R., & Zisserman, A. (2003). *Multiple View Geometry in Computer Vision* (2nd ed.). Cambridge, UK: Cambridge University Press.

Hartley, R., Agapito, L., Hayman, E., & Reid, I. (1999). Camera calibration and the search for infinity. *ICCV 1999*, (pp. 510-517).

Heipke, C., Jacobsen, K., & Wegmann, H. (Eds.). (2002). *Integarted Sensor Orientation.* European Organization for Experimental Photogrammetrc Research (OEEPE) offical publication No. 43.

Heyden, A., & Astrom, K. (1996). Euclidean reconstruction from constant intrinsic parameters. *Proceedings of the 13th International Conference on Pattern Recognition* , (pp. 339-343).

Honkavaara, E. (2004). Calibration in direct georeferencing: theoretical considerations and practical results. *PE&RS, 63*(8), 1207-1208.

Honkavaara, E., Ahokas, E., Hyyppä, J., Jaakkola, J., Kaartinen, H., Kuittinen, R., . . . Markelin, L. (2006). Geometric test field calibration of digital photogrammetric sensors. *J. P&RS, 60*(6), 387-399.

Horaud, R., & Csurka, G. (1998). Self-calibration and Euclidean reconstruction using motions of a stereo rig. *ICCV 1998*, (pp. 96-103).

Itō, K. (Ed.). (1993). *Encyclopedic Dictionary of Mathematics* (2nd ed.). The MIT Press.

Jacobsen, K. (1982). Attempt at obtaining the best possible accuracy in bundle block adjustment. *Photogrammetria, 37*(6), 219-235.

Jacobsen, K. (2007). Geometric handling of large size digital airborne frame camera images. *International Conference on Optical 3D Measurement Techniques VIII*, (pp. 164-171).

Jacobsen, K. (2011). Geometric property of large format digital camera DMC II 140. *Photogrammetrie-Fernerkundung-Geoinformation (PFG), 2011*(2), 71-79.

Jacobsen, K., Cramer, M., Ladstätter, R., Ressl, C., & Spreckels, V. (2010). DGPF-project: evaluation of digital photogrammetric camera systems – geometric performance. *Photogrammetrie-Fernerkundung-Geoinformation (PFG), 2010*(2), 85-98.

José, L., & Cabrelles, M. (2007). A review and analyses of plumb-line calibration. *Photogrammetric Record, 22*(118), 135-150.

Kenefick, J., Gyer, M., & Harp, B. (1972). Analytical self-calibration. *Ibid, 38*(11), 1117-1126.

Kersten, T., & Haering, S. (1997). Automatic interior orientation of digital aerial images. *PE&RS, 63*(8), 1007-1011.

Kilpelä, E. (1981). Compensation of systematic errors of image and model coordinates. *Photogrammetria, 37*(1), 15-44.

Kilpelä, E., Heikkilä, J., & Inkilä, K. (1981). Compensation of systematicerrors in bundleadjustment. *Photogrammetria, 37*(1), 1-13.

Kim, J., Gurdjos, P., & Kweon, I. (2005). Geometric and algebraic constraints of projected concentric circles and their applications to camera calibration. *PAMI, 27*(4), 637-642.

Knight, J., Zisserman, A., & Reid, I. (2003). Linear auto-calibration for ground plane motion. *CVPR 2003*, (pp. 503-510).

Koornwinder, T. (1975). Two-variable analogues of the classical orthogonal polynomials. In R. Askey (Ed.), *Theory and Application of Special Functions* (pp. 435-495). New York: Academic Press.

Kraus, K. (1997). *Photogrammetry: Advanced Methods and Applications (Volume 2).* Bonn: Ferd Dümmlers Verlag.

Kraus, K. (2007). *Photogrammetry: Geometry from Images and Laser Scans* (2nd ed.). Berlin: Walter de Gruyter.

Kresse, W., Skaloud, J., & Hinsken, L. (2006). Requirements for an orientation and calibration

standard for digital aerial cameras and related sensors. *IAPRS*, *36(1)*. 4 pages on CD-ROM.

Kröpfl, M., Kruck, E., & Gruber, M. (2004). Geometric Calibration of The Digital Large Format Aerial Camera Ultracam. *IAPRS*, *35(1)*, pp. 42-44.

Kukelova, Z., Bujnak, M., & Pajdla, T. (2008). Automatic Generator of Minimal Problem Solvers. *ECCV 2008. LNCS 5304*, pp. 302-315. Springer-Verlag.

Läbe, T., & Förstner, W. (2004). Geometric stability of low-cost digital consumer cameras. *IAPRS*, *35(5)*, pp. 528-535.

Lei, F., & Tiziani, H. (1993). Atmospheric influence on image quality of airborne photographs. *Optical Engineering, 32*(9), 2271-2280.

Lepetit, V., Moreno-Noguer, F., & Fua, P. (2009). An accurate O(n) solution to the PnP problem. *IJCV, 81*(2), 155-166.

Li, H. (2008). A simple solution to the six-point two-view focal-length problem. *ECCV 2008. LNCS 3951*, pp. 200-213. Springer-Verlag.

Liebowitz, D., & Zisserman, A. (1998). Metric rectification for perspective images of planes. *CVPR 1998*, (pp. 482-488).

Liebowitz, D., & Zisserman, A. (1999). Combining scene and auto-calibration constraints. *ICCV 1999*, (pp. 293-300).

Longuet-Higgins, H. (1981). A computer algorithm for reconstructing a scene from two projections. *Nature, 293*, 133-135.

Lowe, D. (2004). Distinctive image features from scale-invariant keypoints. *IJCV, 60*(2), 91-110.

Luhmann, T. (2010). Close range photogrammetry for industrial applications. *J. P&RS, 65*(6), 558-569.

Luhmann, T., Robson, S., Kyle, S., & Harley, S. (2006). *Close Range Photogrammetry: Principles, Techniques and Applications*. Caithness: Whittles Publishing.

Luong, Q., & Faugeras, O. (1996). The fundamental matrix – theory, algorithms, and stability analysis. *IJCV, 17*(1), 43-75.

Luong, Q., & Faugeras, O. (1997). Self-calibration of a moving camera from point correspondences and fundamental matrices. *IJCV, 22*(3), 261-289.

Madsen, K., Nielsen, H., & Tingleff, O. (2004). *Methods for Non-linear Least Squares Problems* (2nd ed.). Technical University of Denmark.

Malis, E., & Cipolla, R. (2002). Camera self-calibration from unknown planar structures enforcing the multiview constraints between collineations. *PAMI, 24*(9), 1268-1272.

Mallon, J., & Whelan, P. (2004). Precise radial un-distortion of images. *Proceedings of the 17th International conference on Pattern Recognition*, (pp. 18-21).

Mason, J., & Handscomb, D. (2003). *Chebyshev Polynomials*. Florida: Chapman & Hall / CRC.

Masry, S. (1981). Digital mapping using entities - a new concept. *PE&RS, 47*(11), 1561-1565.

Maybank, S., & Faugeras, O. (1992). A theory of self-calibration of a moving camera. *IJCV, 8*(2), 123-151.

McGlone, J., Mikhail, E., Bethel, J., & Mullen, R. (Eds.). (2004). *Manual of Photogrammetry*. Maryland: American Society for Photogrammetry and Remote Sensing.

Mikhail, E., Bethel, J., & McGlone, J. (2001). *Introduction to Modern Photogrammetry*. NewYork: John Wiley & Sons, Inc.

Mills, J., Newton, I., & Graham, R. (1996). Aerial photography for survey purposes with a high resolution, small format, digital camera. *Photogrammetric Record, 15*(88), 575-587.

Newby, P. (2012). Photogrammetric terminology: second edition. *Photogrammetric Record, 27*(139), 360-386.

Nistér, D. (2004). An efficient solution to the five-point relative pose problem. *PAMI, 26*(6), 756-770.

Oberst, J., Brinkmann, B., & Giese, B. (2000). Geometric calibraiton of the MICAS ccd sensor on the DS1 (deep space one) spacecraft: laboratory vs. in-flight data analysis. *IAPRS, 33(B1)*, pp. 221-230.

Oliver, F., Lozier, D., Boisvert, R., & Clark, C. (Eds.). (2010). *NIST Handbook of Mathematical Functions*. Cambridge, UK: Cambridge University Press.

Philip, J. (1996). A non-iterative algorithm for determining all essential matrices corresponding to five point pairs. *Photogrammetric Record, 15*(88), 589-599.

Pollefeys, M., & van Gool, L. (1997). A stratified approach to metric self-calibration. *CVPR 1997*, (pp. 407-412).

Pollefeys, M., Koch, R., & van Gool, L. (1998). Self calibration and metric reconstruction in spite of varying and unknown internal camera parameters. *ICCV 1998*, (pp. 90-96).

Rao, C. (2001). *Linear Statistical Inference Its Applications* (2nd ed.). New York: John Wiley & Sons, Inc.

Rao, C., & Toutenburg, H. (1999). *Linear Models: Least Squares and Alternatives* (2nd ed.). New York: Springer-Verlag.

Remondino, F., & Fraser, C. (2006). Digital camera calibration methods: considerations and comparisons. *IAPRS, 36(5)*, pp. 266-272.

Sandau, R. (Ed.). (2010). *Digital Airborne Camera: Introduction and Technology*. Berlin: Springer-Verlag.

Schuster, R., & Braunecker, B. (2000). Calibration of the LH systems ADS40 airborne digital sensor. *IAPRS, 33(1)*, pp. 288-294.

Schut, G. (1979). Selection of additional parameters for the bundle adjustment. *PE&RS, 45*(9), 1243-1252.

Schwarz, K., Chapman, M., Cannon, M., & Gong, P. (1993). An integrated INS/GPS approach to the georeferencing of remotely sensed data. *PE&RS, 59*(11), 1667-1674.

Seidl, K., Richter, K., Knobbe, J., & Maas, H. (2011). Wide field-of-view all-reflective objectives designed for multispectral image acquisition in photogrammetric applications. *SPIE Optical Systems Design 2011 – Optical Complex Systems*, (p. 10 pages).

Skaloud, J., & Legat, K. (2008). Theory and reality of direct georeferencing in national coordinates. *J. P&RS, 63*(2), 272-282.

Skaloud, J., Cramer, M., & Schwarz, K. (1996). Exterior orientation without ground control. *IAPRS, 31(B1)*, pp. 125-130.

Slama, S. (Ed.). (1980). *Manual of Photogrammetry* (4th ed.). Maryland: American Society for Photogrammetry and Remote Sensing.

Stamatopoulos, C., & Fraser, C. (2011). Calibration of long focal length cameras in close range photogrammetry. *Photogrammetric Record, 26*(135), 339-360.

Stein, G. (1995). Accurate internal camera calibration using rotation, with analysis of sources of error. *ICCV 1995*, (pp. 230-236).

Stewénius, H., Nistér, D., Kahl, F., & Schaffalitzky, F. (2005). A minimal solution for relative pose with unknown focal length. *CVPR 2005*, (pp. 789-794).

Strecha, C., von Hansen, W., Van Gool, L., Fua, P., & Thoennessen, U. (2008). On benchmarking camera calibration and multi-view stereo for high resolution imagery. *CVPR 2008*, (pp. 1-8).

Sturm, P., & Maybank, S. (1999). On plane based camera calibration: a general algorithm, singularities, applications. *CVPR 1999*, (pp. 432-437).

Sturm, P., Cheng, Z., Chen, P., & Poo, A. (2005). Focal length calibration from two views: method and analysis of singularcases. *Computer Vision and Image Understanding, 99*(1), 58-95.

Szeliski, R. (2011). *Computer Vision: Algorithms and Applications*. London: Springer-Verlag.

Tang, R., Fritsch, D., Cramer, M., & Schneider, W. (2012). A flexible mathematical method for camera calibration in digital aerial photogrammetry. *PE&RS, 78*(10), 1069-1077.

Telem, G., & Filin, S. (2010). Photogrammetric modeling of underwater environments. *J. P&RS, 66*(5), 433-444.

Triggs, B. (1997). Autocalibration and the absolute quadric. *CVPR 1997*, (pp. 609-614).

Triggs, B. (1998). Autocalibration from planar scenes. *ECCV 1998. LNCS 1406*, pp. 89-105. Springer-Verlag.

Triggs, B., McLauchlan, P., Hartley, R., & Fitzgibbon, A. (2000). Bundle adjustment — a modern synthesis. *Vision Algorithms: Theory and Practice (Proceedings of International Workshop on Vision Algorithms 1999)*, (pp. 153-177).

Vedaldi, A., & Fulkerson, B. (2010). Vlfeat: an open and portable library of computer vision algorithms. *Proceedings of the international conference on Multimedia*, (pp. 1469-1472).

VIM. (2007). *ISO/IEC Guide 99:2007, International vocabulary of metrology -- Basic and general concepts and associated terms (VIM)*. Retrieved September 2012, from http://www.iso.org/iso/iso_catalogue/catalogue_tc/catalogue_detail.htm?csnumber=45324

Wang, J., Cohen, P., & Herniou, M. (1992). Camera calibration with distortion models and accuracy evaluation. *PAMI, 14*(10), 965-980.

Wester-Ebbinghaus, W. (1983). *Einzelstandpunkt-Selbstkalibrierung – ein Beitrag zur Feldkalibrierung von Aufnahmekammern. (Single-Site Self-Calibration – A Contribution to Field Calibration of Surveying Cameras)*. Munich: Deutche Geodaetische Kommision (DGK), Nr. 289 (in German).

Wiley, A., & Wong, K. (1995). Geometric calibration of zoom lenses for computer vision metrology. *PE&RS, 61*(1), 69-74.

Wong, W. (1975). Mathematical formulation and digital analysis in close-range photogrammetry. *PE&RS, 41*(11), 1355-1373.

Yastikli, N., & Jacobsen, K. (2005). Influence of system calibration on direct sensor orientation. *PE&RS, 71*(5), 629-633.

Yilmaza, H., Yakarb, M., & Yildizb, F. (2008). Documentation of historical caravansaries by digital close range photogrammetry. *Automation in Construction, 17*(4), 489-498.

Zeitler, W., Dörstel, C., & Jacobsen, K. (2002). Geometric calibration of the DMC: method and results. *IAPRS, 34(1)*. 6 pages on CD-ROM.

Zhang, Z. (2000). A flexible new technique for camera calibration. *PAMI, 22*(11), 1330-1334.

Ziemann, H. (1986). Thoughts on a standard algorithm for camera calibration. *IAPRS, 26(5)*, pp. 85-93.

Ziemann, H., & El-Hakim, S. (1982). On the definition of lens distortion reference data with odd-power polynomials. *International Archives of Photogrammetry, 24(1)*, pp. 123-130.

Acknowledgements

Relevant Publications

Journal papers

- Tang, R., Fritsch, D., Cramer, M., & Schneider, W. (2012). A flexible mathematical method for camera calibration in digital aerial photogrammetry. *Photogrammetric Engineering & Remote Sensing (PE&RS)*, *78*(10), 1069-1077.
- Tang, R., Fritsch, D., & Cramer, M. (2012). New rigorous and flexible Fourier self-calibration models for airborne camera calibration. *ISPRS Journal of Photogrammetry and Remote Sensing*, *71*(2012), 76-85.
- Tang, R., & Fritsch, D. (2013). Correlation analyses of camera self-calibration in close range photogrammetry. *Photogrammetric Record, 28*(141), 86-95.

Conference papers

- Tang, R., Cramer, M. & Fritsch, D. (2011). Application of Bayesian statistics in photogrammetric bundle adjustment. *Procedia Environmental Sciences* (Elsevier online journal), issue on "Spatial Statistics 2011", *3*(2011), 75-80.
- Tang, R., Fritsch, D., & Cramer, M. (2012). A novel family of mathematical self-calibration additional parameters for airborne camera systems. *European Calibration and Orientation Workshop (EuroCOW 2012)*, 7 pages.
- Tang, R., Fritsch, D., & Cramer, M. (2012). New mathematical self-calibration models in aerial photogrammetry. *32. Wissenschaftlich - Technische Jahrestagung der DGPF (32nd DGPF Annual conference)*, (pp. 457-469).
- Tang, R. (2012). A rigorous and flexible calibration method for digital airborne camera systems. *IAPRS*, *39*(part B2), pp. 153-158.

Awards

Young Author Award for Best Paper, International Society for Photogrammetry and Remote Sensing (ISPRS), 2012.

John I. Davidson President's Award (2nd place) for outstanding paper, American Society for Photogrammetry and Remote Sensing (ASPRS), 2013.

Curriculum Vitae

Personal

Name: Rongfu TANG.

Birth: 5th October, 1982 in Longchuan, Guangdong Province, P. R. China.

Nationality: Chinese.

Education

- 2009.09 – 2013.05: PhD student at the Institute for Photogrammetry (ifp), University of Stuttgart, Stuttgart, Germany.
- 2008.03 – 2009.07: PhD student in School of Electronic Science and Engineering, National University of Defense Technology (NUDT), Changsha, P. R. China (not finished).
- 2005.09 – 2008.02: Master student in Department of Mathematics and Systems Science, NUDT, Changsha, P. R. China.
- 2001.09 – 2005.07: Bachelor student in Department of Mathematics and Systems Science, NUDT, Changsha, P. R. China.